Fakultät für Maschinenwesen

Mechanism Based Constitutive Model for Composite Laminates

Ulrich M. Mandel

Vollständiger Abdruck der von der Fakultät für Maschinenwesen der Technischen Universität München zur Erlangung des akademischen Grades eines

Doktor-Ingenieurs

genehmigten Dissertation.

Vorsitzender:

Prof. Dr.-Ing. Steffen Marburg

Prüfer der Dissertation:

1. Prof. Dr.-Ing. Klaus Drechsler

2. Prof. Dr.-Ing. Peter Middendorf (Universität Stuttgart)

Die Dissertation wurde am 23.01.2017 bei der Technischen Universität München eingereicht und durch die Fakultät für Maschinenwesen am 22.08.2017 angenommen.

Technische Universität München
Fakultät für Maschinenwesen
Lehrstuhl für Carbon Composites
Boltzmannstraße 15
D-85748 Garching bei München

Tel.: +49 (0) 89 / 289 – 15092
Fax.: +49 (0) 89 / 289 – 15097
Email: info@lcc.mw.tum.de
Web: www.lcc.mw.tum.de

KURZFASSUNG

Derzeitige Auslegungsrichtlinien für Faserverbundstrukturen schränken die Ausreizung des enormen Leichtbaupotenzials sowie die Nutzung vielversprechender mechanischer Eigenschaften, wie z.B. Quasi-Duktilität, stark ein. Um dem Konstrukteur zukünftig mehr Freiheit bei der Wahl des Lagenaufbaus zu ermöglichen, muss das Materialverhalten von Faserverbundlaminaten unter allgemeineren Bedingungen besser verstanden werden.

In dieser Arbeit wird ein Konstitutivgesetz vorgestellt, das in der Lage ist das teilweise stark nichtlineare Materialverhalten im Speziellen von Faserverbundlaminaten, die keine Fasern in Lastrichtung enthalten, sehr präzise zu beschreiben. Es wird gezeigt, dass bei großen Verformungen neben der Plastizität des Epoxidharzes auch Faserrotation und Zwischenfaserbruchschädigung eine wichtige Rolle spielen. Das Plastizitätsmodell besteht aus zwei unabhängigen Fließbedingungen für Längsschubspannungen und Spannungen, die senkrecht zu den Fasern wirken. Dabei werden die Auswirkungen von hydrostatischem Druck berücksichtigt. Die experimentelle Bestimmung der erforderlichen Materialkenngrößen und Eigenschaften wird erläutert und für das Prepreg Material HexPly IM7-8552 vorgeführt.

Validiert wurde das Stoffgesetz anhand von unidirektionalen Druckversuchen mit verschiedenen Faserorientierungen aus der Literatur und an einer eigens dazu durchgeführten Versuchsreihe von Angle-Ply Zugproben mit verschiedenen Faserorientierungen und zwei unterschiedlichen Einzellagendicken. Die Versuche haben gezeigt, dass sich die Einzellagendicke nur auf das Zwischenfaserbruchverhalten und das Endversagen auswirken, nicht aber auf das Plastizitätsverhalten. Der Abgleich der Simulation mit den Experimenten zeigt eine sehr gute Übereinstimmung für alle betrachteten Proben.

Der zweite Teil der Arbeit beschäftigt sich mit der numerisch effizienten Abbildung von Laminatendversagen. Aktuelle Materialmodelle sind auf Einzellagenebene definiert und benötigen daher eine sehr feine finite Elemente Vernetzung, bei der jede Lage durch mindestens eine Schicht von Elementen abgebildet wird und zusätzliche Kohäsivzonen ein Ablösen der Schichten voneinander ermöglichen. Ein neuartiger Ansatz mit einer differenzierten Betrachtung von Laminatverfestigung auf Lagenebene und Laminatendfestigung auf Laminatebene wird vorgestellt. Dies ermöglicht netzgrößenunabhängige Ergebnisse auch bei Modellierung des Laminats mit nur einer Lage geschichteter Schalenelemente. Abschließend werden die Endversagens-mechanismen der untersuchten Angle-Ply Laminate als Ausblick auf zukünftige Forschungsaktivitäten diskutiert.

ABSTRACT

Due to conservative design rules the utilization of the enormous lightweight potential and other promising mechanical properties of carbon fiber reinforced composites, like quasi-ductile behavior, are currently limited. To provide the design engineer more freedom to optimize the laminate layup, the general understanding of the material behavior of composite laminates has to be improved.

A constitutive model is developed to describe the nonlinear response of laminates without fibers aligned in load direction. It is shown, that despite the plastic behavior of the epoxy resin the consideration of fiber rotation and inter-fiber damage is essential for large deformations. The evolution of yielding is described by two independent hardening curves either for longitudinal shear or transverse loading. The model additionally accounts for the hydrostatic sensibility of the neat resin. A method for the experimental determination of the required material properties is proposed and demonstrated on the example of the prepreg material HexPly IM7-8552.

For validation unidirectional off-axis compression tests from literature have been simulated. Additionally a test series of angle-ply tension tests with various off-axis angles and two different layups accounting for the influence of the ply thickness has been conducted. The tests have shown that the ply thickness only influences inter-fiber damage and the laminate strength but not plastic yielding. The implemented material model shows excellent correlation for all investigated specimens.

The second part of the thesis addresses the numerical efficient representation of ultimate laminate failure. Current material models for fiber-reinforced composites are usually defined on ply-level and therefore require very fine meshing techniques, where each ply is modeled by at least one layer of elements and additional cohesive zone models enable the representation of delamination. A novel approach is presented where laminate hardening is defined on ply-level but laminate softening is defined on laminate-level. This allows for mesh-size independent results even for layered element modelling, where each element represents the whole laminate. Finally, the failure mechanisms of the investigated angle ply laminates are discussed as outlook for further research.

Contents

Nomenclature

Coordinate Systems

$\{\boldsymbol{x}, \boldsymbol{y}, \boldsymbol{z}\}$	Laminate coordinate system
$\{1, 2, 3\}$	Ply coordinate system
$\{n, nt, n1\}$	Inter-fiber fracture plane coordinate system
$\{l, m\}$	Laminate fracture plane coordinate system

2nd-order tensors

$\boldsymbol{\varepsilon}$	[3x3]	[-]	Strain tensor
$\boldsymbol{\sigma}$	[3x3]	[-]	Stress tensor
$\boldsymbol{C}^e$	[6x6]	[MPa]	Linear elastic ply stiffness tensor
$\boldsymbol{A}$	[3x3]	[N/mm]	Membrane stiffness tensor (Laminated plate theory)
$\boldsymbol{B}$	[3x3]	[N]	Coupling stiffness tensor (Laminated plate theory)
$\boldsymbol{D}$	[3x3]	[Nmm]	Bending stiffness tensor (Laminated plate theory)
$\boldsymbol{M}$	[3x3]	[-]	Damage tensor
$\boldsymbol{R}$	[3x3]	[-]	Rotation tensor

1st-order tensors

$\boldsymbol{\varepsilon}$	[6x1], [3x1]	[-]	Strain vector (Voigt notation)
$\boldsymbol{\sigma}$	[6x1], [3x1]	[-]	Stress vector
$\boldsymbol{\varepsilon}^0$	[3x1]	[-]	Mid-plane strain
$\boldsymbol{\kappa}$	[3x1]	[mm^{-1}]	Curvatures
$\boldsymbol{n}$	[3x1]	[N/mm]	Forces
$\boldsymbol{m}$	[3x1]	[N]	Moments
$\boldsymbol{n}^\theta$	[3x1]	[-]	Direction of rotation

Scalar Parameters

$\boldsymbol{A}$	[mm²]	Fracture surface
α, β	[-]	Hydrostatic sensitivity parameters
d	[-]	Damage variable
$d\lambda$	[-]	Plastic multiplier
δ_{Crack}	[mm^{-1}]	Crack density
Δt	[s]	Time increment
E	[GPa]	Elastic modulus
f	[MPa]	Yield function
G_c	[kJ/mm²]	Fracture energy per unit area (Fracture toughness)
G_{12}, G_{23}	[GPa]	Shear modulus
g_c	[kJ/mm²]	Fracture energy per shell element area
g	[MPa]	Plastic potential
I	[MPa]	Stress invariant
k	[-]	Inter-fiber damage parameter
k_f	[-]	Non-hookean parameter
p	[-]	Inclination parameter
R	[MPa]	Strength value
σ_m	[MPa]	Hydrostatic stress acting in the matrix
t	[mm]	thickness
θ	[rad]	Rotation angle
Y	[N/mm]	Energy dissipation rate
z	[mm]	Position in thickness direction

Indices

$\boldsymbol{c}$	Compression
$diss$	Dissipated
e	Elastic
eq	Equivalent
f	Failure
Lam	Laminate
M	Matrix
p	Plastic
sl	Longitudinal shear
t	Tension
tr	Transverse
$'$	Effective
$\sim$	In-situ
$\parallel$	Parallel to the fibers
$\perp$	Perpendicular to the fibers

Abbreviations

CC	Compact compression
CDM	Continuum damage mechanics
CFRP	Carbon fiber-reinforced plastics
CNC	Computer numerical control
CSYS	Coordinate system
CT	Compact tension
CV	Variation coefficient
DCB	Dual cantilever beam
DIC	Digital image correlation
ELC	End-loaded compression
ENF	End-notched flexure
FE	Finite element
FF	Fiber failure
FRP	Fiber-reinforced plastics
IFF	Inter-fiber failure
MoS2	Molybdenum-disulfide
OAC	Off-axis compression
OAT	Off-axis tension
OHC	Open-hole compression
OHT	Open-hole tension
PEEK	Poly ether ether ketone
QI	Quasi-isotropic

ROM	Rule-of-mixture
RVE	Representative volume element
STDV	Standard deviation
VCCT	Virtual crack closure technique
XFEM	Extended finite element method
X-ray	X-radiation

1 Introduction

1.1 Motivation

Current research and development in aviation and automotive industry is focused on the increase of fuel efficiency. To achieve this goal the products need to be lighter without easing off mechanical performance. Carbon fiber reinforced plastics (CFRP) combine these contrary goals of light weight design and high mechanical performance, as the specific stiffness and strength of CFRP parts outperform metal parts. In fiber direction the stiffness and strength of unidirectional CFRP is similar to high-tensile steel at roughly one-fifth of weight. But perpendicular to the fibers the stiffness of CFRP is about twenty times lower. The transverse strength is even up to forty times lower than the strength in fiber direction. The strongly anisotropic material behavior is a big challenge in designing structural parts, but also allows the design engineer to control the stiffness behavior of the component specifically. Although fiber reinforced composites are used in aerospace since the 1930s and become increasingly important in the automotive industry in recent years, the light weight potential of CFRP is still a long way from being fully exploited. Owing to uncertainties with regard to mechanical design, usually very conservative design rules are used for defining laminate layups.

The fiber orientations are normally restricted to 0°, 90°, 45° and -45°, whereby each of this orientations is represented within the laminate. Defining a laminate according to this limitations has the advantage that any kind of in-plane load can be primary carried by fibers. Beside the limited utilization of the light weight potential, the low strain leading to first ply failure is detrimental. Under tensile loading, inter-fiber cracks occur already at a strain level half of the fiber failure strain. Due to this situation, plies with fiber orientation transverse to the principle load are extremely unfavorable concerning first ply failure. There is still lots of potential for layup optimization to increase light weight efficiency. A fully exploited layup consist actually always of only two or maximum three different fiber orientations [1]. It has been found empirically and demonstrated analytically that any ply groups in a laminate with a certain fiber orientation should be dispersed as much as possible to improve laminate strength and toughness [1]. Principle reasons for this are local stress conditions at the free edges and the possibility to separate the laminate in lower strength sub-laminates by delamination.

To allow for the application of more courageous laminate layups to bearing structures in future, it is very important to learn more about the material behavior of composite laminates. The constitutive behavior of unidirectional CFRP has been widely

understood. Also material models and failure criteria with good accuracy have been developed. But the material behavior of multidirectional laminates is much more complex. In industry usually failure criteria for unidirectional reinforcement are used on ply-level to evaluate a laminate. However, the behavior of an embedded ply differs from a pure unidirectional specimen due to constrain effects of the adjacent plies. Within a laminate also different stress states are acting. In a ply of a multidirectional laminate always two axial stress states are acting even if the laminate as a whole is loaded unidirectional. The load of a laminate can be usually increased after the first inter-fiber cracks occur, as the load of the cracked ply is transmitted to the adjacent plies. Especially the ultimate failure behavior of laminates cannot be predicted by failure criteria on ply level for arbitrary loading conditions. In Fig. 1-1 a broken racing bike fork is shown as example for ultimate failure of a laminated composite structure. Even if first ply failure is predicted in all plies the laminate dose not fail mandatorily, as additional delamination would be necessary for separation. But also laminates can fail were no failure at all is predicted by current ply-level criteria. This kind of laminate failure can be exemplarily found for $\pm 15°$ tension tests. The only case where laminate failure can be predicted for certain, is then the laminate consist plies oriented in load direction. Fiber failure in these plies is then the driver of laminate failure. If there are no fibers oriented in load direction, various laminate failure mechanisms can occur. The laminate can fail by a combination of inter-fiber cracks and delamination. But the laminate can also fail brittle without excessive delamination. For this kind of failure, the orientation of the crack can vary. For example, the crack can be perpendicular to the laminate load or aligned with fibers of one ply. In the area of ultimate failure of laminates under arbitrary load conditions additional research is needed in the short and long-term. The basis for further investigations must be a sound constitutive model able to describe the stiffness behavior of multidirectional laminates and the exact stress states in the single plies accurately. The majority of this thesis is the development of a constitutive model for composite laminates especially for large deformations.

The proposed material model for composite laminates has been developed with the focus on distinction among inducing mechanisms. The effect of fiber reorientation and inter-fiber damage is essential in consideration of large deformations. The evolution of yielding is described by two independent hardening mechanisms for longitudinal shear and transverse loading. The prime objective in development of the nonlinear material model was the generation of a profound understanding of the material behavior. A mechanism based formulation allows furthermore relatively few material parameters considering the accuracy of the model. A sound physical basis is very important for the development of a new material model. Especially for fiber reinforced composites there are always too little experimentally determined supporting points for verification. This is why developing a material model as a mathematical fit function is not expedient.

Fig. 1-1: Broken Cervelo C2P Fork [2]

The second part of the thesis deals with the numerical modelling of ultimate laminate failure. Especially in automotive industry many structural components are designed for one-time crash load cases. For the estimation of the maximum bearable load of composite components, a few continuum damage models are already available [3–15]. All these models are either mesh size dependent (strain-based softening formulations) or require fine modeling technics, where each ply is represented by at least one layer of elements and between the plies additional cohesive elements are used to model delamination (energy-based softening formulations). Due to numerical expenses only finite element meshing with layered shell elements, where the whole laminate layup is represented within one element, are suitable for industrial applications. A new approach is proposed allowing for an energy-based softening law in combination with layered elements. This enables mesh size independent solutions at minimal numerical effort.

1.2 Objectives of the Thesis

The main objective of the research work presented in this thesis is to learn more about the material behavior of fiber-reinforced composites by numerical and experimental studies. This should result in a new material model for the accurate simulation of the nonlinear material response of composite laminates even at large deformations. Especially laminates where no fibers are aligned in load direction are focused. Beside the nonlinear constitutive behavior of laminates, the numerical efficient modelling of

the ultimate failure of composite structures should be aimed. The major objectives of the thesis can be summarized as:

- Comprehensive experimental investigation and characterization of the nonlinear material behavior of composite laminates
- Development of a nonlinear material model for CFRP laminates for the accurate description of the laminate's constitutive behavior and the precise evaluation of stress states in the single plies
- Improving the understanding of material and minimizing the required number of parameters by utilizing mechanism based formulations
- Development of a numerical efficient material model approach for layered shell elements for the mesh-size independent prediction of the maximum bearable load of laminated composite structures

1.3 Thesis Outline

The following summarizes the content of the individual chapters of the thesis. As several specific topics are addressed in this thesis, literature review is split to different places in this thesis.

2 Laminate based Formulation

An overview of the proposed material model for composite laminates is given in this chapter. It is shown how both parts of the model, laminate hardening and laminate softening, work together. The interaction of the individual constituents of the material model is shown in a flowchart (Fig. 2-4) using the section headings of the thesis. Moreover, the assumptions and restrictions made for the model are mentioned.

3 Laminate Hardening

In this section, a nonlinear constitutive model for composite laminates is proposed. First several plasticity models from literature for unidirectional fiber-reinforced plastics are briefly presented. Then the laminate hardening model is presented in the next sub-sections addressing the influencing mechanisms. For each mechanism specific literature is provided and discussed. For validation of the laminate hardening model, simulated and experimental results of several off-axis compression tests from literature and conducted angle-ply tension tests are shown and discussed. The experimental setup and specimen preparation of the angle-ply tension tests is also described in this section.

4 Laminate Softening

This section is focused on modeling the ultimate failure of laminated composite structures. A new approach is proposed allowing for an energy-based softening law in combination with layered elements. This enables mesh size independent solutions at minimal numerical effort. For validation, open-hole tension tests with various hole-

diameters from literature have been simulated using several mesh-sizes. Finally, the ultimate failure mechanisms of the angle-ply tension tests are discussed based on their fracture surfaces and stress data.

5 Conclusion

In chapter 5 the proposed material model for CFRP laminates is presented in a summary from by naming the considered physical mechanisms. Also the experimental validation and discussion about the model's applicability are summarized.

6 Outlook

In this section further steps to make the model applicable for industrial applications are mentioned. Additionally, open questions are stated and decisive issues for further research are given.

2 Laminate based Formulation

In current research, the material behavior of fiber-reinforced composites is investigated on different scales. To describe physical phenomenon by numerical simulations, composites have to be considered on a micromechanical scale. Therefore, representative volume elements (RVEs) have been established, where the single fibers are modeled separately and usually even a stochastic fiber distribution is assumed [16]. Some studies account for the influence of laminate dependencies (in-situ) on the inter-fiber cracking behavior of embedded plies [17–19]. Moreover, the effect of changing the fiber, resin or fiber-resin interface properties can be estimated by micromechanical models. An example for this is a numerical study to estimate the increase of the fracture toughness for fiber failure by mixing different types of carbon fibers [20].

The results of micromechanical studies must be transferred to a smeared ply level due to the fact that micromechanical models are not applicable on structural applications because of their numerical effort. In literature, this process is commonly named multi-scale modelling. For this purpose, different approaches have been developed. On the one hand there are models using simple analytical micromechanical models allowing for a direct implementation within the constitutive law [21–23]. On the other hand, micromechanical models are used to determine input parameters for a smeared model [15, 24]. This idea sounds very attractive, since it would mean that characterizing the fibers, the resin and the fiber-matrix interface enables to simulate the response of any laminate with an arbitrary layup. The problem in applying this idea is, that the number of required properties and parameters rises with increasing fineness of the model. In other words, a micromechanical model, able to simulate the same material response than a smeared model requires more parameters than the smeared model. For that reason, micromechanical models have not been established for strength prediction of composites so far. Reasonable applications are the quick estimation of modified properties due to changing the fibers, the resin, the fiber volume fraction, the ply thickness or the orientation of adjacent plies.

The most important failure criteria for fiber-reinforced composites are all defined on ply-level and consider a smeared continuum [25–30]. For the analysis of laminates the stress state in each ply has to be calculated and evaluated. The fact that failure in one ply does not necessarily mean failure of the laminate makes the analysis of laminates difficult. Especially inter-fiber cracks can occur considerably before laminate failure. To detect inter-fiber failure in an embedded ply, the effect of the surrounding laminate has to be considered. In thin plies embedded between stiff plies inter-fiber cracks occur much later than in thick plies or unidirectional specimens. Fiber failure in at least one

ply always results in laminate failure for all practical layups. The big problem is the estimation of the laminate strength than no ply is oriented in the main load direction. In this case the laminate fails without reaching the fiber strength in any ply. For some layups even inter-fiber cracks are not predicted at the laminate failure load, see Section 3.6.4.

Beside the strength the fracture toughness is a very important property when analyzing structural parts. At a stress concentration a crack can only form and growth if the stress state is higher than the strength and the energy release rate is large enough. In continuum damage mechanics (CDM) the energy release rate can be used to become independent of the mesh size [31]. Therefore, the failing elements must dissipate the fracture energy during degradation. As the energy dissipation rate has to be adhered to on laminate level and not mandatory on ply level, in the proposed material model the softening law is defined on laminate level, see Fig. 2-1. This results in the advantage that the model is applicable in combination with layered shell elements. In contrast, current continuum damage models for composites are usually defined on ply level. Therefore, they require a fine modelling technique, where each ply is represented by at least one layer of elements and between the plies cohesive elements are placed to represent possible delamination.

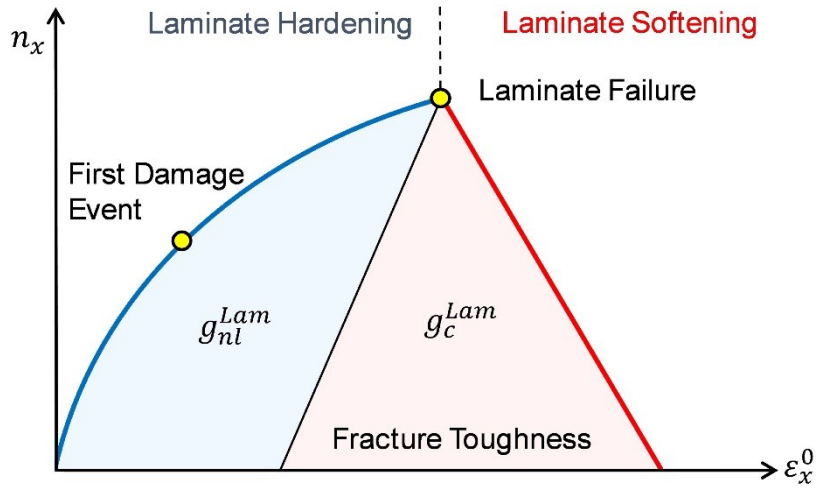

Fig. 2-1: Constitutive behavior of composite laminates

The calculation procedure of the presented material model is illustrated in Fig. 2-4, using the section headings in this thesis. The model is developed for explicit time integration. Therefore, at the beginning of each time step, it has to be checked if the ultimate laminate failure criterion, see Section 4.1, predicts failure and subsequently the softening behavior is responsible to calculate the laminate response, or if the current loading condition of the laminate is in the hardening domain. Once ultimate failure is predicted, the model will stay in the softening domain, even if the laminate gets unloaded.

The constitutive behavior of composite laminates is depending on the layup more or less nonlinear. An accurate analysis requires the consideration of all mechanisms influencing the constitutive material behavior. These are an accumulation of plastic strains, deformation induced fiber rotation, non-hookean elasticity in fiber direction and inter fiber damage effects. In Fig. 2-4, these mechanisms are listed in terms of section headings. A more detailed flowchart of the hardening model representing the interactions of the mechanisms is given in Fig. 3-1. The precise simulation of the stress-strain response prior to failure is essential to predict the ultimate failure of a structure. Otherwise incorrect stress states are determined, leading to misinterpretation of locus and time of damage initiation and its progression. In contrast to the laminate softening, in the proposed material model the nonlinear constitutive behavior during laminate hardening is defined on ply level.

When modeling nonlinear material behavior of a laminate with layered shell elements, at each integration point of the element section points are defined through the thickness. For each ply at least one section point is required as shown in Fig. 2-2.

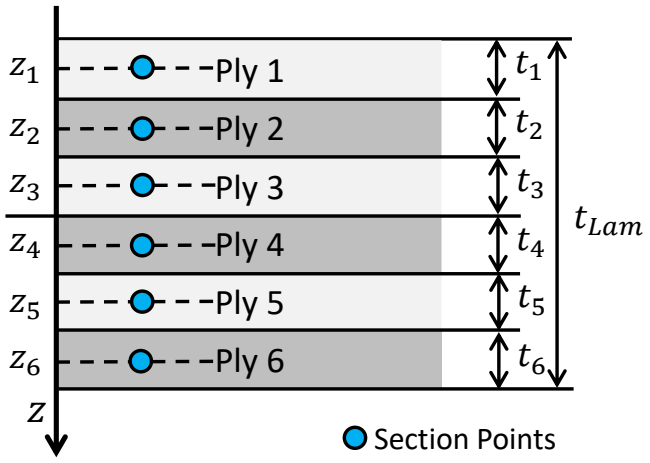

Fig. 2-2: Section points through the thickness of the laminate at the location of the element integration point

For more accuracy more section points can be defined. In Fig. 2-3 three section points within one ply are shown for Gauss integration. The position $z_{k,i}$ of the Gauss section points depending on the number of section points defined for each ply is given in Table A-1. The related thickness $t_{k,i}$ for each integration point is given in Table A-2.

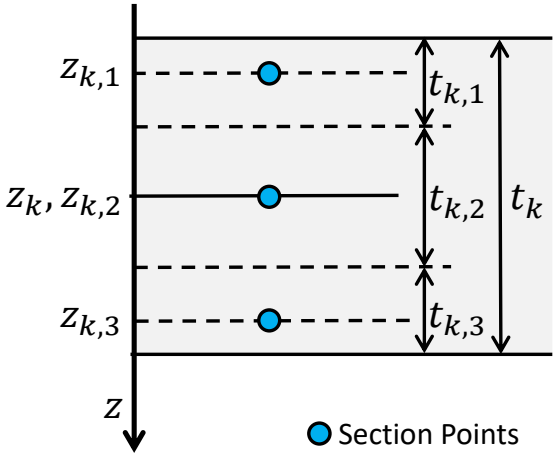

Fig. 2-3: Three Gauss section points through the thickness of one ply

During laminate hardening the stress at each section point has to be calculated. The strain at each section point is given by

$$\boldsymbol{\varepsilon}_{k,i} = \boldsymbol{\varepsilon}^0 + z_{k,i}\,\boldsymbol{\kappa}. \tag{2-1}$$

In the next calculation step the section point strain is transformed to fiber coordinates. Here also the deformation induced reorientation of the fibers, see Section 3.1, is considered. The resulting stress at each section point is calculated by the proposed constitutive model described in Section 3. Next, the section point stress is transformed to the laminate coordinate system. Then the resulting laminate forces and moments have to be calculated. The laminate forces result by multiplying the stress at each section point $\boldsymbol{\sigma}_{k,i}$ with its corresponding thickness $t_{k,i}$:

$$\boldsymbol{n} = \sum_k \sum_i \boldsymbol{\sigma}_{k,i} t_{k,i}. \tag{2-2}$$

For the determination of the laminate moments the section point stresses $\boldsymbol{\sigma}_{k,i}$ are multiplied by the corresponding thickness $t_{k,i}$ and the corresponding position $z_{k,i}$.

$$\boldsymbol{m} = \sum_k \sum_i \boldsymbol{\sigma}_{k,i} t_{k,i} z_{k,i}. \tag{2-3}$$

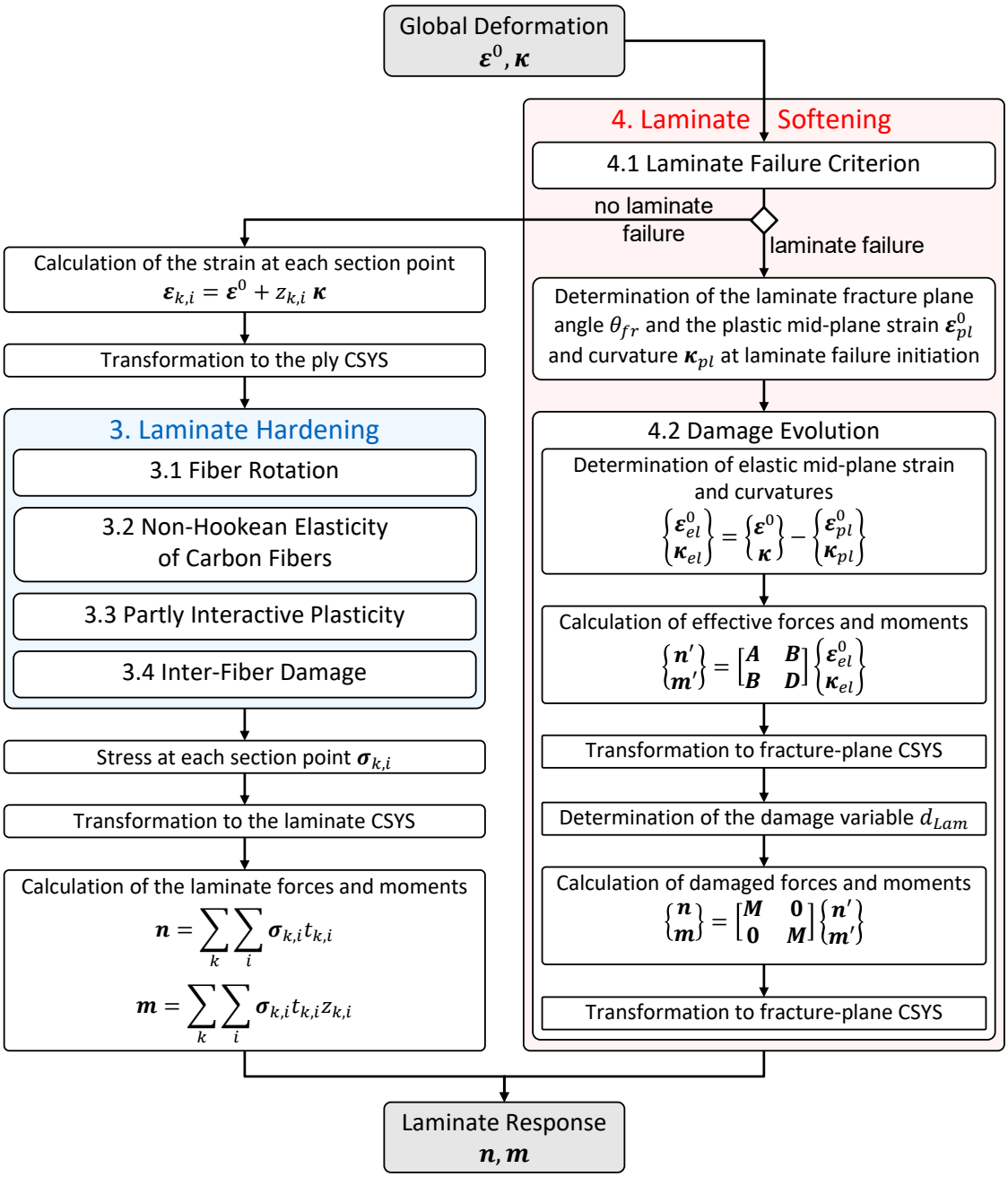

Fig. 2-4: Flowchart of the calculation approach

Explicit Dynamic Analysis

For solving nonlinear problem with the finite element method implicit and explicit integration methods can be used. In an implicit dynamic analysis at each time increment the nonlinear equilibrium equations must be solved. An explicit dynamic analysis uses the central-difference operator for integration of the equations of motion. As a consequence, the equilibrium equations need not to be solved exactly at each time increment, but a linear estimation is sufficient. However, the size of the time increments is limited. The stable time increment (largest suitable time increment Δt) is related to

the time required to a stress wave to cross the smallest element in the model. Thus, a high mesh quality is required for an explicit dynamic analysis, as only one small element can increase the numerical effort dramatically. Nevertheless, for large nonlinear problems and for solving extremely discontinuous short-term events the explicit integration method is often more efficient than the implicit integration method. An additional reason for choosing the explicit integration method is the effort to define a material model. An implicit material model requires iterative procedures to solve the nonlinear equations. Furthermore, stabilization methods are necessary to prevent the solver to run in an infinite loop. For the reasons mentioned above, the presented material model for composite laminates is defined for explicit dynamic analysis. The explicit calculation process of *ABAQUS* is visualized in Fig. 2-5.

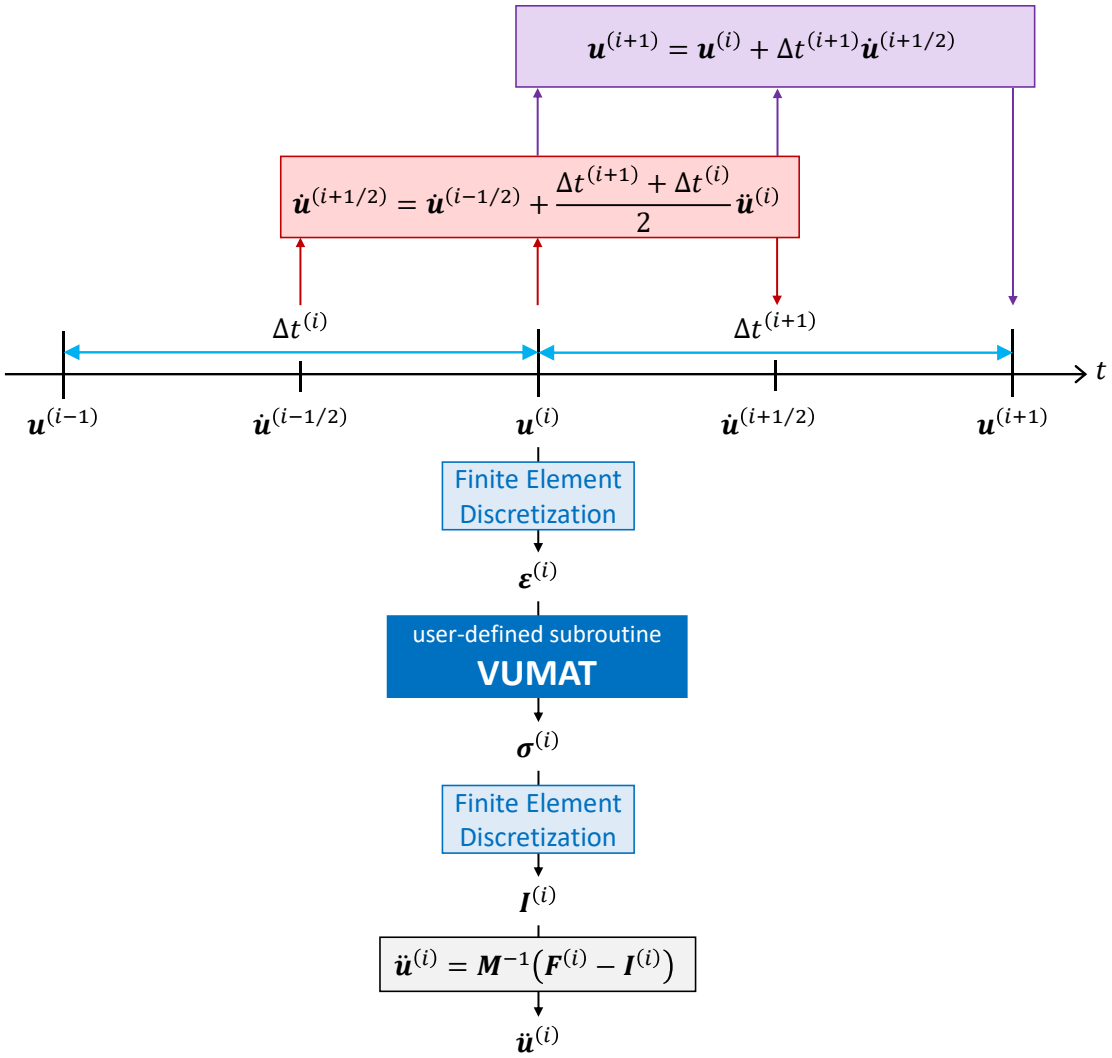

Fig. 2-5: Flowchart of explicit time integration

At each time increment, the acceleration $\ddot{\boldsymbol{u}}$ has to be calculated. The finite element discretization transforms the displacement $\boldsymbol{u}$ into strain states $\boldsymbol{\varepsilon}$ at each integration point.

The relation between strain $\boldsymbol{\varepsilon}$ and stress $\boldsymbol{\sigma}$ is given by the constitutive model. The presented material model has been implemented as *ABAQUS VUMAT*. At each time step, the user-defined program code is called to calculate the stress state $\boldsymbol{\sigma}$ at each integration point. For numerical efficiency, the *VUMAT* calculates the stress state at usually 128 integration points with every call. By multiplication of the mass matrix $\boldsymbol{M}$ with the difference between the applied load vector $\boldsymbol{F}$ and the internal force vector $\boldsymbol{I}$ the acceleration at the beginning of the increment $\ddot{\boldsymbol{u}}^{(i)}$ can be determined. As shown in Fig. 2-5, the acceleration at the beginning of the increment $\ddot{\boldsymbol{u}}^{(i)}$ influences the displacement at the end of the increment $\boldsymbol{u}^{(i+1)}$. In this way the integration process keeps the error in the balance of force little.

Assumptions and Limitations

The proposed material model for composite laminates is defined for plane stress states, with the exception of the plasticity model and the consideration of deformation induced fiber rotation. As composite laminates are usually used for shell structures, a plane stress state can be assumed without risking an important error. The material behavior of composite laminates is complex and influenced by many factors. Due to a lack of experimental studies for validation and to limit the complexity of the model some requirements for the model's applicability are defined. The model is only valid under quasi-static loading and room temperature conditions. Also the influence of moisture is not considered. The main goal of the model is to predict the nonlinear response and the maximum bearable load of composite structures. The unloading behavior is not focused, but defined in a way to avoid material heeling and energy creation.

3 Laminate Hardening

The objective of the laminate hardening model is to represent the nonlinear material behavior of continuous fiber reinforced plastics accurately even at large deformations. The accurate prediction of the complex three dimensional stress state acting at the critical area of a structural part is a basic requirement for a sensible failure analysis. Simultaneously, the number of required parameters shall be kept as low as possible. A reliable structural design of composite parts, requires an accurate prediction of the stress state at the critical areas. These are often areas of load transmission where a complex three dimensional stress state is acting. Therefore, the laminate hardening model, expect the inter-fiber damage model, is formulated for the evaluation of three dimensional stress states. The laminate hardening model as a whole has already been published at an earlier stage, see [32]. Also a concise description of the three dimensional plasticity model has been published, see [33]. The constitutive response of fiber-reinforced composites prior to ultimate failure is determined by the interaction of several processes within the material constituents. Dependent on the prevailing direction and amount of the applied load in relation to fiber and matrix, several sources can be responsible for a nonlinear stress–strain behavior and characterize the specific degree of nonlinearity. These are an accumulation of viscoelastic and viscoplastic deformations, fiber deflection, damage effects and the non-hookean elasticity in fiber direction. The numerical simulation requires a material model that considers the micromechanical physics of the composite. The presented model accounts for all presumed sources interactively in order to stray from a mathematically-defined approach. The constitutive behavior of epoxy resin is time and temperature dependent [34]. As a consequence, also the constitutive behavior of fiber-reinforced composites is influenced by strain-rate and temperature conditions. To avoid a considerable influence of time and temperature, the experiments used for the model`s validation are conducted quasi-static on low strain rates and room temperature. Equivalently, the constitutive model is implemented in the context of rate-independent plasticity with isotropic hardening. To show the interaction of the sources, influencing the nonlinear response, the calculation procedure of the material model is illustrated schematically in Fig. 3-1. The numerical representation of fiber rotation, plasticity, inter-fiber damage and non-hookean elasticity in fiber direction are addressed in the following sections.

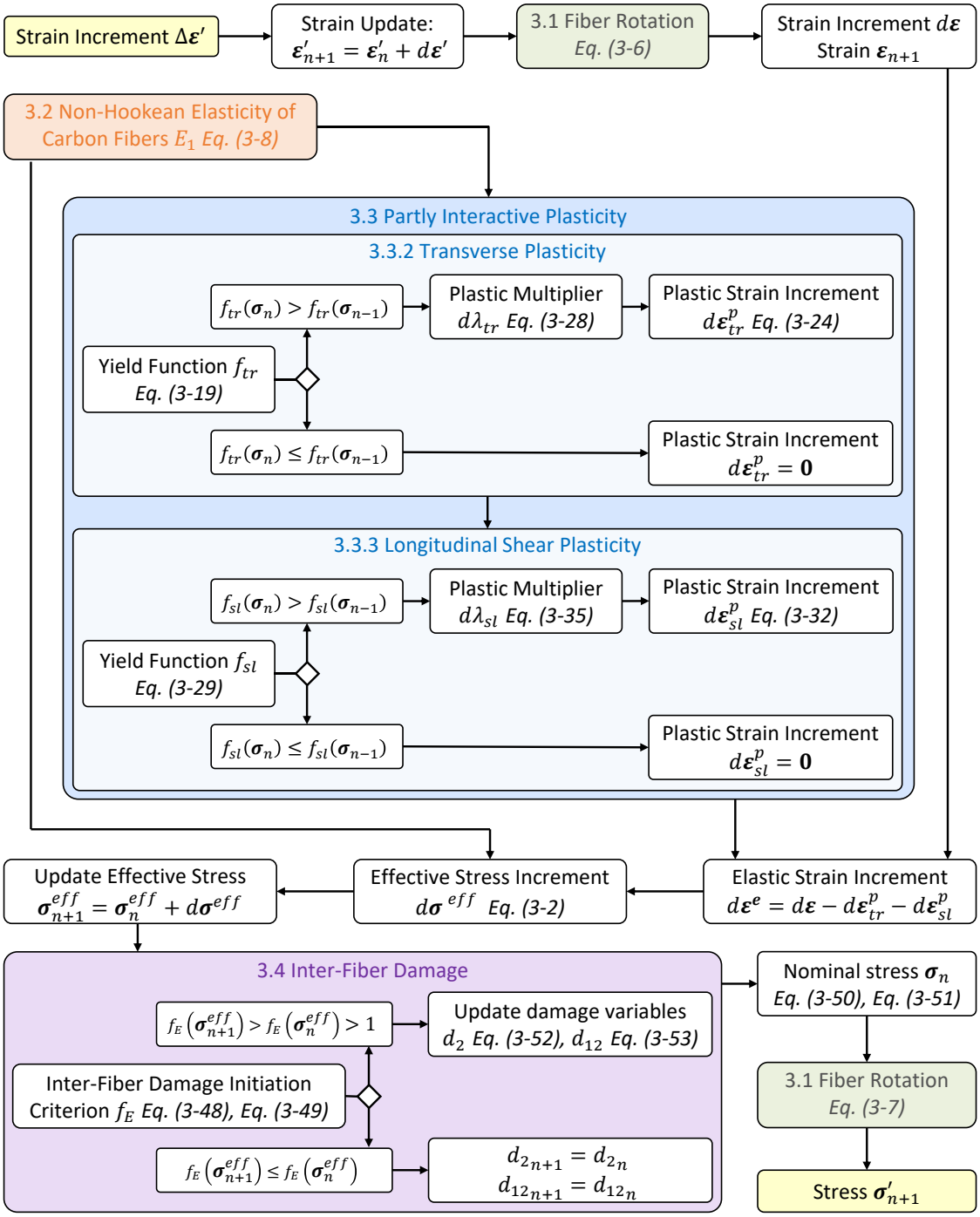

Fig. 3-1: Flowchart of the hardening model

At each time increment the stress state at the end of the increment has to be calculated. As input for the calculation the strain increment of the current time step and the user-defined variables calculated at the last time step are available. First, the strain state at the end of the increment is calculated. Then, the material routine transforms the strain increment according to the actual fiber orientation, considering deformation induced

fiber reorientation. Next, the incremental strain $d\boldsymbol{\varepsilon}$ is linearly decomposed into the elastic part $d\boldsymbol{\varepsilon}^e$ and the plastic parts $d\boldsymbol{\varepsilon}_{tr}^p$ and $d\boldsymbol{\varepsilon}_{sl}^p$ as

$$d\boldsymbol{\varepsilon} = d\boldsymbol{\varepsilon}^e + d\boldsymbol{\varepsilon}_{tr}^p + d\boldsymbol{\varepsilon}_{sl}^p. \tag{3-1}$$

The plastic parts of the strain $\boldsymbol{\varepsilon}_{tr}^p$ and $\boldsymbol{\varepsilon}_{sl}^p$ are defined in such a way that the plastic strain components are either controlled by the transverse plasticity or by the longitudinal shear plasticity. In detail, the plastic strain components $\varepsilon_{tr_{12}}^p, \varepsilon_{tr_{13}}^p, \varepsilon_{sl_{11}}^p, \varepsilon_{sl_{22}}^p, \varepsilon_{sl_{33}}^p$ and $\varepsilon_{sl_{23}}^p$ are allways zero. The other components are calculated by the transverse plasticity and the longitudinal shear plasticity model respectively, as shown in Fig. 3-1. The stress increment $d\boldsymbol{\sigma}$ results from the multiplication of the elastic stiffness matrix $\boldsymbol{C}^e$ and the elastic strain increment $d\boldsymbol{\varepsilon}^e$

$$d\boldsymbol{\sigma} = \boldsymbol{C}^e d\boldsymbol{\varepsilon}^e. \tag{3-2}$$

At the end of the calculation process the stress increment is transformed into the coordinate system of the finite element, where the fiber direction is defined in the non-deformed state.

3.1 Fiber Rotation

A few studies account for the mechanism of fiber reorientation induced by deformation [35–38]. Especially at large deformations, fiber rotation has a substantial influence on the nonlinear material behavior. But also for laminates with a large poison ratio, fiber rotation results in a considerable stiffening even at low deformations. As a consequence, neglecting fiber reorientation can easily provoke a misinterpretation of the response of a ±30° tension test. Ignoring stiffening due to fiber rotation could mislead to a predicted influence of σ_{22} on the σ_{12} shear response in order to compensate for the missing stiffness. This wrongly assumed inner friction interaction would reduce the shear nonlinearity for a concurrent transverse compression. Hence, it is absolutely necessary to consider fiber rotation, when defining a nonlinear material model for fiber-reinforced composites. Otherwise, the laminate stress-strain response and especially the ply-stress data become worse for increasing deformation and impede a reasonable failure analysis.

As shown in Fig. 3-2, an in-plane shear deformation causes an additional rotation of the fibers. Depending on the layup of a unidirectional laminate, high shear strains can occur. Due to the inherent orthotropic behavior of carbon fiber reinforced composites, fiber reorientation has a strong influence on the constitutive response of the laminate. In particular for ±45° angle-ply laminates, usually used for in-plane shear characterization [39], an additional fiber rotation of almost eight degrees arises, see Fig. 3-4. In case of a three-dimensional constitutive model formulation, not only in-plane shear deformation

leads to a reorientation of the fibers, but also an out-of-plane longitudinal shear strain ε_{13}.

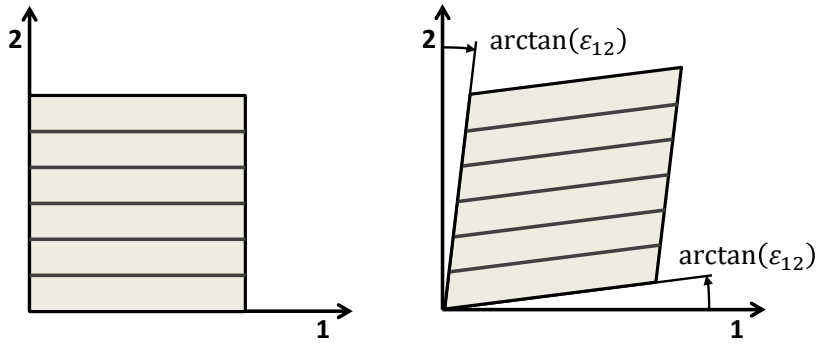

Fig. 3-2: Rotation of the fiber orientation due to in-plane shear deformation

In the finite element software *ABAQUS*, a separate coordinate system is created for each element when using the option *discrete orientation*. Thus, under loading the material orientation of each element can change separately. During a geometric nonlinear analysis the software takes into account the change of the material orientation caused by rigid body rotation of the element. But the change of the fiber orientation caused by the deformation of the element itself is not considered by default. Therefore it is necessary to care for within the use-defined material subroutine, see Fig. 3-3.

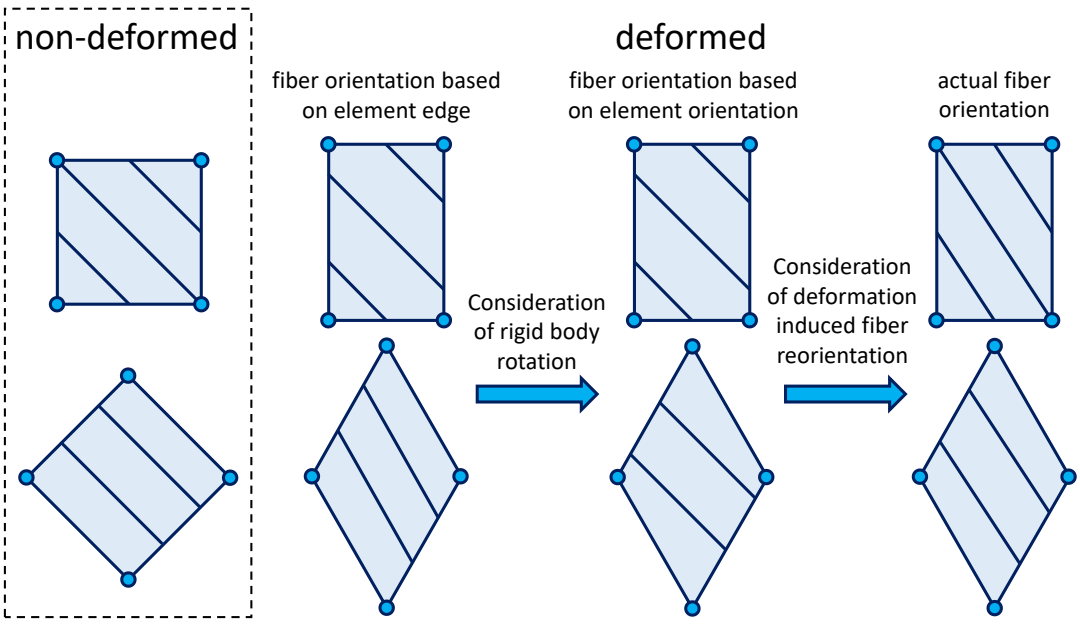

Fig. 3-3: Consideration of fiber reorientation within a finite element analysis

The deformation induced rotation angle θ and the direction of the rotation $\boldsymbol{n}^{\theta}$ arise from the current deformation state:

$$\theta = \arctan\sqrt{{\varepsilon'_{12}}^2 + {\varepsilon'_{13}}^2} \tag{3-3}$$

$$\boldsymbol{n}^{\theta} = \begin{Bmatrix} n_1^{\theta} \\ n_2^{\theta} \\ n_3^{\theta} \end{Bmatrix} = \frac{1}{\sqrt{{\varepsilon'_{12}}^2 + {\varepsilon'_{13}}^2}} \begin{Bmatrix} 0 \\ \varepsilon'_{13} \\ \varepsilon'_{12} \end{Bmatrix} \tag{3-4}$$

The strain components ε'_{12} and ε'_{13} are defined in the non-rotated coordinate system $\{1', 2', 3'\}$, where the $1'$-direction is aligned in fiber direction of the non-deformed state. According to the condition $n_1^{\theta} = 0$, the rotation tensor $\boldsymbol{R}$ can be written as

$$\boldsymbol{R}(\theta) = \begin{bmatrix} \cos\theta & -n_3^{\theta}\ \sin\theta & n_2^{\theta}\ \sin\theta \\ n_3^{\theta}\ \sin\theta & {n_2^{\theta}}^2\ (1-\cos\theta) + \cos\theta & n_2^{\theta}\ n_3^{\theta}\ (1-\cos\theta) \\ -n_2^{\theta}\ \sin\theta & n_2^{\theta}\ n_3^{\theta}\ (1-\cos\theta) & {n_3^{\theta}}^2\ (1-\cos\theta) + \cos\theta \end{bmatrix}. \tag{3-5}$$

The actual strain, considering fiber reorientation, can be calculated incrementally:

$$\boldsymbol{\varepsilon}_{n+1} = \boldsymbol{\varepsilon}_n + \boldsymbol{R}(\theta)^T\ d\boldsymbol{\varepsilon}'\ \boldsymbol{R}(\theta). \tag{3-6}$$

Based on the local strains present at the current time increment, the stress state can be calculated by application of the constitutive model, as shown in Fig. 3-1. The last step of the calculation procedure is the retransformation of the stress increment into the initial non-rotated coordinate system $\{1', 2', 3'\}$:

$$\boldsymbol{\sigma}'_{n+1} = \boldsymbol{\sigma}'_n + \boldsymbol{R}(-\theta)^T\ d\boldsymbol{\sigma}\ \boldsymbol{R}(-\theta). \tag{3-7}$$

It should be noted that Eq. (3-6) and Eq. (3-7) are only valid if the strain $\boldsymbol{\varepsilon}$ and stress $\boldsymbol{\sigma}$ are defined as second order tensors.

The development of the additional fiber rotation for angle-ply tension tests is shown in Fig. 3-4. As indicated, there is an excellent correlation between optically-measured (DIC) experiments and numerical results. However, especially the large values for the $\pm 30°$, $\pm 40°$ and $\pm 45°$ laminates suggest the significant influence on the axial modulus that shows the inevitability of considering fiber reorientation in a constitutive model. Referred to the axial strain, the $\pm 30°$ laminate shows the largest change of the fiber orientation. This goes along with the huge transverse contraction of such a layup. The accurate prediction of the fiber angle change concurrently ensures a correct representation of the specimen's transverse contraction.

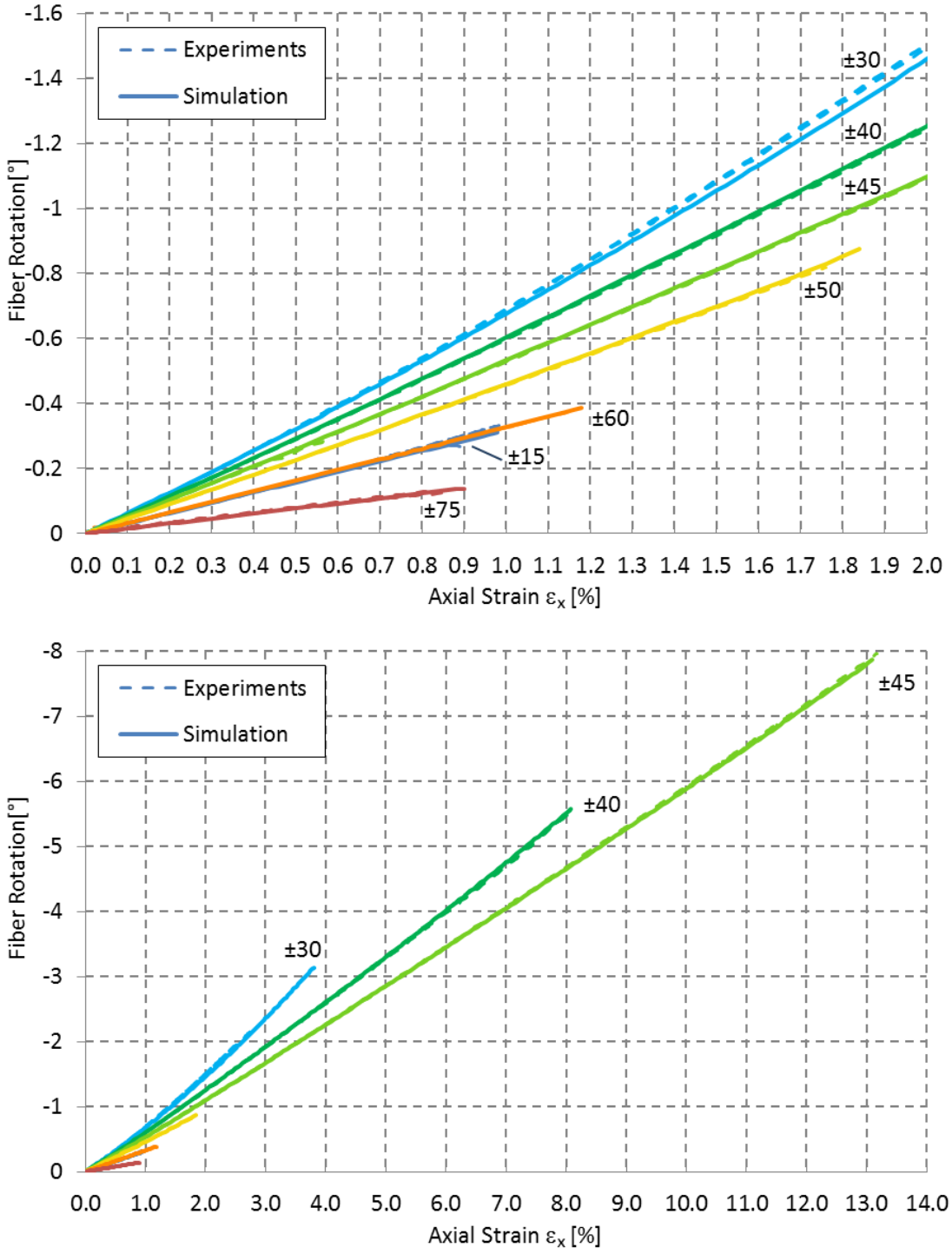

Fig. 3-4: Experimental and numerical evaluation of fiber rotation of angle-ply tension tests

3.2 Non-Hookean Elasticity of Carbon Fibers

The constitutive behavior in fiber direction of carbon composites is usually assumed to be linearly elastic up to failure. However, the Young's modulus in fiber direction changes with loading. The tensile modulus in fiber direction increases with increasing tensile load [40, 41], while the compressive modulus decreases with increasing compressive load [42]. From experimental data of 0° tensile tests, van Dreumel found the Young's modulus to be proportional to the stress [41]. A slightly different observation has been made by Stecenko [42] and Djordjecić [40], who describe the relation between Young's modulus and strain to be linear. This non-hookean behavior is not caused by micro waviness of the fibers within a ply, but is driven by the fibers themselves. So the stiffening effect under tensile loading can also be observed for single non-impregnated fibers [43]. A further interesting aspect is that the rule-of-mixture (ROM) overrates the Young's modulus in fiber direction as shown in [44]. It is because the ROM equation is only a theoretical upper bound of modulus that assumes perfect fiber-matrix adhesion. As a consequence also the fiber-matrix adhesion influences the modulus in fiber direction. This effect was experimentally investigated by Madhukar [44], who tested several specimens using the same carbon fibers with different fiber surface modifications. The non-hookean stress strain response of carbon fibers is reversible and unaffected by loading and unloading cycles up to at least 40% of the tensile strength [40]. This suggests that the nonlinear material behavior is real non-hookean elasticity. According to the experimental observable feature the Young's modulus in fiber direction E_1 is defined as

$$E_1 = E_1^0\left(1 + k_f\, \varepsilon_{11}\right), \tag{3-8}$$

where E_1^0 is the initial Young's modulus and the constant k_f controlls the stiffening due to tensile load. As the material model is defined for explicit forward Euler time integration, at each time step the current modulus is used for stress update. For the experimental determination of k_f unidirectional longitudinal tension tests have been conducted. Five specimens with a length of 250mm, a width of 25mm and a thickness of 2mm were fabricated as described in Section 3.6.2. The scattering between the specimens is very slight and a stiffening with increasing load is clearly visible, as shown in Fig. 3-5. The strength values for all specimens are given in Table A-3. With $k_f = 21.0$ the numerical material model correlates very well with the experimental results. The other material properties used for the simulation are given in Table 3-1.

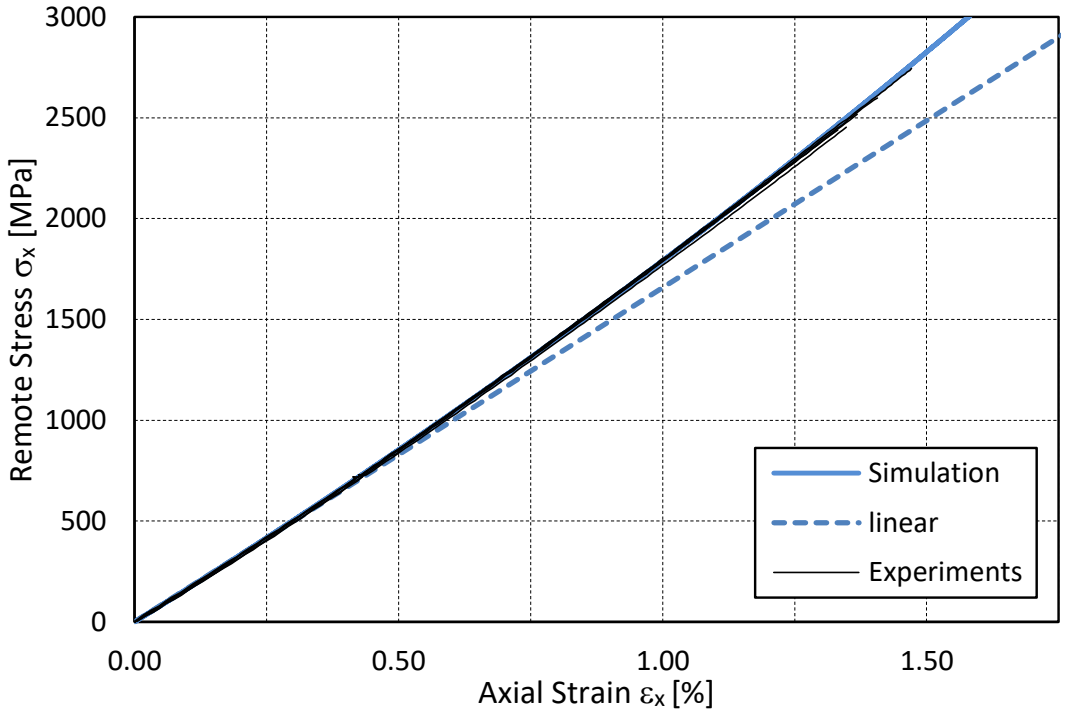

Fig. 3-5: Remote axial stress-strain response of longitudinal tension specimens for IM7-8552

3.3 Partly Interactive Plasticity

Loads acting at an oblique angle to the fiber orientation lead to a nonlinear material response due to yield processes within the epoxy resin. Current yield criterions for fiber-reinforced polymers are predominantly based on the deviatoric yield criterion for orthotropic solids, known as Hill`s criterion [45] or the Drucker-Prager yield criterion [46], which accounts additionally for the hydrostatic stress state. Both criteria are theoretically formulated as fully interactive in the yield behavior of the considered stress components.

Hill [45] presented a generalized yield criterion for orthotropic material behavior. It is based on a fully quadratic stress interaction neglecting linear stress terms. The yield locus is defined by six parameters which can be determined experimentally. Therefore, Hill proposed three uniaxial tension tests in the principal directions orthogonal to the planes of orthotropy and three pure shear tests in the planes of orthotropy. Xie [47] proposed a yield criterion based on a simplification of Hill`s work related to FRP`s. With the assumption of transverse isotropy and an assumed linear elastic behavior in fiber direction, the number of required parameters is reduced to two. As they are considered as intrinsic material constants, one hardening decisive effective stress-strain curve is defined, based on 5 different uniaxial and biaxial test setups. A further reduction of Hill`s yield criterion for the application on FRP`s is proposed by Sun [48]. Due to a fixed

specification of several yield parameters and the assumption of a plane stress state, only one parameter has to be provided. The yield function defined by Sun reads:

$$2f = {\sigma_{22}}^2 + 2a_{66}{\sigma_{12}}^2. \tag{3-9}$$

Similar to [47], a single effective stress-strain curve is proposed to assign the hardening behavior under various stress states. Sun [48] proposed a set of off-axis tests in order to define the hardening curve. As shown in [49] for unidirectional CFRP laminates of IM7-8552, it is not possible to match OAC and OAT results with only one single hardening curve. The application of two curves would provoke a knee in the stress-strain curve for a [±45]-laminate at the transition of tension and compression regime. The main problem of the model of Sun is the prediction for a pure longitudinal shear load. As an additional transverse stress, independent of its sign, results in an increase of the plastic flow, it is not possible to match a pure in-plane shear curve together with off-axis tests. Even if the model predicts the axial stress-strain response correctly, the disposition of the plastic flow in the transverse and the shear component is wrong.

A direct formulation of a yield criterion for FRP`s is presented by Boehler [50] based on invariants formulation in the context of the generalized theory of transversely isotropic solids. Spencer [51] proposed a criterion taking into account only quadratic stress interactions. The criterion exclusively consists of deviatoric stress invariants, as he assumes an independence of hydrostatic stress. Moreover, yielding is not affected by stresses in fiber direction, as only fiber independent stress invariants are used. In a recent paper, Vogler [52] stated a tri-axial yield criterion including an additional invariant that contains linear non-deviatoric stress terms, transverse to the fiber. The yield surface given by Vogler reads:

$$f = \alpha_1 I_1 + \alpha_2 I_2 + \alpha_3 I_3 + \alpha_{32} I_3^2 \leq 0, \tag{3-10}$$

where the invariants are defined as:

$$I_1 = {\sigma_{23}}^2 + \frac{1}{4}(\sigma_{22} - \sigma_{33})^2, \quad I_2 = {\sigma_{12}}^2 + {\sigma_{13}}^2, \quad I_3 = \sigma_{22} + \sigma_{33}. \tag{3-11}$$

The yield surface can be illustrated in stress space or invariant space is shown in Fig. 3-6. For the determination of yield surface parameters α six different test setups are required. A longitudinal and a transverse shear test, a transverse uniaxial compression and tension test and a biaxial compression and tension test.

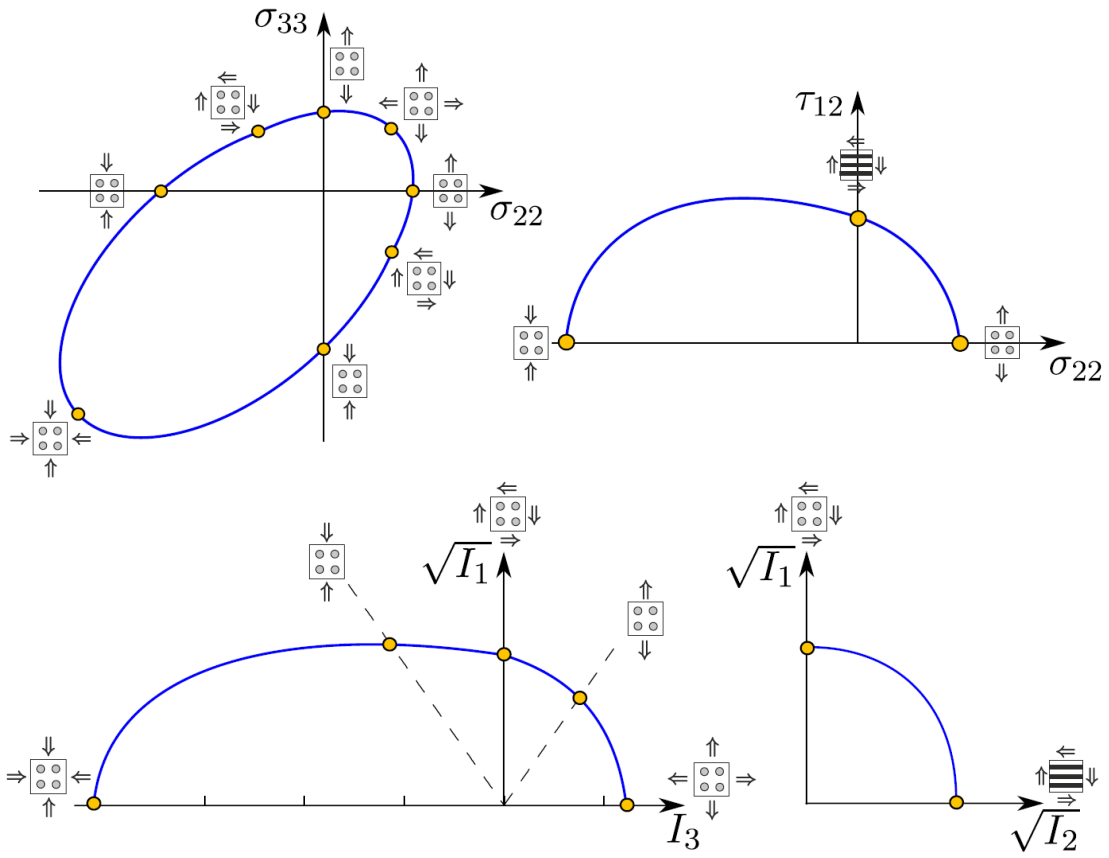

Fig. 3-6: Schematic representation of the yield surface [52]

To allow for an accurate prediction of the plastic Poisson coefficients and of the volumetric plastic strains, Vogler introduced a non-associative flow rule. The evolution of the plastic strains is not given by the gradient of the yield surface, but by the gradient of a plastic potential function g. The plastic flow potential is defined as:

$$g = \beta_1 I_1 + \beta_2 I_2 + \beta_3 I_3^2 - 1. \tag{3-12}$$

The plastic potential parameters β control plastic contractility during yielding. Only the ratios of these values are relevant and not the absolute values. The β parameters can be determined based on experimental results of a unidirectional transverse compression test, where the Poisson ratio is measured. The model is validated on unidirectional off-axis compression tests.

Based on the experimentally-detected dependence of polymers on hydrostatic pressure Raghava [53] developed a yield criteria for polymers. A yield criterion for FRP's according to this effect is shown by Vyas [54]. He proposed an adopted Drucker-Prager criterion, taking into account the transverse stress components for hydrostatic sensitivity and assuming linear elastic behavior in fiber direction. The yield function given by Vyas reads:

$$f = \sqrt{\frac{1}{6}(\sigma_{22} - \sigma_{33})^2 + {\sigma_{12}}^2 + N{\sigma_{23}}^2 + {\sigma_{13}}^2 + \frac{\mu}{2}(\sigma_{22} + \sigma_{33})} - \sigma_0. \quad (3\text{-}13)$$

The constant N is introduced to account for the difference in matrix-dominated shear properties. This is not a good solution as a freely selectable parameter N leads to the fact that non transversal isotropic material behavior is assumed. The parameter μ controls hydrostatic sensitivity. The corresponding non-associative plastic potential is introduced in order to correctly reproduce the experimentally measured curves:

$$g = \sqrt{\frac{1}{6}(\sigma_{22} - \sigma_{33})^2 + {\sigma_{12}}^2 + N{\sigma_{23}}^2 + {\sigma_{13}}^2 + \frac{\mu'}{2}(\sigma_{22} + \sigma_{33})}. \quad (3\text{-}14)$$

The model validation is based on experimental determined longitudinal shear stress-strain curves under varies conditions. On the one hand experiments under high hydrostatic pressure [55] provide the data. On the other hand the shear curves have been measured for unidirectional off-axis tests [56].

A rather different modeling approach is presented by Flatscher [14, 57] for plane stress conditions. He distinguishes between two different mechanisms for plastic strain accumulation of in-plane shear and transverse compression. Both mechanisms are considered separately on a specific shear plane oriented on fracture planes defined by Puck`s failure criterion. For both mechanisms, a separate flow rule and its own hardening behavior is assigned. The yield condition for the in-plane shear plasticity reads:

$$f_I = \sigma_I - \tilde{\sigma}_I = 0, \quad (3\text{-}15)$$

where σ_I is the equivalent shear stress and $\tilde{\sigma}_I$ is the yield stress. The equivalent shear stress σ_I is defined piecemeal by

$$\sigma_I = \begin{cases} |\sigma_{12}| + \mu_I^t \sigma_{22} & r_I < 0 \\ |\sigma_{12}| & 0 \le r_I \le \lambda_I, \\ |\sigma_{12}|(1 - \mu_I^c \lambda_I) - \mu_I^c \sigma_{22} & \lambda_I < r_I \end{cases} \quad (3\text{-}16)$$

with a stress ratio $r_I = -\sigma_{22}/|\sigma_{12}|$ and stress interaction parameters μ_I^t, μ_I^c and λ_I. The in-plane shear yield surface is visualized in Fig. 3-7.

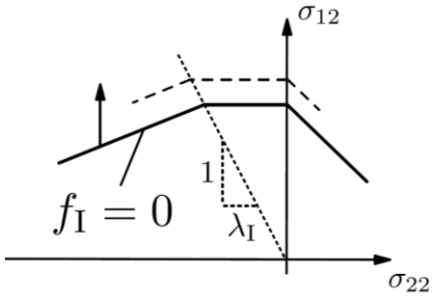

Fig. 3-7: Yield surface for in-plane shear given by [14]

For transverse compressive ply loads, the yield condition reads

$$f_{II} = \sigma_{II} - \tilde{\sigma}_{II} = 0, \tag{3-17}$$

where σ_{II} is the equivalent compressive stress and $\tilde{\sigma}_{II}$ is the yield stress. The equivalent compressive stress σ_{II} is defined for $\sigma_{22} < 0$ by

$$\sigma_{II} = \begin{cases} -\sigma_{22} & r_{II} \leq \lambda_{II} \\ -\sigma_{22}(1 - \mu_{II}\lambda_{II}) + \mu_{II}|\sigma_{12}| & r_{II} > \lambda_{II} \end{cases}, \tag{3-18}$$

With a stress ratio $r_{II} = -|\sigma_{12}|/\sigma_{22}$ and stress interaction parameteres μ_{II} and λ_{II}. The yield surface for transverse compressive plasticity is visualized in Fig. 3-8.

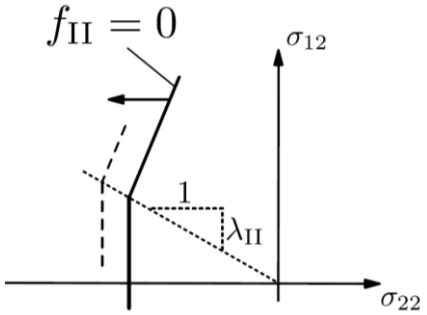

Fig. 3-8: Yield surface for transverse compression given by [14]

The idea to separate yielding is inevitable, especially considering the same development in the field of composite failure. Two separate flow rules allow for the definition of two independent master curves. As an in-plane shear test and a transverse compression test is anyway mandatory as input for an accurate plasticity model, no additional tests are necessary, but both response curves are used as model input. Fully interactive plasticity models, like all others mentioned above, require not less than one material parameter just to ensure that the model can predict the in-plane shear and transverse compressive behavior correctly with only one plastic master curve. Usually, this is only possible if little deviations are accepted for at least one of both test cases.

Although, several material models are available for composite design, it is obvious that there is a lack of experimental verification. The validation of a constitutive model based on a small number of different tests or a barely varying experimental setup with similar loading states in all specimens does not ensure its general applicability. As shown in [52] and [49], fundamentally different plasticity approaches are able to match the same series of unidirectional off-axis compression tests. The basis for the development of the proposed plasticity model was a comprehensive experimental study, see Section 3.6. In the following different probable influencing stress interactions are subjected to a critical discussion based on experimental investigations from literature. Also numerical studies have been done to investigate the effect of possible stress interactions on the prediction of the angle-ply tension and off-axis compression tests, used for validation. As the result of this discussion, a new plasticity model for unidirectional fiber reinforced composites is proposed.

3.3.1 Stress Interaction

In order to define a constitutive model for continuous fiber reinforced plastics, it is essential to evaluate the composites response to a multi-axial stress state. In detail, the influence of uniaxial or biaxial transverse stresses and hydrostatic pressure in combination with longitudinal shear load is discussed concerning the effects on yielding. The influence of multi-axial stress states is estimated from experimental data. Due to the high level of complexity of test rigs generating a specific multi-axial stress state, limited data can be found in literature. Only the influence of a uniaxial transverse stress σ_{22} and hydrostatic pressure on the nonlinear in-plane shear response is addressed. Other data was not available. Some possible test setups for evaluation of further multi-axial stress states, especially mechanical tri-axial tests, are shown in [58], but no data determined from experimental results is currently available.

Several literary sources account for an influence of stresses transverse to the fibers on the shear stress-strain response. A common outcome is the significant dependence of compressive stress on the shear strength of the specimens. In contrast, no consistent result arises for the influence of the nonlinear shear stress-strain behavior under varying transversal load. Both, literature showing an experimental dependency [27, 59] and no dependency [49, 56, 59–61] can be found. Experimental determination of the shear stress-strain behavior is critical as it is highly dependent on how to interpret the results. Moreover, influencing secondary effects like fiber rotation or damage processes for high stress exposures have to be taken into account. Pure shear and normal stresses in the fiber coordinate system are no measureable quantities. Obtained curves are either calculated by analytical models, especially for in-plane biaxial test setups like off-axis compression tests, or calculated from recorded results of force sensors and strain gages. So a detailed description of the experimental setup is very important, when analyzing experimental results.

Vogler and Kyriakides [59] have investigated the nonlinear behavior in shear and transverse compression of unidirectional AS4/PEEK and their interaction. In a custom facility thin strips of the composite were tested under pure shear, pure compression and under biaxial loading history. The tests were performed for three biaxial loading paths. In the first, the specimen was sheared then compressed while the shear stress was held constant. In the second, the specimen was compressed then sheared while the compressive stress was held constant and in the third, the specimen was loaded simultaneously by proportional amounts of compression and shear. Two strain gages placed ±45° in the center of the specimen on opposite sides of it were used to measure the shear strain. The transverse strain was measured by back-to-back gages placed a little outside of the center of the specimen. Due to deformation induced rotation of the ±45° gages during testing this setup results in an error in the measured shear strain. The results of Vogler and Kyriakides are given in Fig. 3-9. They considered a significant effect of the loading path on the material response. For the two types of non-proportional paths applied, the stress held constant did not significantly influence the strain of the increasing stress (Fig. 3-9 a) and b)). In contrast, in the tests with simultaneous increasing of compression and shear loading, an interaction between the two stress components was considered (Fig. 3-9 c) and d)). So the results cannot draw a clear conclusion about the interaction of longitudinal shear and transverse stresses regarding the nonlinear constitutive behavior. It is hard to explain the observed strong influence of the loading path on the material behavior from a physical point of view. A possible explanation for these results provides a critical consideration of the strain measurement method. The deformation induced rotation of the strain gages during the experiments can influence the measured strains. For the tests where the other stress component is applied before the actual measurement of the nonlinear response curve, the deformation caused by that stress results in an initial rotation of the strain gages. In contrast for the tests where both stress components are simultaneously increased, a combination of both stresses drives the rotation of the strain gages. Friction and canting of the linear bearing device could have been another influencing factor.

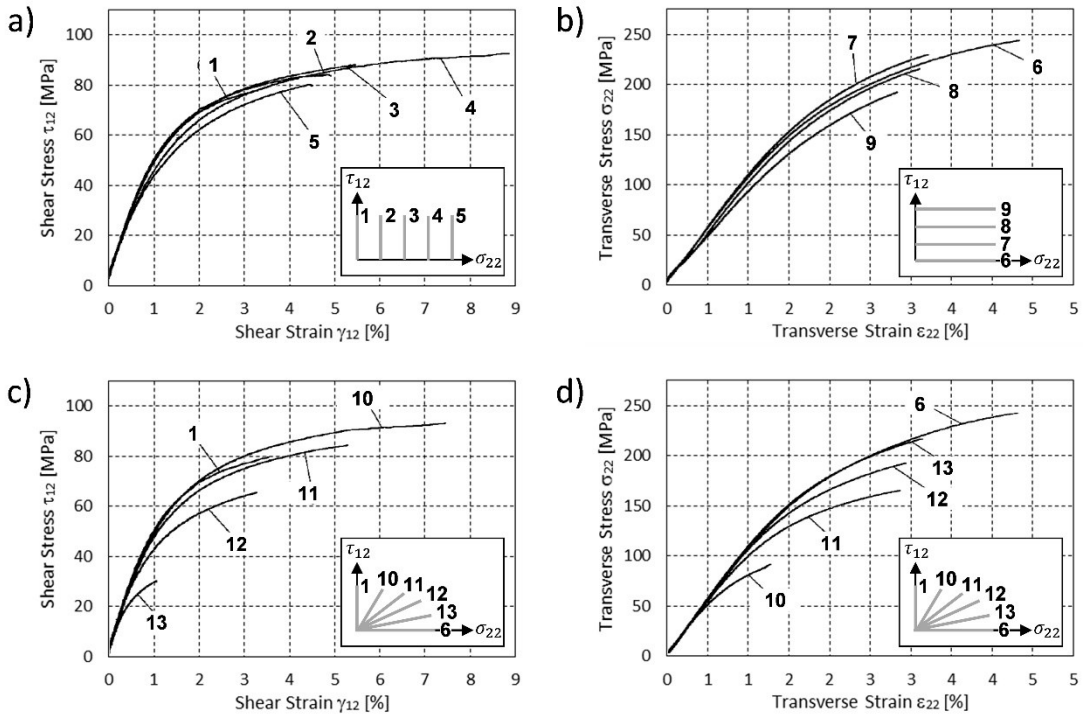

Fig. 3-9: Response of bi-axial loaded AS4/PEEK specimens [59]

a) Shear response under constant transverse compressive loading

b) Transverse compression response under constant shear loading

c) Shear response under simultaneous compression and shear loading

d) Transverse compression response under simultaneous compression and shear loading

Puck and Schürmann [27] presented experimental results of glass-fiber/epoxy specimens loaded under combined transverse and shear loading. They observed a noticeable influence of transverse tensile loading on the shear stress-strain curve, but only minor influence of compressive loading, see Fig. 3-10. As reason for the shallower curves for combined transverse tension and shear loading, they mention additional micro-damage.

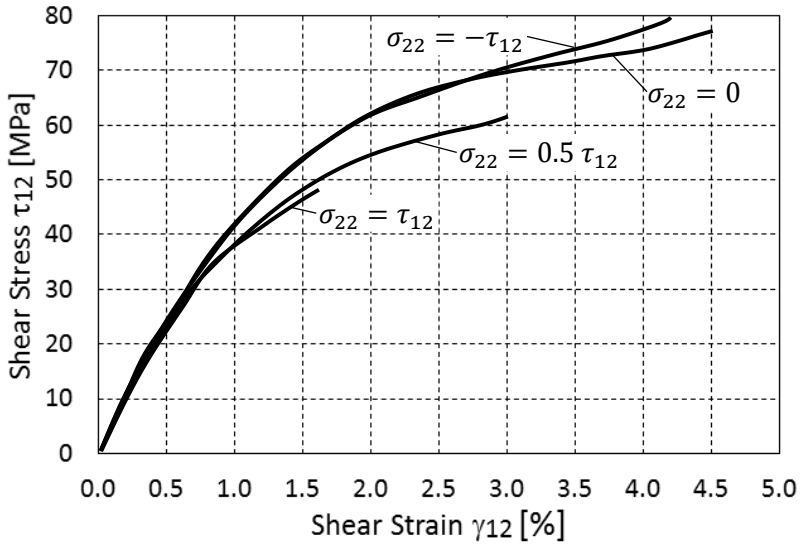

Fig. 3-10: Stress/strain diagrams of unidirectional glass-fiber/epoxy specimens under combined σ_{22}, τ_{12} loading [27]

A further experimental study on the nonlinear behavior in transverse compression and in-plane shear is given by Körber et al. [60]. Quasi-static and dynamic experiments were performed with end-loaded, rectangular off-axis compression specimens made of IM7-8552. The dynamic tests at strain rates up to $350\ s^{-1}$ were performed on a split-Hopkinson pressure bar. In accordance to the end-loading compression (ELC) test standard ASTM D695 [62][62, 62], all specimens had the same nominal dimensions of $20 \times 10 \times 4\ mm^3$. The in-plane strain field of the specimens was obtained via digital image correlation and averaged over a virtual gauge area of $3 \times 3\ mm^2$ for the quasi-staic tests and $6 \times 6\ mm^2$ for the dynamic tests. The stress components σ_2 and τ_{12} were obtained from the applied axial stress by transformation into the material coordinate system. Thereby, the fiber rotation during the test, which was provided by the DIC software, was considered. The in-plane shear response of all specimens is given in Fig. 3-11. All curves lie close to each other until failure, even though depending on the off-axis angle different transverse compression stresses were acting.

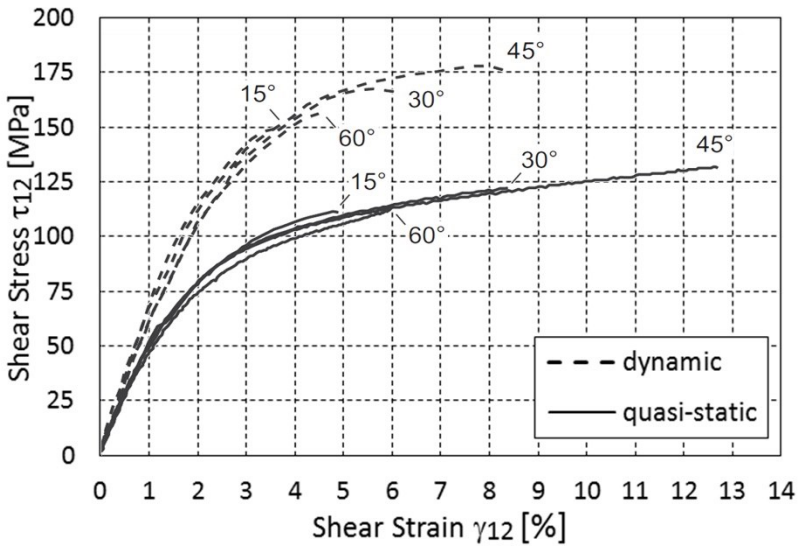

Fig. 3-11: In-plane shear response of unidirectional IM7-8552 off-axis compression specimens [60]

Swanson et al. [56] investigated the interaction of stress states leading to matrix failure. They performed a series of tests involving torsional shear combined with axial tension or compression of unidirectional hoop wound cylinders, using AS4/55A carbon/epoxy. The inside diameter of the specimens was nominally 96.5 mm, the wall thickness was 2.5 mm and the gage section was 50 mm long. The ends of the tubes were reinforced and connected to aluminum end plates, to avoid stress concentrations. The cylinders were wound at an angle of 1.14° from the hoop direction. So loading the specimens leads to a small stress in fiber direction beside the investigated transverse and shear stresses. For simplicity, the small value of σ_{11} was negelcted. The test procedure was to apply the transverse stress σ_{22} first, followed by the shear stress. Strains were measured by 3-gage rosettes on each specimen. In Fig. 3-12 the results of the test series are given.

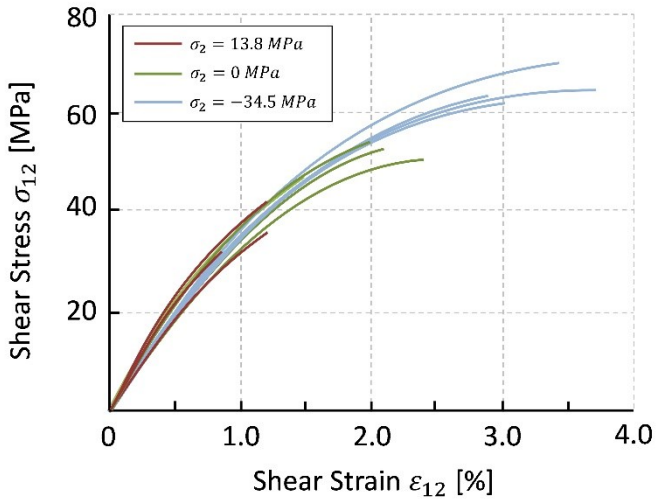

Fig. 3-12: Shear stress-strain response from combined torsional and compression load for AS4-55A [56]

Another explanation for an influence of transverse loading on the shear behavior is given in [61]. Especially in the loading history, shortly before specimen failure, micro-damage processes and hackle markings cause a substantial effect on yielding.

Plastics are hydrostatic pressure sensitive, which denotes a compressibility caused by molecular processes within the polymer chains. Hydrostatic pressure causes several effects on the shear stress-strain response of a neat resin [55, 63]. There is a moderate increase in shear modulus of the stress-strain curve with increasing pressure and there is a more obvious substantial increase in the failure stress for high pressure loads. Experiments indicate the same effect of hydrostatic sensitivity for FRP`s but at a reduced scale in comparison to neat resins [55, 63, 64]. The ultimate failure of the specimens is delayed by an applied hydrostatic pressure. Thus, higher nonlinear strains can be obtained.

An experimental investigation of the influence of superimposed hydrostatic pressure on the mechanical behavior of carbon fiber epoxy composites has been done by Pae [64]. He conducted compression tests of unidirectional 90° and 45° specimens inside a thick-walled high pressure vessel. As pressure-transmitting fluid silicon oil was used. This setup allowed for the measurement of nominal stress-strain curves under various hydrostatic pressures up to 4kbar. All specimens were made of the prepreg tape Scotchply SP-319 from 3M Company. The experimental results are given in Fig. 3-13.

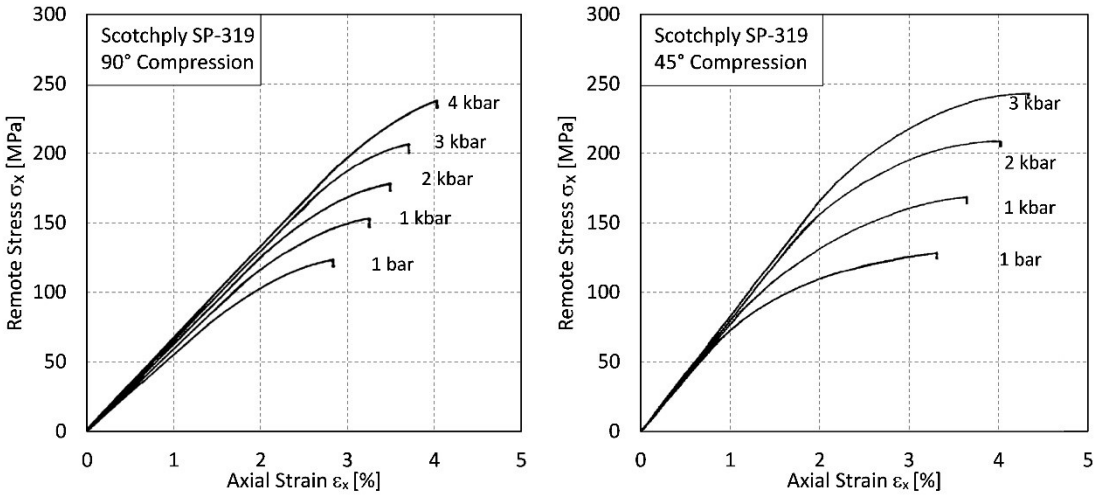

Fig. 3-13: Axial response of transverse and 45° off-axis compression specimens under various hydrostatic pressure for Scotchply SP-319 [64]

Notably, considerable interaction requires an additional hydrostatic pressure in range of hundreds of MPa. Corresponding experimental studies were obtained by a special test setup, applicable for a high-pressure fluid in the test environment. This provides an entire ambient pressure state for determination of the compressibility properties. Under standard atmospheric conditions, a possible hydrostatic stress component in the resin of uniaxial loaded tension specimens is considerably lower. For the investigation of an influence of the hydrostatic pressure on the material behavior of the respective lamina, the smeared plane stress state is not sufficient. Therefore, a micromechanical model is required to correlate the stress state acting in the matrix to the smeared stress state of the composite. A further important aspect for formulating a three-dimensional constitutive law is the correct representation of the volumetric change.

The objective of the presented plasticity model is to represent the nonlinear material behavior of continuous fiber reinforced plastics accurately even at large deformations. The accurate prediction of the complex three dimensional stress state acting at the critical area of a structural part is a basic requirement for a sensible failure analysis. Simultaneously, the number of required parameters shall be kept as low as possible. As shown in Fig. 3-14 different mechanisms, in relation to the stress components, promote yielding caused by directional straightening of polymer chains. Due to longitudinal shear, sliding of fibers and resin occurs longitudinally. In contrast, the yield processes in reaction to transverse loading are taking place perpendicularly to the fibers. It follows that two master curves representing the effective stress-strain behavior for both mechanism are required for modelling plasticity.

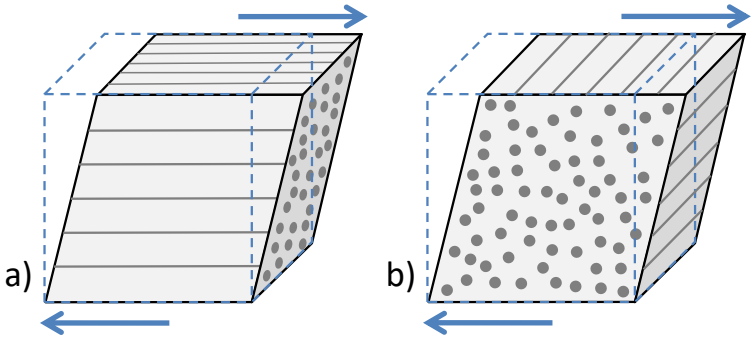

Fig. 3-14: Yielding for a) longitudinal shear and b) transverse plasticity

In previous experimental and numerical studies regarding multi-axial stress interactions, a direct interaction of the transverse stress σ_{22} and the in-plane shear stress σ_{12} was not observed [32]. However, for three dimensional stress states it is not reasonable to disregard any interaction between the individual stress components. Instead, the proposed three dimensional model assumes transversal isotropic material behavior and accounts for an interaction of certain stress components in a partly interactive formulation. Separate flow rules are defined for transverse loading and for longitudinal shear.

For the interaction of the transverse stress components to an equivalent stress, the von Mises criterion (maximum distortion energy theory) or the Tresca criterion (maximum shear stress theory) are suitable in principle. Using the von Mises stress would cause the problem that under pure hydrostatic loading of the composite ($\sigma_{11} = \sigma_{22} = \sigma_{33}$) the equivalent stress would not be zero, see Eq. (3-20). This would result in a plastic change of the cross-sectional area transverse to the fibers and therefore in a physically pointless plastic volumetric change. For the Tresca criterion, see Eq. (3-21) this effect does not occur, so the equivalent stress according to Tresca is used for the interaction of the stress components acting perpendicular to the fibers. To account for hydrostatic sensitivity, the yield function contains a hydrostatic sensitivity factor multiplied with the hydrostatic stress in addition to the equivalent stress. That formulation is similar to the Drucker-Prager criterion [46]. The hydrostatic stress acting in the matrix, estimated by a simple micromechanical model, see Eq. (3-22), is used, as the resin is the driver for the hydrostatic sensitivity of the composite.

The plastic deformation due to longitudinal shear is described by a separate yield function. To enable transversal isotropic behavior, the equivalent stress is defined as a quadratic superposition of both longitudinal shear stress components (σ_{12} and σ_{13}), see Eq. (3-30). An direct interaction between longitudinal shear and transverse stresses is not assumed, as this would result in a deterioration of the model‘s prediction quality. The hydrostatic sensitivity of the longitudinal shear behavior is considered in terms of a non-associative flow rule, similar to transverse plasticity. It is possible that for lower

fiber volume fractions, longitudinal shear and transverse load influence each other more strongly in comparison to the material investigated in this study.

3.3.2 Transverse Plasticity

This section describes the plastic flow, caused by stress components acting perpendicular to the fibers ($\sigma_{22,}\ \sigma_{33}, \sigma_{23}$). The corresponding yield function is defined as

$$f_{tr} = \tilde{\sigma}_{tr} = \sigma_{tr}^{eq} + \alpha_{tr}\ \sigma_m, \tag{3-19}$$

where σ_{tr}^{eq} is the equivalent plastic stress, α_{tr} is the hydrostatic pressure sensitivity and σ_m is the hydrostatic stress. The effective plastic stress $\tilde{\sigma}_{tr}$ is defined equal to the yield function.

Following the assumption of isotropic material behavior in the 2-3 plane, equivalent plastic stress formulations, typically used for isotropic materials, like the von Mises yield criterion or the Tresca yield criterion are suitable in principle. In the case of plane stress the von Mises criterion reads:

$$\sigma_{tr}^{eq} = \sqrt{\sigma_{22}^2 + \sigma_{33}^2 - \sigma_{22}\sigma_{33} + 3\sigma_{23}^2}. \tag{3-20}$$

Using the von Mises stress leads to the problem that under pure hydrostatic loading ($\sigma_{11} = \sigma_{22} = \sigma_{33}$) the equivalent stress would not become zero. This would cause a plastic change of the cross-sectional area transverse to the fibers and therefore to a physically pointless plastic volumetric change. In other word, a composite specimen would strongly shrink under hydrostatic pressure. So the plane stress formulation of the von Mises criterion is not suitable for the interaction of the stress components acting in the plane transverse to the fibers. The plane stress formulation of the Tresca criterion reads:

$$\sigma_{tr}^{eq} = \sqrt{\sigma_{22}^2 + \sigma_{33}^2 - 2\sigma_{22}\sigma_{33} + 4\sigma_{23}^2}. \tag{3-21}$$

Substituting the condition $\sigma_{22} = \sigma_{33}$ and $\sigma_{23} = 0$ in Eq. (3-20), the Tresca equivalent stress becomes zero. So the problem of a plastic volumetric change under pure hydrostatic loading of the composite is not present when using the Tresca criterion. The Tresca yield criterion only accounts for stress states resulting in a distortion of the cross-section located transverse to the fibers. In the presented model the equivalent plastic stress according to Tresca is used.

The hydrostatic stress sensitivity of fiber reinforced composites is driven by the matrix. Therefore, the hydrostatic stress acting in the matrix is used to control hydrostatic sensitivity of the composite. To estimate the stress in fiber direction acting in the matrix,

the smeared stress σ_{11} is converted by the stiffness ratio. Transverse to the fibers the stresses in the matrix are assumed to be equal to the smeared stresses of the composite. The hydrostatic stress acting in the matrix σ_m follows:

$$\sigma_m = \frac{1}{3}\left(\frac{E_m}{E_1}\sigma_{11} + \sigma_{22} + \sigma_{33}\right). \tag{3-22}$$

The parameter α_{tr} can be determined by a transverse compression test under various hydrostatic pressures. In Section 3 simulated and experimentally measured results are given. Additionally, the sensitivity of α_{tr} is discussed.

The plastic potential used for the flow rule is defined based on the yield function Eq. (3-19). To allow for a non-associative flow, β_{tr} is used as hydrostatic sensitivity parameter:

$$g_{tr} = \sigma_{tr}^{eq} + \beta_{tr}\,\sigma_m. \tag{3-23}$$

The parameter β_{tr} influences the volumetric change of the material during plastic flow. For an isotropic material, the constant β_{tr} can be related to the plastic Poisson's ratio ν_p, assuming a uniaxial compression in the z-direction of the material [65]. In the same way a reliable value for composites could be determined by measuring the lateral contraction in both directions during a unidirectional 90° compression test. In Section 3.3.5 the sensitivity of β_{tr} is discussed. The incremental plastic strain can be written in terms of the plastic potential g_{tr}:

$$d\boldsymbol{\varepsilon}_{tr}^{p} = \frac{\partial g_{tr}}{\partial \boldsymbol{\sigma}}\, d\lambda_{tr}, \tag{3-24}$$

where the subscript p denotes plasticity, and $d\lambda_{tr}$ is a proportionality factor. The equivalent plastic strain is defined as

$$\tilde{\varepsilon}_{tr}^{p} = \frac{1}{2}\sqrt{d\boldsymbol{\varepsilon}_{tr}^{p} : d\boldsymbol{\varepsilon}_{tr}^{p}}. \tag{3-25}$$

The factor $1/2$ in Eq. (3-25) allows for direct measurement of the $\tilde{\sigma}_{tr}$-$\tilde{\varepsilon}_{tr}^{p}$ master curve given by the axial response of a unidirectional transverse compression test. The plastic multiplier $d\lambda_{tr}$ is calculated by substituting Hook's law Eq. (3-2) into the consistency condition given by:

$$0 = \frac{\partial f_{tr}}{\partial \boldsymbol{\sigma}}\, d\boldsymbol{\sigma} + \frac{\partial f_{tr}}{\partial \tilde{\varepsilon}_{tr}^{p}}\, d\tilde{\varepsilon}_{tr}^{p}. \tag{3-26}$$

By substituting Eq. (3-1) and Eq. (3-24) into Eq. (3-2), the stress increment can be written as

$$d\boldsymbol{\sigma} = \boldsymbol{C}^e \left(d\boldsymbol{\varepsilon} - \frac{\partial g_{tr}}{\partial \boldsymbol{\sigma}} d\lambda_{tr} \right) \tag{3-27}$$

and the plastic multiplier can be determined by substituting Eq. (3-24), Eq. (3-25) and Eq. (3-27) into Eq. (3-26):

$$d\lambda_{tr} = \frac{2 \frac{\partial f_{tr}}{\partial \boldsymbol{\sigma}} \boldsymbol{C}^e d\boldsymbol{\varepsilon}}{\frac{\partial \tilde{\sigma}_{tr}}{\partial \tilde{\varepsilon}^p_{tr}} \sqrt{\frac{\partial g_{tr}}{\partial \boldsymbol{\sigma}} : \frac{\partial g_{tr}}{\partial \boldsymbol{\sigma}}} + \frac{\partial f_{tr}}{\partial \boldsymbol{\sigma}}^T \boldsymbol{C}^e \frac{\partial g_{tr}}{\partial \boldsymbol{\sigma}}}. \tag{3-28}$$

3.3.3 Longitudinal Shear Plasticity

To describe the plastic deformation caused by longitudinal shear stresses (σ_{12}, σ_{13}), the following yield function is defined:

$$f_{sl} = \tilde{\sigma}_{sl} = \sigma_{sl}^{eq} + \alpha_{sl}\, \sigma_m, \tag{3-29}$$

where the index sl denotes longitudinal shear. The equivalent stress σ_{sl}^{eq} is defined as

$$\sigma_{sl}^{eq} = \sqrt{\sigma_{12}^2 + \sigma_{13}^2} \tag{3-30}$$

and the hydrostatic stress is already given by Eq. (3-22). In the proposed model, the authors assume that plastic flow caused by longitudinal shear stresses has no influence on the volumetric change of the material. Hence the plastic potential is set to be equal to the equivalent stress

$$g_{sl} = \sigma_{sl}^{eq}. \tag{3-31}$$

The equivalent plastic longitudinal shear strains can be written in terms of the plastic potential g_{sl} as

$$d\boldsymbol{\varepsilon}_{sl}^p = \frac{\partial g_{sl}}{\partial \boldsymbol{\sigma}} d\lambda_{sl}, \tag{3-32}$$

where $d\lambda_{sl}$ is the plastic multiplier for longitudinal shear. The equivalent plastic strain is defined as

$$\tilde{\varepsilon}_{sl}^p = \sqrt{d\boldsymbol{\varepsilon}_{sl}^p : d\boldsymbol{\varepsilon}_{sl}^p}. \tag{3-33}$$

The consistency condition for longitudinal shear plasticity reads

$$0 = \frac{\partial f_{sl}}{\partial \boldsymbol{\sigma}} d\boldsymbol{\sigma} + \frac{\partial f_{sl}}{\partial \tilde{\varepsilon}_{sl}^{p}} d\tilde{\varepsilon}_{sl}^{p}. \tag{3-34}$$

The plastic multiplier can be calculated in the same way then for transverse plasticity. As the stress increments $d\sigma_{11}$, $d\sigma_{22}$, $d\sigma_{33}$ and $d\sigma_{23}$ are affected by the transverse plasticity, they need to be calculated by Eq. (3-27) before $d\lambda_{sl}$ can be determined:

$$d\lambda_{sl} = \frac{\frac{\alpha_{sl}}{3}\left(\frac{E_m}{E_1} d\sigma_{11} + d\sigma_{22} + d\sigma_{33}\right) + \frac{G_{12}}{\sigma_{sl}^{eq}}\left(\sigma_{12} d\varepsilon_{12} + \sigma_{13} d\varepsilon_{13}\right)}{\frac{\partial \tilde{\sigma}_{sl}}{\partial \tilde{\varepsilon}_{sl}^{p}} \sqrt{\frac{\partial g_{sl}}{\partial \boldsymbol{\sigma}} : \frac{\partial g_{sl}}{\partial \boldsymbol{\sigma}}} + \frac{\partial f_{sl}}{\partial \boldsymbol{\sigma}}^{T} \boldsymbol{C}^{e} \frac{\partial g_{sl}}{\partial \boldsymbol{\sigma}}}. \tag{3-35}$$

3.3.4 Experimental Determination of the Master Curves

For the determination of plastic strains, two independent master curves are sufficient. The master curves define the hardening behavior by a relation between effective stress and effective plastic strain and are required as input for transverse and for longitudinal shear loading, respectively. Within the implemented *ABAQUS VUMAT*, a tabular input of the master curves is provided. The plasticity model requires the slop of the master curve at the current equivalent plastic stress for the calculation of $d\lambda$ (see Eq. (3-28) and Eq. (3-35)). In order to simplify the search of the current position on the master curve, the tabular input provides the equivalent plastic strain for each whole-numbered equivalent plastic stress.

The hardening behavior for transverse loading can be measured in a unidirectional 90° compression test, as the compressive strength of FRP`s is much higher in comparison to the tensile strength. During this test, a hydrostatic stress state in the matrix occurs. Hence, the hydrostatic sensitivity parameters α_{tr} and β_{tr} influence the model's prediction under pure transverse loading in addition to the master curve. So the master curve has to be determined by iterative adaption according to the chosen hydrostatic sensitivity parameters.

The experimental determination of the longitudinal shear master curve, directly determinable through the pure shear stress-strain curve, is more difficult. A proposed procedure is shown in ASTM D 3518 [39] but is limited to small axial specimen strains. For larger strains, the $\pm 45°$ angle-ply response is influenced by damage processes and fiber rotation. Specimens providing pure longitudinal shear σ_{12} are not suitable, as failure occurs prematurely compared to a combined shear and compression stress state. A master curve for a sufficient large strain range can be prepared based on a tensile test of a $\pm 40°$ angle-ply laminate. This kind of laminate in combination with an adequate width is not influenced by damage. Due to occurring transverse and longitudinal stress components the longitudinal shear behavior cannot be measured directly. However, the

longitudinal shear master curve can be determined by an iterative fitting process. The master curves applied in the presented study for IM7-8552 and Scotchply SP-319 are shown in Fig. 3-15 and Fig. 3-16.

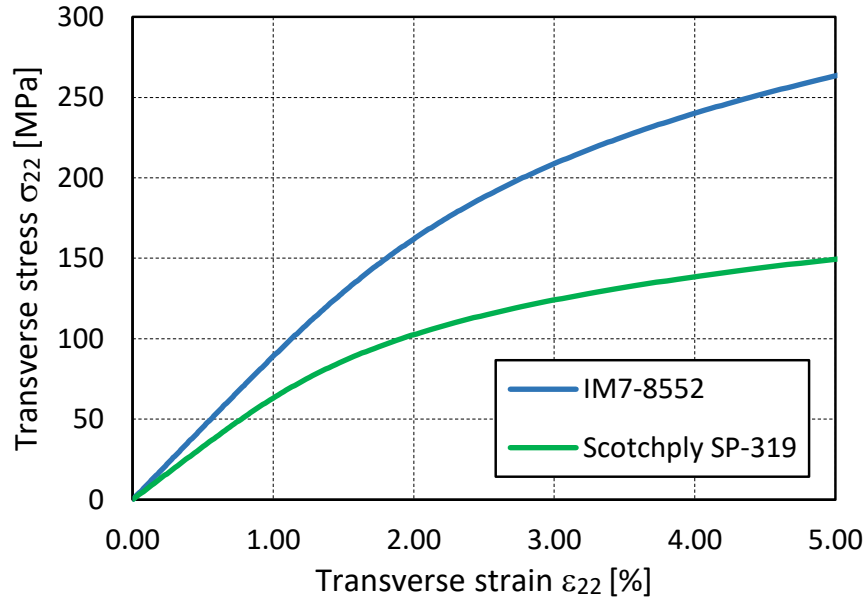

Fig. 3-15: Master curves for transverse plasticity

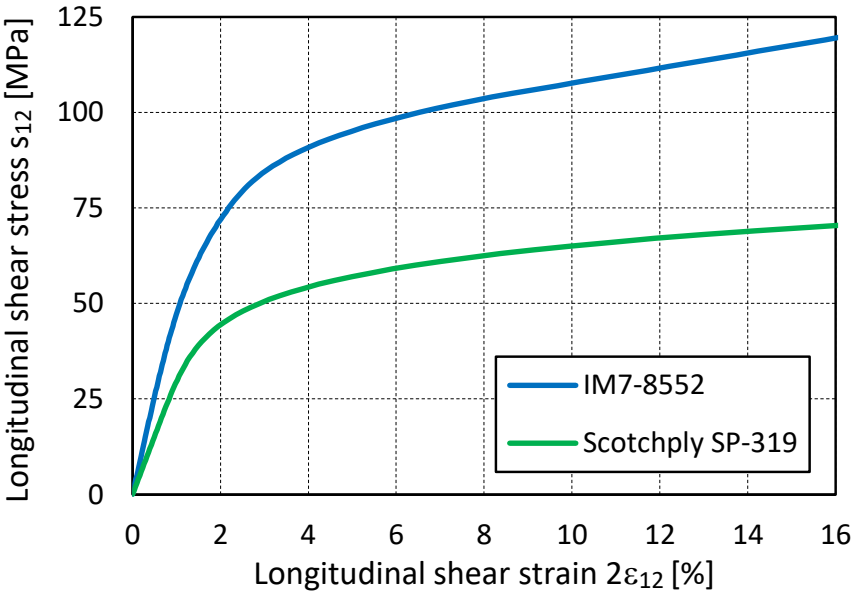

Fig. 3-16: Master curves for longitudinal shear plasticity

3.3.5 Verification of the Hydrostatic Sensitivity

In the following, the influence of the hydrostatic sensitivity parameters is discussed on the basis of several experiments. In Section 3.6, a compressive validation of the

hardening model is based on experimental results of angle-ply tension and unidirectional off-axis compression specimens made of Hexply IM7-8552. Unfortunately, experimental investigations under high hydrostatic pressure are not available for this material. Therefore, the verification of the hydrostatic sensitivity is based on experimental results for another carbon epoxy prepreg material Scotchply SP-319. Pae performed compression tests of unidirectional 45° and 90° specimens under various levels of hydrostatic pressure [64]. These results are used to derive the material parameters describing the hydrostatic sensitivity. The hydrostatic sensitivity parameters determined for Scotchply SP-319 are also used as an estimate for IM7-8552.

3.3.5.1 Model Calibration based on Scotchply SP-319

An experimental investigation of the influence of superimposed hydrostatic pressure on the mechanical behavior of carbon fiber epoxy composites has been done by Pae [64]. He conducted compression tests of unidirectional 90° and 45° specimens inside a thick-walled high pressure vessel. As pressure-transmitting fluid silicon oil was used. This setup allowed for the measurement of nominal stress-strain curves under various hydrostatic pressures up to 4kbar. All specimens were made of the prepreg tape Scotchply SP-319 from 3M Company. The experimental results are given in Fig. 3-17 and Fig. 3-18. For numerical predictions, a corresponding finite element model was developed. According to the tests the simulations are done in two steps. In a first step, the hydrostatic pressure is applied on all surfaces of the specimen. In the following second step the compression is applied by kinematic boundary conditions on the top and bottom surface of the specimen. The lateral contraction of the specimen is not constrained even at the specimen ends. The stiffness parameters used in the simulations are taken from [64]. The hydrostatic sensitivity parameters α_{tr} and α_{sl} were derived from the experimental results as covered below. First the master curves for the longitudinal shear and for the transverse plasticity were defined based on the results under atmospheric conditions. Then the parameters α_{tr} and α_{sl} have been chosen by iterative adjustment with the objective to optimize the correlation between the predicted and experimental measured curves for the various hydrostatic pressure conditions.

During a unidirectional 90° compression test, a hydrostatic stress state in the matrix occurs. Hence, the hydrostatic sensitivity parameters α_{tr} and β_{tr} influence the model's prediction under pure transverse loading in addition to the master curve itself. So the master curve for transverse plasticity has to be iteratively adapted when changing the hydrostatic sensitivity parameters. As shown in Fig. 3-17 and Fig. 3-18 hydrostatic sensitivity parameters could be found that allow for a good correlation between the numerical and the experimental results. The hydrostatic sensitivity parameter β_{tr}, introduced for the plastic potential, was set to be zero, as discussed in Section 3.3.5.4.

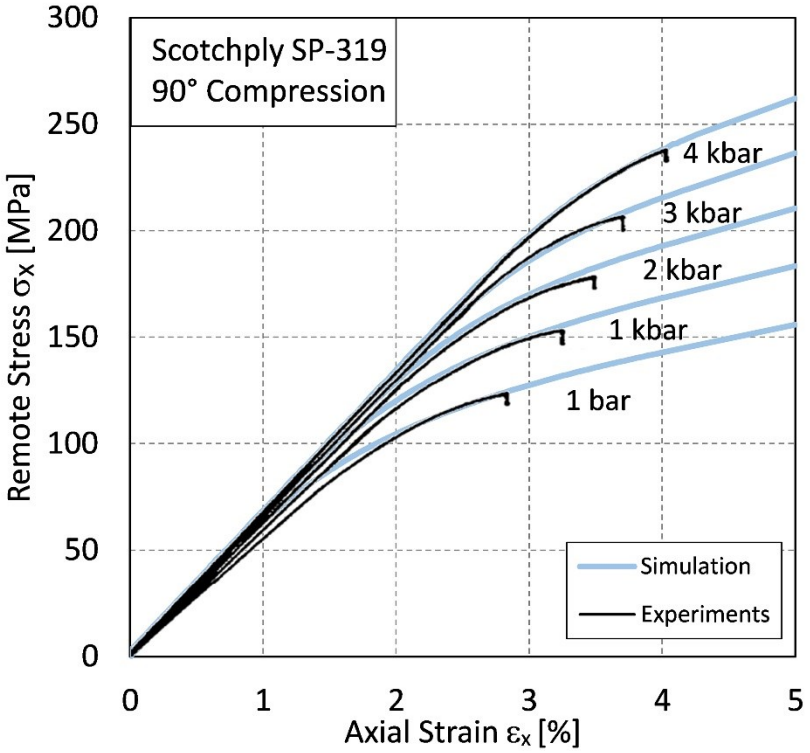

Fig. 3-17: **Transverse compression stress-strain response for Scotchply SP-319 at various hydrostatic pressures, experimental data from [64]**

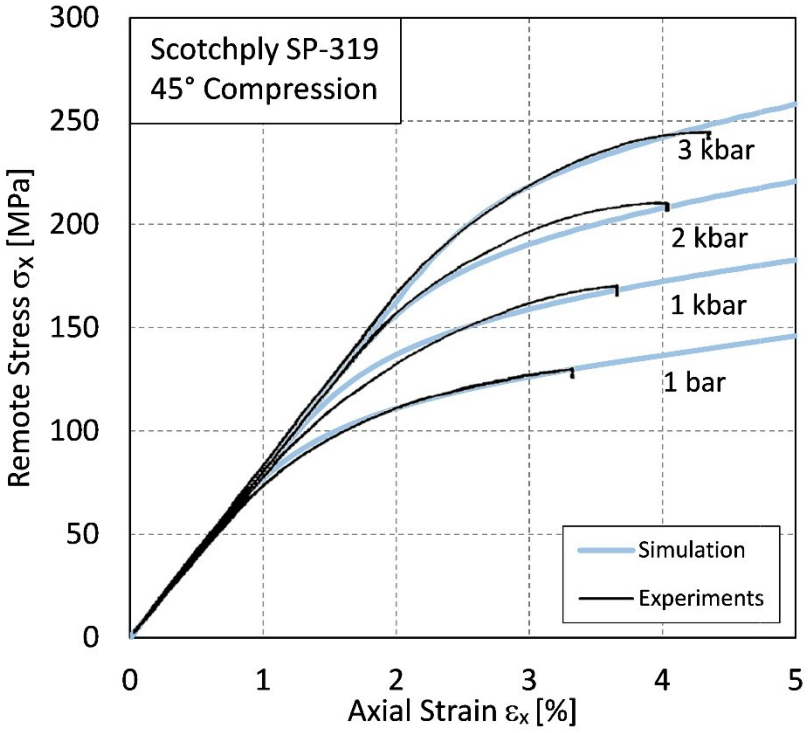

Fig. 3-18: **45° off-axis compression stress-strain response for Scotchply SP-319 at various hydrostatic pressures, experimental data from [64]**

3.3.5.2 Model Predictions for Hexply IM7-8552

In literature many experimental results can be found for the material IM7-8552. Therefore, the validation of the proposed constitutive model is based on that material system. However, for this material system no experimental data concerning the influence of high hydrostatic pressure is available. The hydrostatic sensitivity parameters α_{tr}, β_{tr} and α_{sl}, determined for Scotchply SP-319 (see Section 3.3.5.1), are therefore also used for IM7-8552 as an estimate, as both material systems are carbon fiber reinforced epoxy. The material parameters used in the simulation are given in Table 3-1. The unidirectional 90° and 45° compression tests under various hydrostatic pressure conducted by Pae [64] for Scotchply SP-319 have been simulated for IM7-8552. In Fig. 3-19 and Fig. 3-20 the assumed results under various levels of hydrostatic pressure are presented together with experimental results under atmospheric conditions.

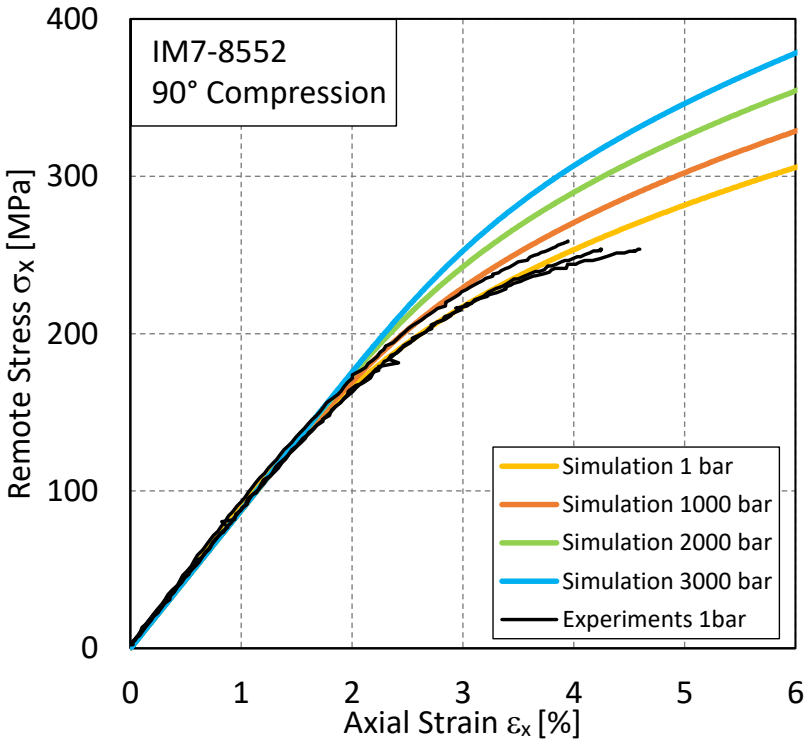

Fig. 3-19: Predicted transverse compression stress-strain response for IM7-8552 at various hydrostatic pressures, experimental data from [60]

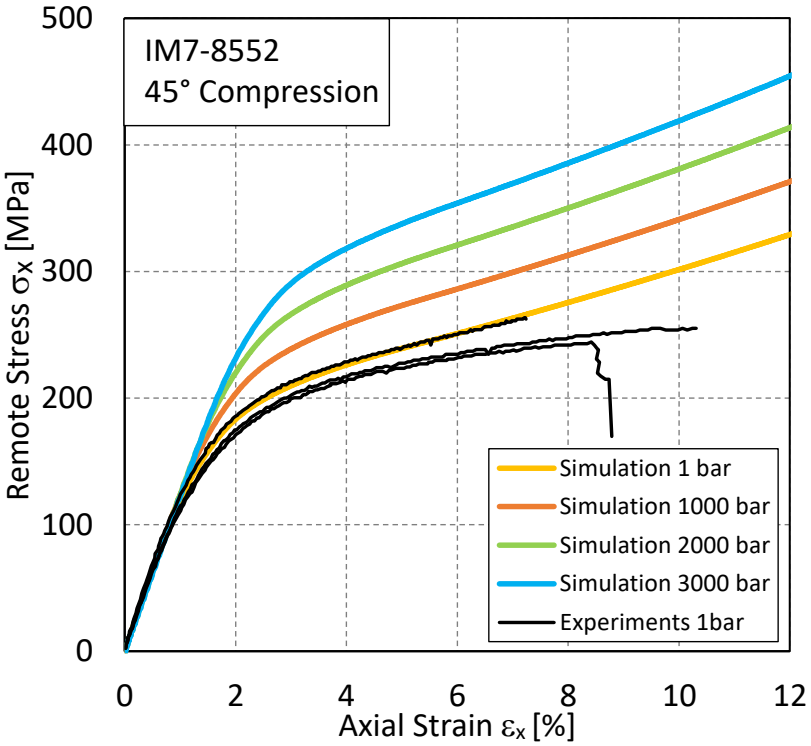

Fig. 3-20: Predicted 45° off-axis compression stress-strain response for IM7-8552 at various hydrostatic pressures, experimental data from [60]

For further discussion of the hydrostatic sensibility, results for the $\pm 30°$ laminate and for the $\pm 40°$ laminate are shown in Fig. 3-21 and Fig. 3-22 respectively. As the laminate layup is symmetric to the mid-plane, except for the edge zones a plane stress state is acting in the specimens. In Fig. 3-21 and Fig. 3-22 additionally to the axial response the hydrostatic stress acting in the matrix, calculated by Eq. (3-22) is given. As the ratio between the longitudinal stiffness of the composite E_1 and the stiffness of the neat resin E_M is very small, the hydrostatic stress, acting in the matrix, is nearly proportional to the transverse normal stress σ_{22}. Shortly before failure, the hydrostatic pressure in the resin is in the range from 70MPa to 80MPa.

At an intermediate state of the material model hydrostatic sensitivity was neglected. Nevertheless, this model is able to predict the axial response of the angle-ply laminates even at large deformations [32]. It is important to understand, why the models with and without considering hydrostatic sensitivity are both able to predict the experimental results. The prediction of plastic deformation caused by σ_{22} is nearly the same for both models. The transverse plasticity master curve for the three-dimensional model already accounts for the hydrostatic stress acting during a unidirectional transverse compression test. And the influence of the longitudinal normal stress σ_{11} is very slight as mentioned above. So a difference in the prediction of both models can only result due to longitudinal shear plasticity. However, during the angle-ply tests the hydrostatic pressure in the matrix is not constant, but increases with loading. At the beginning of the

test the hydrostatic pressure is too small to effect the model prediction noticeable. Another reason, why both models provide similar results, is that the longitudinal shear master curve for the model considering hydrostatic sensitivity differs slightly from the master curve of the model neglecting hydrostatic sensitivity. At high stress levels a flatter curve results for the model with hydrostatic sensitivity from its derivation process from experimental results of ±40° laminate tension tests, see Section 3.3.4. So the master curve compensates the influence of the hydrostatic pressure. This difference in the longitudinal shear master curve concerns stress levels under which pure shear loaded specimens would have been collapsed. Such high shear stresses can only be achieved by concurrent transverse compressive loading. This is why the master curve can't be measured directly from experiments, but can be derived from ±40° laminates.

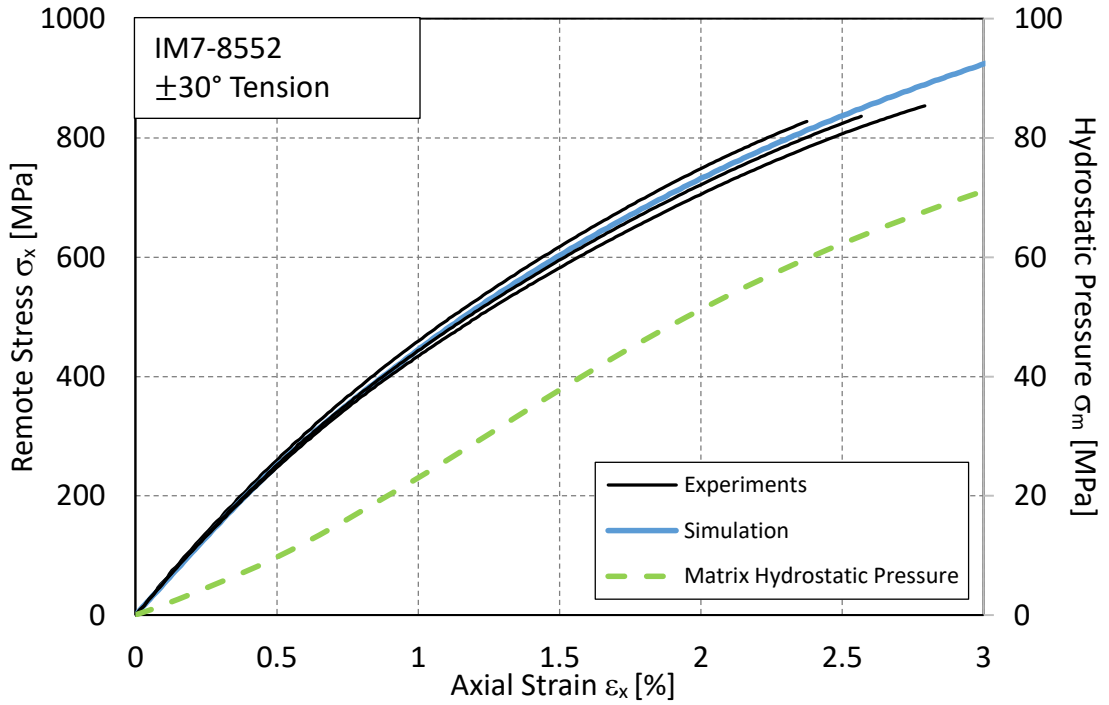

Fig. 3-21: Axial stress-strain response and matrix hydrostatic pressure of ±30° tension specimens for IM7-8552

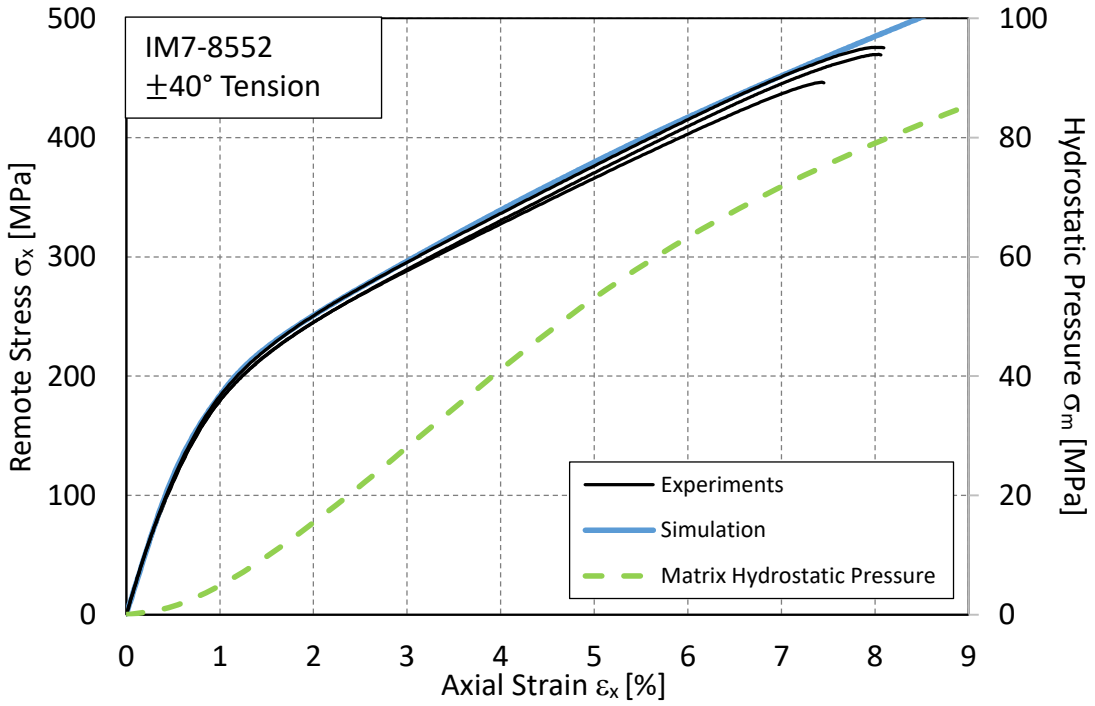

Fig. 3-22: Axial stress-strain response and matrix hydrostatic pressure of ±40° tension specimens for IM7-8552

3.3.5.3 Sensitivity of α

To visualize the sensitivity of the parameter α, the unidirectional 45° compression tests have been simulated under a hydrostatic pressure of 3kbar and under atmospheric conditions with doubled α_{tr} and α_{sl}. The results are shown in Fig. 3-23 in comparison to the results using the original values. The impact of the hydrostatic sensitivity parameters α_{tr} and α_{sl} on the axial response of the specimens is much stronger under high hydrostatic pressure. This is why experiments under high hydrostatic pressure should be used for the determination of the α parameters. A calibration of α based on different in-plane loading conditions is critical and can lead to physically unreasonable values.

An important part for determination of α_{tr} is, that the transverse plasticity master curve needs to be adapted when changing the value of α_{tr}. If no hydrostatic sensitivity is defined ($\alpha_{tr} = 0$), the master curve for transverse plasticity is defined as the axial response of a unidirectional transverse compression test. As the stress component σ_{22} results in a hydrostatic stress acting in the matrix, α_{tr} has an impact on the simulated axial response of this test, see Fig. 3-24. Consistence between the experimentally measured and the simulated response curve must be achieved by adapting the master curve respectively.

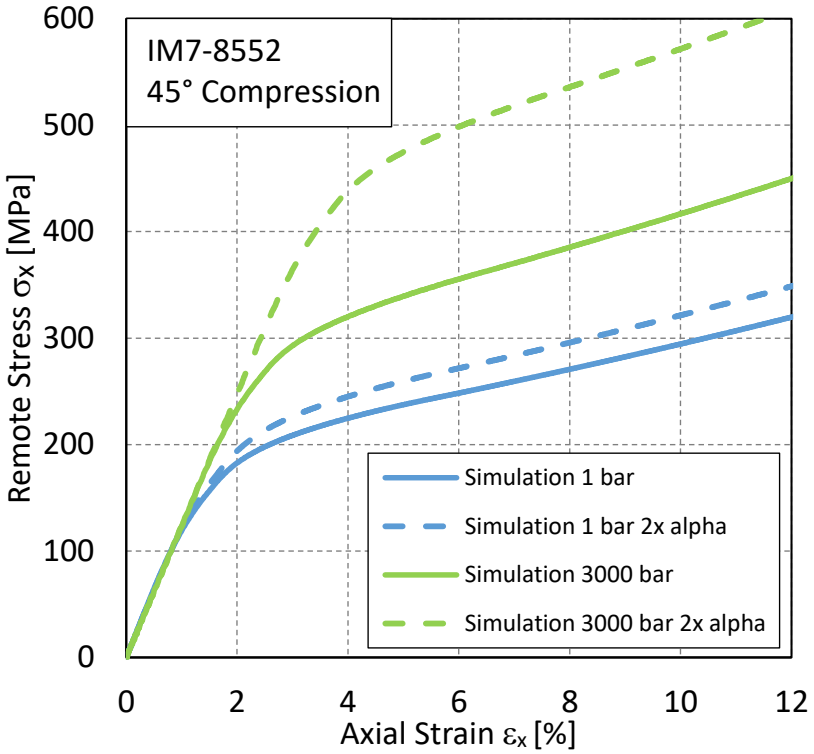

Fig. 3-23: Sensitivity of α for the 45° off-axis compression specimens for IM7-8552

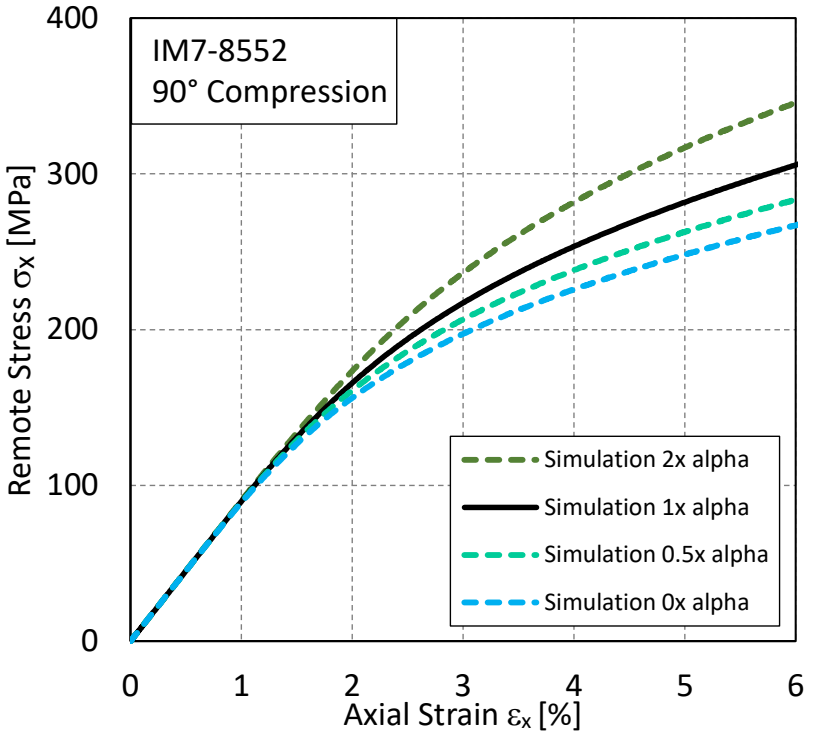

Fig. 3-24: Sensitivity of α for the transverse compression specimens for IM7-8552

3.3.5.4 Sensitivity of β

The hydrostatic sensitivity parameter β_{tr} has only minor influence for in-plane loading conditions. For example, in Fig. 3-25 the predicted result curves of transverse compression tests are given for the two extreme values $\beta_{tr} = \alpha_{tr}$ and $\beta_{tr} = 0$. In this diagram the relative volumetric change is given additionally. The volume change is much more sensitive to the parameter β_{tr}. A reliable value for β_{tr} could be determined by measuring the volumetric change in terms of the lateral contraction in both directions during a transverse compression test. Unfortunately such experimental results are not available for the investigated material. When estimating β_{tr} it must be observed, that adverse values can lead to physically senseless volume changes. If a volume change of the material, induced by the plasticity model, is not desired, it can be eliminated by specifying beta=0.

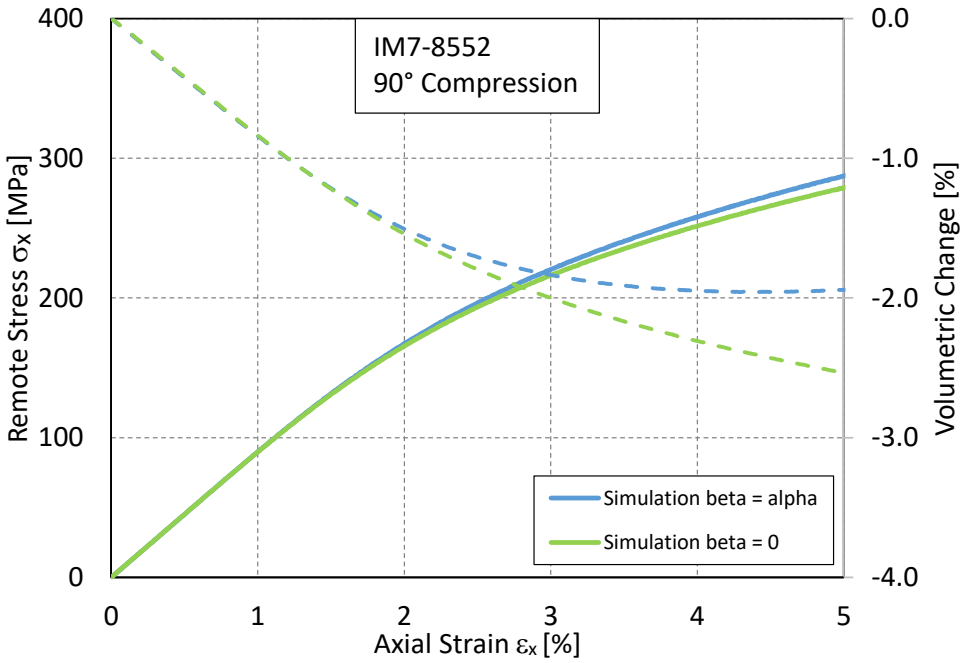

Fig. 3-25: Sensitivity of β for the transverse compression specimens for IM7-8552

3.4 Inter-Fiber Damage

An additional mechanism influencing the constitutive behavior of composite laminates is inter-fiber damage. While fiber failure in at least one ply actually always results in laminate failure, inter-fiber cracks are usually not critical as the surrounding laminate is able to carry the load. Hence, depending on the layup in some plies typically exit multiple inter-fiber cracks at the point of laminate failure. The reason for that is that the transverse tensile failure strain is only about half that for longitudinal tension. But whenever the laminate includes plies orientated in load direction, the stiffness effect of

inter-fiber cracks is negligible small. However, there are also laminates where inter-fiber damage significantly influences the stiffness behavior. For example at $\pm 45°$ tension tests first inter-fiber cracks occurred at an axial strain of 2% while a maximum strain of 14% was reached, see 3.6.4. In this section first inter-fiber failure criteria are presented. Than damage initiation in laminates is discussed followed by the representation of damage evolution in the material model.

3.4.1 Inter-Fiber Failure Criteria

The objective of a failure criterion is to evaluate arbitrary stress states regarding failure. The most important material properties, required by a failure criteria are the strength values for uniaxial loading conditions. For an evaluation regarding inter-fiber cracks these are the transverse tensile strength, the transverse compression strength and the in-plane shear strength.

One opportunity to define a failure criteria is the assumption of a quadratic stress interaction of the individual stress components [66]. Based on constraints like the direction-independence of the shear stress and the known strength values for the single stress components the required interaction parameters can be determined. One of the most famous failure criterion from this group is the Tsai-Wu criterion [25]. A drawback of such mathematical failure criteria is that they cannot provide information about the occurring failure mechanism. Particularly, they provide physically implausible results. Already in 1980 Hashin has noticed that the strength hypotheses of Mohr [67] could provide a physical fundament for an inter-fiber failure condition [26]. The strength hypotheses of Mohr reads: The strength of a material is determined by the stresses acting on the fracture plane. The application of the Mohr hypotheses requires a search operation for the fracture plane. As inter-fiber cracks are always parallel to the fibers just the fracture plane angle needs to be found. Due to the enormous amount of numerical effort this idea was put into practice at a later date by Puck [4, 27, 68]. In the meantime further failure criteria for unidirectional fiber-reinforced composites giving broadly similar predictions are disseminated widely. The main difference between the LaRC criterion [29] and the Puck criterion is the prediction of fiber failure in compression. Therefore, a fiber kinking criterion is proposed by calculating the fiber misalignment under load and applying the matrix failure criterion in the coordinate frame of the misalignment. A further failure criterion very similar is the Cuntze criterion [28, 69] that is based on invariants and therefore does not require to search for the fracture plane angle. However, the fracture plane angle cannot be determined with the Cuntze criterion.

Puck Criterion

The inter-fiber criterion of Puck is described briefly in the following. Detailed information and a comprehensive derivation is given [68] (in German) in and [70] (in English). According to the strength hypothesis of Mohr only the stresses acting on the fracture plane are relevant for failure analysis. Since initially the facture plane angle is

not known, all possible fracture plane angles ($-90° \leq \theta_f \leq 90°$) have to be examined. In a first step the stress state acting on the possible fracture plane ($\sigma_n, \sigma_{n1}, \sigma_{nt}$) therefore needs to be determined:

$$\sigma_n = \cos^2(\theta)\sigma_{22} + \sin^2(\theta)\sigma_{33} + 2\sin(\theta)\cos(\theta)\,\sigma_{23}, \tag{3-36}$$

$$\sigma_{n1} = \cos(\theta)\,\sigma_{12} + \sin(\theta)\,\sigma_{13}, \tag{3-37}$$

$$\sigma_{nt} = \sin(\theta)\cos(\theta)\,(\sigma_{33} - \sigma_{22}) + \left(\cos^2(\theta) - \sin^2(\theta)\right)\sigma_{23}. \tag{3-38}$$

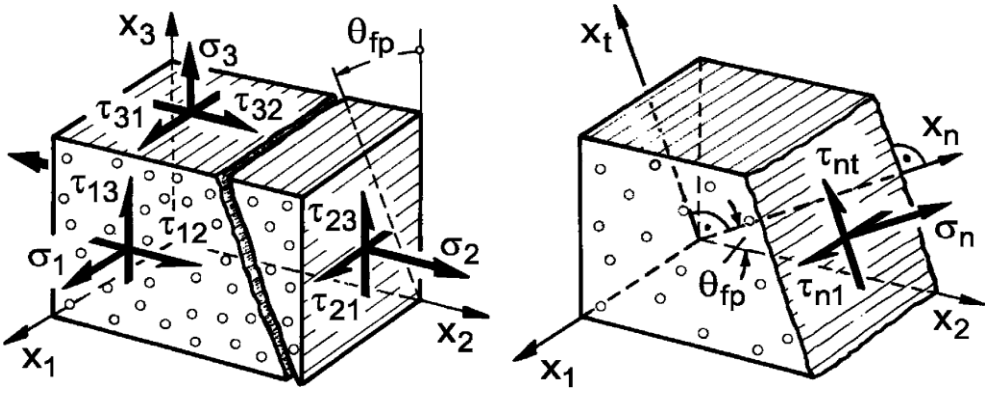

Fig. 3-26: Stresses of the UD-lamina and stresses on a possible (IFF)-fracture plane [70]

The strength values according to the single stress components of the possible fracture plane are required, when defining fracture conditions. For the normal stress component it has to be differentiated between tension and compression. If only a compressive stress is acting on a possible fracture plane ($\sigma_n < 0, \sigma_{n1} = \sigma_{nt} = 0$), no failure will occur under the investigated fracture plane regardless of the load level. Therefore, no strength value is required for the normal stress under compression. The strength values for uniaxial tension ($\sigma_n > 0, \sigma_{n1} = \sigma_{nt} = 0$) and for pure longitudinal shear ($\sigma_{n1} \neq 0, \sigma_n = \sigma_{nt} = 0$) correspond to the well-known strength values $R_{\perp}^{t}$ (transversal tensile strength) and $R_{\parallel\perp}$ (longitudinal shear strength). However, it is not possible to determine the strength value for pure transverse shear loading $R_{\perp\perp}^{A}$ experimentally. The reason for that is that under pure transverse shear loading the tensile stress acting in a plane rotated by 45° is more critical than the shear stress. So the transverse tensile strength $R_{\perp}^{t}$ is measured instead of the transverse shear strength $R_{\perp\perp}^{A}$. As a remedy the transverse shear strength $R_{\perp\perp}^{A}$ can be estimated based on the transverse compressive strength $R_{\perp}^{c}$:

$$R_{\perp\perp}^{A} = \frac{R_{\perp}^{c}\,cos\left(\theta_f^{Y_c}\right)}{2p_{\perp\perp}^{c}} = \frac{R_{\perp}^{c}}{2\left(1 + p_{\perp\perp}^{c}\right)}, \tag{3-39}$$

where $\theta_f^{Y_c}$ is the fracture plane angle under uniaxial transverse compression. For carbon fiber-reinforced epoxy typically $\theta_f^{Y_c} = 53 \pm 3°$ is valid. In addition to the strength

values the Puck criterion requires four inclination parameters ($p^t_{\perp\perp}$, $p^c_{\perp\perp}$, $p^t_{\parallel\perp}$, $p^c_{\parallel\perp}$) describing the influence of inner friction. How to determine these parameters is described in [70]. Additionally typical values for carbon and glass fiber-reinforced epoxy are given.

The parabolic fracture condition of Puck for tensile loading ($\sigma_n(\theta) \geq 0$) reads

$$f_E(\theta) = \sqrt{\left[\left(\frac{1}{R^t_\perp} - \frac{p^t_{\psi\perp}}{R^A_{\psi\perp}}\right)\sigma_n(\theta)\right]^2 + \left(\frac{\tau_{nt}(\theta)}{R^A_{\perp\perp}}\right)^2 + \left(\frac{\tau_{n1}(\theta)}{R_{\parallel\perp}}\right)^2} + \frac{p^t_{\perp\psi}}{R^A_{\perp\psi}}\sigma_n(\theta), \quad (3\text{-}40)$$

and for compressive loading ($\sigma_n(\theta) < 0$)

$$f_E(\theta) = \sqrt{\left(\frac{p^c_{\psi\perp}}{R^A_{\psi\perp}}\sigma_n(\theta)\right)^2 + \left(\frac{\tau_{nt}(\theta)}{R^A_{\perp\perp}}\right)^2 + \left(\frac{\tau_{n1}(\theta)}{R_{\parallel\perp}}\right)^2} + \frac{p^c_{\psi\perp}}{R^A_{\psi\perp}}\sigma_n(\theta). \quad (3\text{-}41)$$

The relations $p^t_{\psi\perp}/R^A_{\psi\perp}$ and $p^t_{\psi\perp}/R^A_{\psi\perp}$respectively are established by a simple interpolation approach as follows:

$$\frac{p^{t,c}_{\psi\perp}}{R^A_{\psi\perp}} = \frac{p^{t,c}_{\perp\perp}}{R^A_{\perp\perp}}\cos^2(\psi) + \frac{p^{t,c}_{\parallel\perp}}{R_{\parallel\perp}}\sin^2(\psi), \qquad \text{where } \psi = \arctan\left(\frac{\tau_{n1}(\theta)}{\tau_{nt}(\theta)}\right). \quad (3\text{-}42)$$

In Fig. 3-27 the master fracture body of the Puck criterion is visualized. The master fracture body is open for pure compressive loading ($\sigma_n < 0, \sigma_{n1} = \sigma_{nt} = 0$). Thus no failure can occur under such an angle.

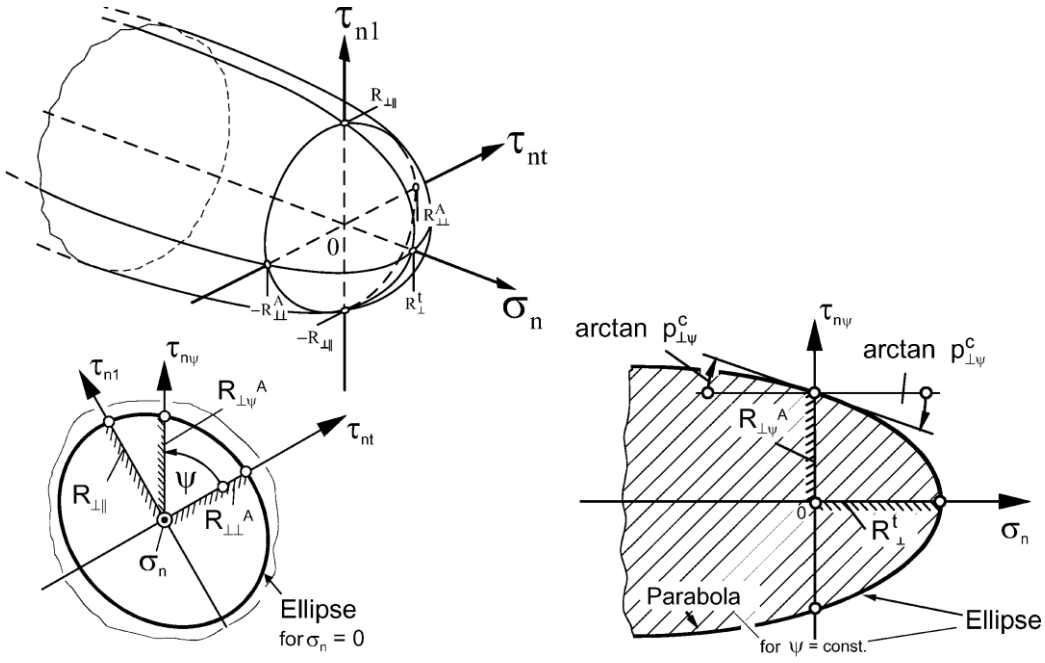

Fig. 3-27: Master Fracture Body in the ($\sigma_n, \sigma_{nt}, \sigma_{n1}$)-space [70]

In order to calculate the inter-fiber stress exposure according to Puck, the most critical fracture plane angle has to be found:

$$f_E = f_E(\theta_f) = \max(f_E(\theta)), \quad \text{where } \theta \in [-90°, 90°]. \tag{3-43}$$

When taking into account only plane stress states and assuming a coupling between parameters $p^c_{\perp\perp}/R^A_{\perp\perp} = p^c_{\parallel\perp}/R_{\parallel\perp}$, the Puck criterion does not require a search algorithm to determine the fracture plane angle. For transverse tensile loading $\sigma_2 \geq 0$ or a shear dominated load (σ_{12}) the fracture plane angle $\theta_f = 0°$. Only if a high transverse compressive stress is acting, the fracture plane angle θ_f is different from 0°. Considering the assumptions mentioned above, the compressive stress acting on the fracture plane σ_n at the point of failure always takes the value $\sigma_n = -R^A_{\perp\perp}$ (independent of the transverse stress σ_2 acting at the failure conditions). Therefore, the fracture plane angle θ_f can be calculated explicitly even for high transverse compressive loading. For plane stress states the Puck Criterion reads:

$$\text{Mode A: } f_E = \sqrt{\left[\left(\frac{1}{R^t_\perp} - \frac{p^t_{\parallel\perp}}{R_{\parallel\perp}}\right)\sigma_{22}\right]^2 + \left(\frac{\sigma_{12}}{R_{\parallel\perp}}\right)^2} + \frac{p^t_{\parallel\perp}}{R_{\parallel\perp}}\sigma_{22} \qquad \text{if } \sigma_{22} \geq 0, \tag{3-44}$$

$$\text{Mode B: } f_E = \sqrt{\left(\frac{p^c_{\parallel\perp}}{R_{\parallel\perp}}\sigma_{22}\right)^2 + \left(\frac{\sigma_{12}}{R_{\parallel\perp}}\right)^2} + \frac{p^c_{\parallel\perp}}{R_{\parallel\perp}}\sigma_{22} \quad \text{if } \sigma_{22} < 0 \text{ and } \left|\frac{\sigma_{22}}{\sigma_{12}}\right| \leq \left|\frac{R^A_{\perp\perp}}{\sigma_{12,c}}\right|, \tag{3-45}$$

$$\text{Mode C: } f_E = \left[\left(\frac{\tau_{21}}{2(1+p^c_{\perp\perp})R_{\perp\parallel}}\right)^2 + \left(\frac{\sigma^c_{22}}{R^c_\perp}\right)^2\right]\frac{R^c_\perp}{-\sigma^c_{22}} \text{ if } \sigma_2 < 0 \text{ and } \left|\frac{\sigma_{22}}{\sigma_{12}}\right| > \left|\frac{R^A_{\perp\perp}}{\sigma_{12,c}}\right|, \tag{3-46}$$

where $\sigma_{12,c} = R_{\parallel\perp}\sqrt{1+2p^c_{\perp\perp}}$. In case of Mode A and Mode B the fracture plane angle takes the value $\theta_f = 0°$. If the stress state satisfies the Mode C conditions, the fracture plane angle can be calculated as follows:

$$\cos(\theta_f) = \sqrt{\frac{R^A_{\perp\perp}}{-\sigma_{22}}}. \tag{3-47}$$

In Fig. 3-28 the inter-fiber failure condition according to Puck is shown in the σ_{12}-σ_{22} diagram. Additionally the simulated curves of off axis-compression tests, based on experimental results of [49] are given. In Section 3.6.3 the experimental setup and the corresponding simulation model is described.

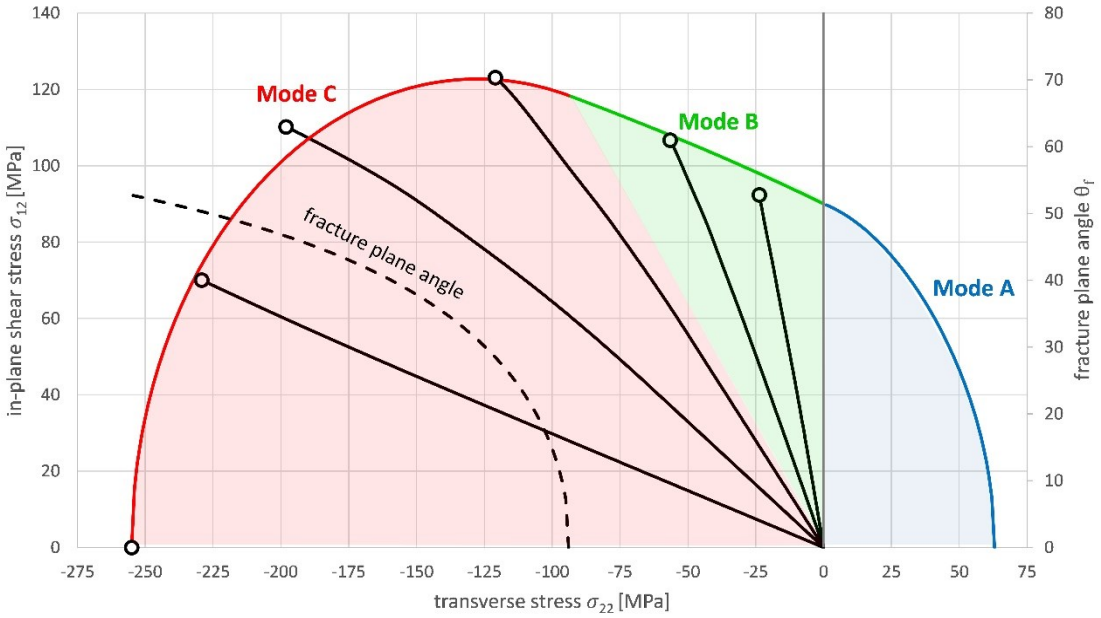

Fig. 3-28: Inter-fiber failure envelope of the Puck Criterion

3.4.2 Inter-Fiber Damage Initiation in Laminates

Usually inter-fiber failure criteria are not only used for single unidirectional fiber-reinforcement, but also to predict damage initiation in composite laminates existing of several plies with different fiber orientations. Crack development in an embedded or even an only one-sided tied up lamina, however, is influenced by the constraint effect of the adjacent plies. Due to being strain-controlled the material flaws in a thin lamina cannot grow freely up to micro-crack size in thickness direction, because the neighboring laminae will act as crack stoppers [69]. As a result the stress acting in an embedded laminate at the moment of the first formation of an inter-fiber crack depends on its ply thickness and the stiffness of the adjacent laminate, especially the adjacent plies. Some experimental studies addressing this effect can be found in literature.

Cross-ply laminates made of glass fiber (Tyglas Y119) reinforced polyester (Crystic 390) with various transverse ply thicknesses (0.75mm, 1.5mm and 2.6mm) have been tested in tension by Garrett [71].The onset of cracking was detected in three ways, visually, by acoustic emission and deduced from the “knee” in the stress-strain curves. A slight reduction of the initial cracking strain was observed with increasing transverse ply thickness (0.75mm → 0.48%, 3.2mm → 0.37%). A more significant dependency on the transverse ply thickness was established for the crack spacing. Generally, the higher the applied stress and the smaller the transverse ply thickness, the smaller was the averaged crack spacing.

Experimental results for carbon fiber reinforced epoxy T300/934 are given in [72–74]. Crossman [74] tested $(\pm 25/90_n)_S$, n=1,2,3 laminates under uniaxial tensile load. The single-ply thickness in a cured laminate was 0.132mm. Within this study transverse

cracks were detected by the use of x-ray pictures. The author observed a strong influence of the transverse ply thickness on the critical strain for transverse cracking. For a transverse ply thickness of 0.264mm (n=1) the critical strain was 0.697%, but free edge delamination occurred before transverse cracking. The specimens with a transverse ply thickness of 0.528mm (n=2) showed first cracks at an axial strain of 0.392%. In the specimens with 0.792mm (n=3) transverse ply thickness, the first inter-fiber cracks could even be observed at 0.33% axial strain. Similar tests have been conducted by Flaggs [72].In this study, the ultimate tensile load at which transverse cracking initiated in the 90° laminae of $(0_2/90_n)_S$, $(\pm 30/90_n)_S$ and $(\pm 60/90_n)_S$, n=1,2,4,8 laminates was determined experimentally using x-radiography. Based upon the lamination theory in-situ transverse strengths were calculated. These in-situ strengths, which were as high as 2.5 times the unidirectional transverse strength, were found to depend strongly on both the corresponding ply thickness and the orientation of adjacent plies.

An experimental investigation of the in situ ply shear strength was performed by Chang and Chen [75]. T300/1034-C carbon/epoxy cross-ply laminates were tested using a rail shear fixture. Similar to the results for transverse tension [72–74] an increase of the in situ shear strength was observed for the laminates with alternating plies (thin layers with uniform fiber orientation).

A further experimental study on initiation and growth of matrix cracks in cross-ply AS4/3502 carbon/epoxy laminates has been presented by Groves [76]. The thickness of the transverse plies is also varied between single ply clustering and eightfold ply clustering. Two different types of matrix cracks were identified, straight and curved cracks. The straight cracks are oriented normal to the laminate plane and grow very suddenly, and probably emanate from preexisting microscopic flaw. The curved cracks formed after the straight cracks and followed a repeatable pattern of location and orientation relative to the straight cracks. As a consequence, it was postulated that the growth mechanism of the curved cracks is driven by the stress state resulting from the formation of the straight cracks. The experiments showed a correlation between the number of curved cracks and the relative thickness of the 0° and the 90° layers as well as the total thickness of the 90° layers. With an increasing thickness of the transverse plies the number of curved cracks increased as well. For a single 90° ply embedded between 0° plies no curved cracks were observed. However, the total number of cracks for all laminates was fairly constant.

Boniface [77] found out that transverse ply cracking is a two stage process of initiation and propagation. In laminates with thick plies, all cracks span the full thickness and width of the transverse ply whereas for laminates with thin plies, same part width cracks exist over an appreciable strain range. At large ply thicknesses, first cracking is initiation-controlled while at small ply thicknesses it is propagation controlled. So the measurement of in situ strengths depends strongly on the definition of the minimum crack length, where a crack is counted. The investigated laminates were fabricated from Tenax HTA carbon fibers and F922/F927 epoxy resin.

Another study of the in situ transverse tensile strength of composite plies is presented by Sebaey et al. [78]. The crack density of $(\pm 45/90_n)_S$, n=1,2,4 laminates was measured optically at the free edge. While only a slight decrease of the axial strain at damage initiation for increasing transverse ply thickness was observed (0.44% for n=1 and 0.41% for n=4), a strong in situ effect (influence of the ply thickness) on the transverse strength is described. Responsible for the differences of the calculated in situ strengths are different thermal residual stresses, caused by a change of the ratio between the number of $\pm 45°$ and 90° plies.

A theory explaining the dependency of the ply thickness on the transverse crack initiation stress (in-situ strength) has been developed by Dvorak [79]. According to this theory, crack propagation in fiber direction controls the strength of thin plies, while cracking in the thickness defines the strength of thick plies. The model can predict the strength in a laminate as function of the ply thickness and applied stress state. The experimental values of the ply toughness and the ratio between the toughness of a crack growing in fiber direction or in thickness direction is required. The theoretical results have been compared to experimental results for T300/934 carbon epoxy [74] and to E-Glass/epoxy showing good correlation.

Properly the best known publication about the estimation of in situ strengths has been presented by Camanho et al. [80]. The calculation of the in situ transverse tensile strength is taken from Dvorak [79], but the calculation procedure for the in situ in-plane shear strength has been improved, considering nonlinear material behavior. Three ply configurations are considered for the determination of in situ strengths: thick plies, thin plies, and thin outer plies. For the transition thickness between thick plies and thin plies Dvorak [79] names a value of 0.5mm. For each case closed-form equations are given to calculate the in situ transverse tensile strength and the in situ shear strength respectively. A detailed description and derivation of the formulas can be found in [80] and [30].

Catalanotti [81] proposed a three-dimensional failure criteria for composites accounting for in situ strengths. Also a calculation procedure for an in situ transverse compression strength depending on the in situ shear strength is given. When using in-situ strengths, required relations between the material properties are not always satisfied. This results in both wrong first ply failure loads and wrong fracture plane angles. To remove such limitation, additional constants depending on the in situ strength relations are introduced.

Inter-Fiber Damage Initiation Criterion

For the layer wise detection of inter-fiber damage initiation in laminates the Puck Criterion is suitable in principle. However, the constraint effect of the surrounding plies must be considered. Therefore, in-situ strength values depending on the ply thickness need to be determined. The in-situ transverse tensile strength has been determined by analyzing micrographs of different loaded cross-ply laminates. The in-situ shear stress has been estimated based on $\pm 45°$ tension tests with single and double ply-clustering, see Section 3.4.3. The inter-fiber damage initiation criterion for combined in-plane shear

and transverse tensile load results from inserting in-situ strengths instead of the basic strengths into the Mode A of the Puck Criterion:

$$f_E = \sqrt{\left[\left(\frac{1}{\widetilde{R}_{\perp}^{t}} - \frac{p_{\parallel\perp}^{t}}{\widetilde{R}_{\parallel\perp}}\right)\sigma_{22}\right]^2 + \left(\frac{\sigma_{12}}{\widetilde{R}_{\parallel\perp}}\right)^2} + \frac{p_{\parallel\perp}^{t}}{\widetilde{R}_{\parallel\perp}}\sigma_{22} \qquad \text{if } \sigma_{22} \geq 0. \tag{3-48}$$

For pure transversal compressive loads, damage is not active in the present model. For a unidirectional specimen fracture appears on a plane with an angle of about 54°. In a laminate, this failure mechanism would induce an inter-ply delamination between plies of differing fiber orientation. Remarkably, within the experimental study, such a failure mode has not been found. Prepared micrographs of $\pm 45°$ specimens exhibit only vertical cracks, see Fig. 3-29. Based on these observations, the proposed damage initiation criterion exclusively detects shear failure. Therefore, only Mode B of the Puck Criterion is used to detect inter-fiber damage initiation under combined in-plane shear and transverse compressive load:

$$f_E = \sqrt{\left(\frac{p_{\parallel\perp}^{c}}{\widetilde{R}_{\parallel\perp}}\sigma_{22}\right)^2 + \left(\frac{\sigma_{12}}{\widetilde{R}_{\parallel\perp}}\right)^2} + \frac{p_{\parallel\perp}^{c}}{\widetilde{R}_{\parallel\perp}}\sigma_{22} \qquad \text{if } \sigma_{22} < 0. \tag{3-49}$$

Fig. 3-29: Micrograph of the damage state shortly before ultimate failure of a ±45° laminate

The damage initiation criterion for single and double clustered plies is shown in Fig. 3-30, together with the effective shear and normal stress output of the angle-ply tension tests. Additionally, the ultimate strength of the angle-ply laminates are marked taken into account the ply clustering. The tests are described in Section 3.6.4 and the in-situ strength values are given in Table 3-1. For $\pm 50°$, $\pm 60°$ and $\pm 75°$ angle-ply laminates, the curves intersect the damage initiation criterion shortly before ultimate failure.

Noticeable is the extremely nonlinear evolution of the ratio of the stress components for $\pm 45°$ caused by concurrent effects of plasticity and fiber rotation. For this kind of angle-ply laminates damage onset occurs due to an interaction of shear and transverse tension stresses. Subsequently, the normal stress changes to the compressive region and continues in damage-inducing states up to large compression stress. A consideration of damage is therefore essential for these laminates.

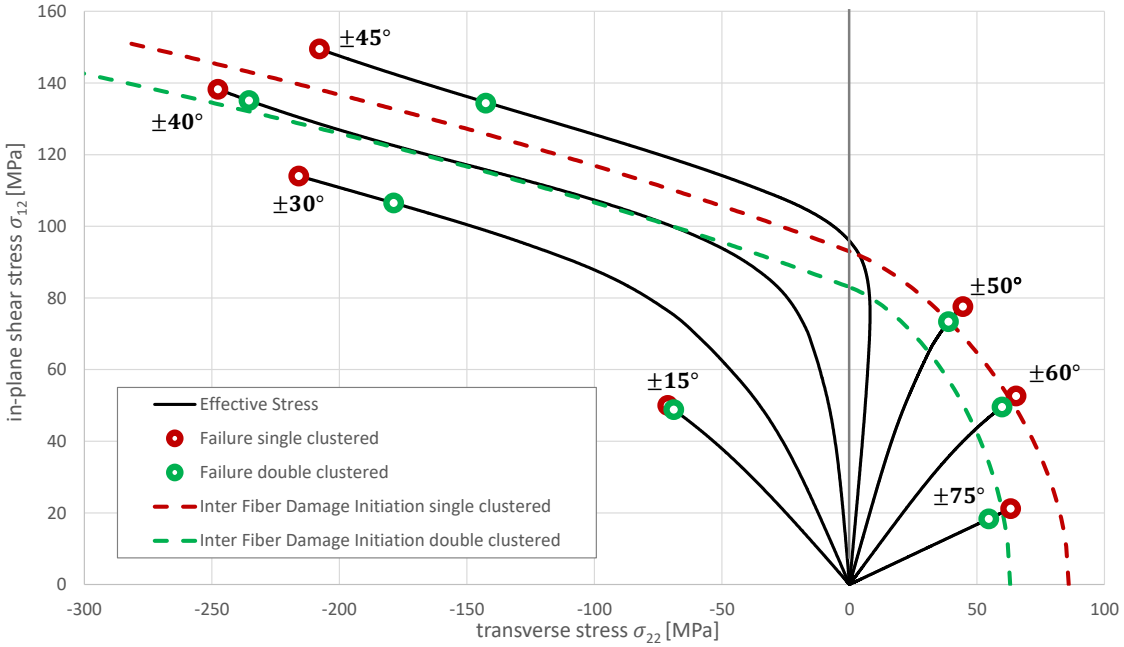

Fig. 3-30: Damage initiation criterion and the effective shear and normal stress response of angle-ply tension specimens for IM7-8552

3.4.3 Inter-Fiber Damage Evolution in Laminates

The objective of the degradation analysis is to reduce the effective stress $\boldsymbol{\sigma}^{eff}$, calculated by the plasticity model, to determine the stress averaged over the ply including damaged regions. Therefore, two scalar damage variables are introduced. The affected stresses are directly degraded through multiplication with the relating variables. The relation between the undamaged effective stresses and the smeared nominal stresses is given by

$$\sigma_{22} = (1 - d_2)\sigma_{22}^{eff}, \tag{3-50}$$

$$\sigma_{12} = (1 - d_{12})\sigma_{12}^{eff}. \tag{3-51}$$

The damage variables are calculated by a simple approach, where the difference of the current strain to the strain at damage initiation is multiplied by a constant. For transverse tension and in-plane shear different constants are necessary. If a transverse compressive stress is acting, the damage variable d_2 is set to zero, as compression can be transmitted by the crack. The damage variable d_2 reads

$$d_2 = \begin{cases} k_2 \left(\varepsilon_{22} - \varepsilon_{22} \left(\frac{\boldsymbol{\sigma}}{f_E} \right) \right) & \text{if } \sigma_{22} > 0 \\ 0 & \text{if } \sigma_{22} \leq 0 \end{cases} \tag{3-52}$$

and the damage variable for in-plane shear is defined as

$$d_{12} = k_{12} \left(\varepsilon_{12} - \varepsilon_{12} \left(\frac{\boldsymbol{\sigma}}{f_E} \right) \right). \tag{3-53}$$

When calculating the damage variables, some limitations have to be taken into account. Firstly Eq. (3-52) and Eq. (3-53) are only valid if inter-fiber damage is detected ($f_E > 1$). Further the damage variables must not become greater than one. If a resulting damage variable is greater than one, the corresponding damage variable is set to one to avoid a negative stiffness. To prevent material healing the damage variables are only updated when they increase. During unloading the material model exhibits linear elastic behavior without additional damage and yielding. For subsequent reloading the stress-strain response is consistent with the unloading curve until the yield surface or damage initiation is reached. Thus, energy creation is avoided. The real unloading behavior of composites is much more complex as discussed in Section 3.5.

Determination of the damage progression parameters

The damage progression parameter for in-plane shear k_{12} has been determined based on the experimental results of $\pm 45°$ laminates. The k_{12} and the in-situ strength values $\tilde{R}_{\parallel\perp}$ were varied to find an optimal parameter set leading to the best correlation between the simulated and experimental measured axial response curves for both single and double ply clustered specimens. In Fig. 3-31 the axial stress-strain response of the single and double clustered $\pm 45°$ laminates is shown together with the evolution of the in-plane shear damage variable d_{12}. The transverse damage variable d_2 has only very little effect on the axial response of these tests, as the transverse stress component σ_{22} reaches only little tension at the beginning of the test and then turns to compressive values, see Fig. 3-30. The correlation between simulation and experimental results are shown in Fig. 3-45. The greatest benefit of the proposed inter-fiber damage model is its simplicity. A drawback is that it is sensitive to the parameters, making it necessary that all involving parameters are determined interactively.

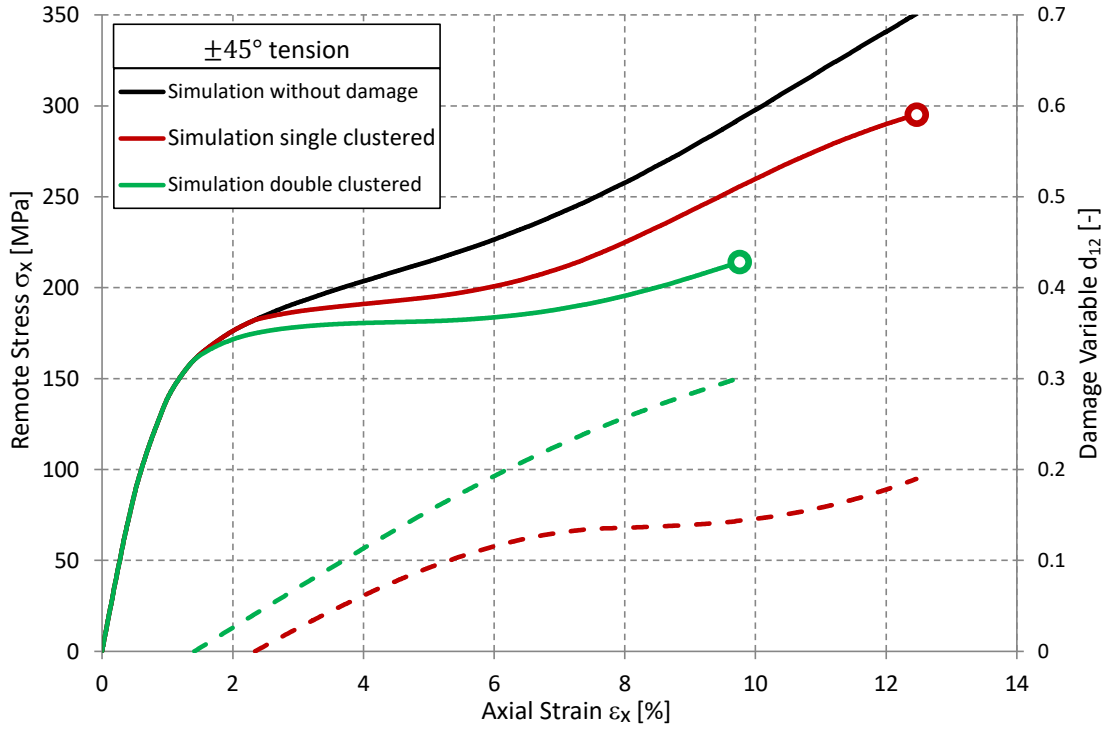

Fig. 3-31: Axial response and evolution of inter-fiber damage of ±45 laminates under tension

The damage progression parameter for transverse tension k_2 has been determined based on the experimental results of the $0/90°$ cross-ply laminates. As the effect of the inter-fiber damage in the $90°$ plies on the axial response is very slight due to the dominance of the $0°$ plies, inter-fiber cracks have been counted at different load stages. For that purpose, polished micrographs have been prepared. The specimen with a length of 250mm, a width of 25mm and a thickness of 2mm have been fabricated as described in Section 3.6.2. After loading the specimens to their specific load level, little samples have been cut out of the specimens to prepare for micrographs. Attention was paid to making sure that the observed sectional view is orientated length to the specimen and in the middle of the specimen for both length and width. Thus, the counted crack densities are not influenced by edge effects. It is important for the quality of the polished micrographs that the fibers are cut at an angle. Therefore, the samples have been embedded under an angle into the support resin before polishing.

The counted crack densities of the $90°$ plies referred to the axial strain are given in Fig. 3-32. The evolution of the crack densities can be approximated by straight lines for both, single (0.125mm ply thickness) and double clustered (0.25mm ply thickness) specimens. The ply thickness influences crack initiation as well as the increase of the crack density. But it can be assumed that the crack accumulation rate for the single clustered plies is approximately half as big as for the double clustered plies. To estimate the relation between the crack density and the damage variable, a discrete crack analyses with representative volume elements (RVE) can be performed, as shown in [82]. This paper shows the results of a numerical RVE study investigating the effect of nonlinear material

behavior on the relation between a discrete crack density and the smeared damage variable. For the occurring crack densities an interaction between neighboring cracks can be neglected. In other words this means that the smeared damage state remains the same when the ply thickness is doubled and the crack density is halved simultaneously. Therefore, the damage variable d_2 can be assumed proportionally to the crack density δ_{Crack}:

$$d_2 = 1.05\ \delta_{Crack}\ t_{Ply}. \tag{3-54}$$

The increase rate of the crack density can be converted to the damage progression parameter k_2 by application of Eq. (3-54).

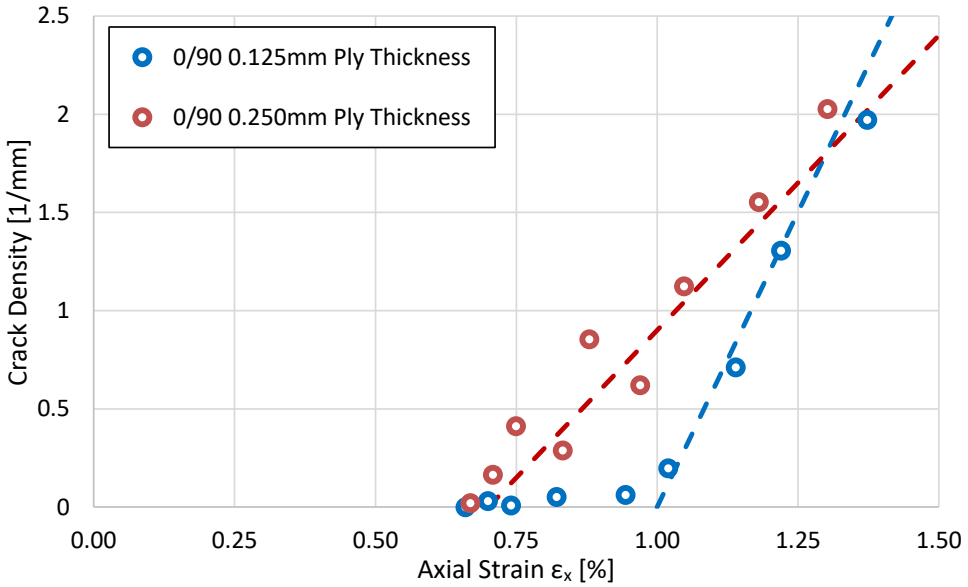

Fig. 3-32: Crack evolution in cross-ply laminates

3.5 Unloading behavior

During unloading the proposed material model exhibits linear elastic behavior without additional damage and yielding. For subsequent reloading the stress–strain response is consistent with the unloading curve until the yield surface or damage initiation is reached. Thus, energy creation is avoided and the material behavior takes care of physical principles. However, the unloading behavior of carbon fiber reinforced composites is much more complex, as the nonlinear material behavior is strongly dependent on time and temperature [83–86]. During unloading also the plastic strain decreases dependent on the unloading velocity. The strain retardation process after fully unloading a single ply clustered ±45° laminate, loaded to 8.09% axial strain is shown in Fig. 3-33. After reaching the unloaded condition ($F_x = 0$), the axial strain in the specimen decreases over time. The strain retardation rate is reduced with time and the response

indicates that an amount of a residual deformation is reached after a slow reconstitution of the internal mechanical equilibrium.

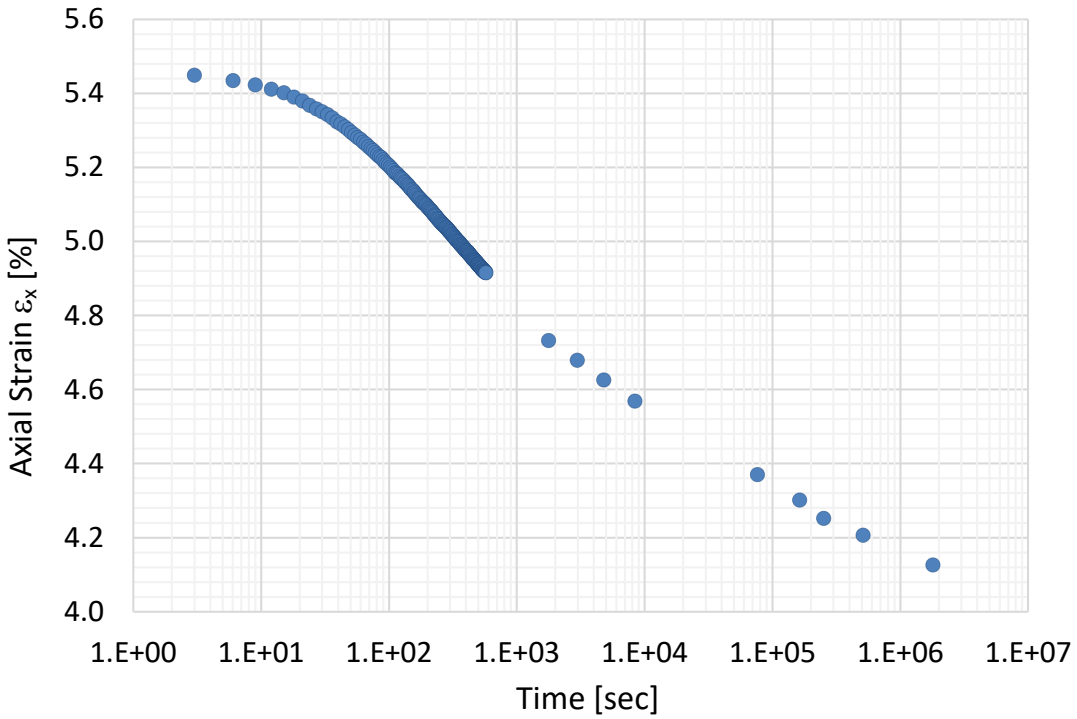

Fig. 3-33: Strain retardation process for a ±45° laminate after unloading [87]

Nonlinear material behavior results from a combination of plastic strain accumulation and stiffness reduction due to damage. For an experimental determination of the amount of nonlinearity caused by plastic strain accumulation and damage respectively, Ladevèze [11] proposed to use cyclic tests, where the specimen is unloaded and reloaded at several load stages bevor ultimate failure is reached.

The polymer material‘s inherent time dependency of mechanical behavior has a significant impact on the slope of the reloading cycle due to viscous micromechanical processes in the polymer chains. To determine a variation of the stiffness from the stress–strain response, several procedures are compared in Pettersson et al. [88]. The tangent modulus, which is the initial slope of the loading cycle, and the secant modulus, which is the slope between the reversal point of unloading and reloading, can be evaluated. In Fig. 3-34 the stress–strain response of two different single ply clustered ±45° specimens is shown. The analysis of the secant modulus results in a significantly higher reduction of the stiffness. Additionally, there is a difference between the evaluations of the stiffness with retardation time $\tilde{E}_{xd}^{sec}$ and without E_{xd}^{sec}. As both specimens were previously loaded to the same maximum stress and strain, the difference in moduli indicates an additional damage evolution during the retardation time. This contradicts the physical behavior during retardation. Fiber reinforced composites accumulate additional plastic strains during unloading [89]. This impedes a

determination of the damage state concerning a specific load using the secant modulus measurement. A tangent modulus of the envelope without retardation is not possible to evaluate, as no distinct linear response is exhibited.

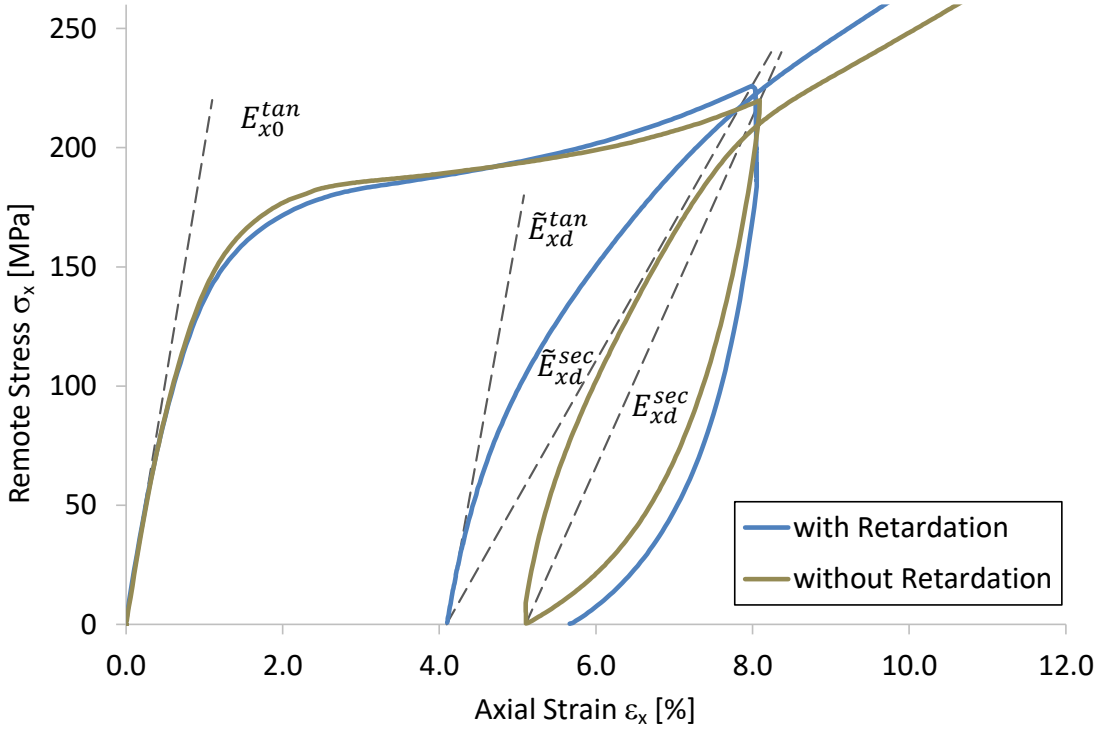

Fig. 3-34: Comparison of different laminate stiffness evaluation procedures [87]

The time and temperature dependency of the material properties are not only relevant for unloading or long term behavior. Also experiments under extreme strain rates show significantly stiffer response curves compared to the results under quasi-static conditions [49, 60]. In order to enable reliable results during unloading it is absolutely necessary to care for the time-dependency of the mechanical behavior. The experimental characterization of a universally valid material model requires great effort. It is therefore usually recommended to use model restricted to its application with the benefit of much lower characterization effort. The applicability of the presented laminate hardening model is limited to steadily loading under quasi-static conditions and room temperature.

3.6 Validation and Model Verification

The laminate hardening model is subjected to a comprehensive validation to verify its capabilities and prediction accuracy. To this end a test series of angle-ply laminates with seven different off-axis angles has been conducted. Also two different layups have been tested for each off-axis angle in order to investigate the influence of the ply thickness. On the one hand the plies were stacked alternating. On the other hand in each case two

plies of the same orientation were clustered together. Due to a wide specimen geometry, large axial strains could be obtained and thereon the verification of the model's applicability up to large deformations was possible. Additionally, the constitutive model is validated with off-axis compression tests from literature [49]. Using the same material system offers the determination of a single material parameter set for the simulation of both test series. This improves the significance of the verification and therefore allows a better prediction of the structural applicability.

3.6.1 Material Parameters

One of the most important objectives during the development of the presented material model was to get along with as little as possible parameters. To achieve this, a mechanism based approach was followed instead of a mathematical one. Considering the scope and the forecast accuracy of the model, only a few material parameters are required. In Table 3-1 the material parameters for the material system IM7-8552 and Scotchply SP-319 are given. To describe the initial linear elastic behavior of a unidirectional reinforced ply transversal isotropic material behavior can be assumed. Therefore, five constants ($E_1^0, E_2, \nu_{12}, G_{12}$ and G_{23}) are required. The laminate hardening model considers four different mechanisms: Deformation induced fiber reorientation, non-hookean elasticity in fiber direction, partly interactive plasticity and inter-fiber damage. Having regard to deformation induced fiber rotation does not require any parameter, as current fiber orientation can be directly calculated from the deformation state. The non-hookean elasticity in fiber direction requires one material parameter k_f. The partly interactive plasticity model is more extensive. But its mechanism based formulation allows a three dimensional formulation without additional parameters in comparison to the plane stress formulation. Only two master curves describing plastic yielding under transverse and longitudinal shear loading are required. Unfortunately, the determination of the master curves is complex, as hydrostatic sensitivity influences yielding and large longitudinal shear deformations are achievable. However, only two experiments are necessary for the deviation of both master curves, see Section 3.3.4. The parameters most difficult to establish are the hydrostatic sensitivity parameters. Therefore, experiments under high hydrostatic pressure are essential, see Section 3.3.5. But for in-plane loading conditions this parameters are not very sensitive so existing values for similar material systems should be suitable. The last mechanism implemented in the laminate hardening model is inter-fiber damage. Here again the constitutive model is formulated in way to minimize the number of required material specific parameters. In total the inter-fiber damage model needs four parameters. Two of them are strength values and the other two control the stiffness degradation for transverse and longitudinal shear loading respectively. It is however to be considered, that the strength values depend on the laminate layup, especially the thickness of the corresponding ply. For the simulations different values for single and double clustered plies are used. Within the experimental study no angled inter-fiber cracks were observed, therefore, the transverse

compressive strength is not required, as discussed in Section 3.4.2. As the strength values in combination with the damage progression parameters describe the damage behavior in the laminate, it is important to calibrate them on the same experimental bases as shown in Section 3.4.3.

The material properties of carbon fiber-reinforced epoxy, especially for transverse and shear behavior, depend on the applied manufacturing process, even for prepreg material systems. The degree of cure of the epoxy resin is sensitive to the temperature and pressure profile during the curing process. Depending on the geometry and tooling this can vary locally. In literature for one prepreg system different properties are given by different research institutions. Especially inter-fiber damage is very sensitive to curing conditions. For the fabricated laminate plates, a slight tendency for the specimens taken from the edge to reach a little bit lower ultimate strength could be observed. For complex parts this effect may become much more important. The consideration of effects of manufacturing by process simulations should be perused as a long-term objective.

Table 3-1: Material parameters for the laminate hardening model

Description	Symbol [Unit]	Hexcel IM7-8552		Scotchply SP-319
Longitudinal Modulus	E_1^0 [GPa]	163		162*
Transverse Modulus	E_2 [GPa]	9.08		6.6*
Longitudinal Poisson‘s Ratio	ν_{12} [-]	0.32		0.32
Longitudinal Shear Modulus	G_{12} [GPa]	5.18		3.3*
Transverse Shear Modulus	G_{23} [GPa]	3.97**		2.9
Non-Hookean Parameter	k_f [-]	21		21
Neat Resin Modulus	E_M [GPa]	4.08***		3
Hydrostatic Sensitivity	α_{tr} [-]	0.42		0.42
	β_{tr} [-]	0		0
	α_{sl} [-]	0.25		0.25
In-Situ Transverse Tensile Strength	$\widetilde{R}_\perp^t$ [MPa]	Single 86	Double 63	-
In-Situ Longitudinal Shear Strength	$\widetilde{R}_{\parallel\perp}$ [MPa]	Single 93	Double 83	-
Damage Progression	k_2 [-]	2.4		-
	k_{12} [-]	70		-

* [64] ** [90] *** [91]

3.6.2 Specimen Preparation

The prepreg material Hexply IM7-8552 used for the experimental validation is available on a role. The first stage in manufacture of composite specimens is the precise cutting of the individual layers. Any deviation from the nominal orientation angle occurring during this process cannot be corrected later on. So this step is very important to allow for a high quality of the specimens. The application of a CNC-Cutter enabled very accurate cut-offs without recognizable angular deviation, see Fig. 3-35.

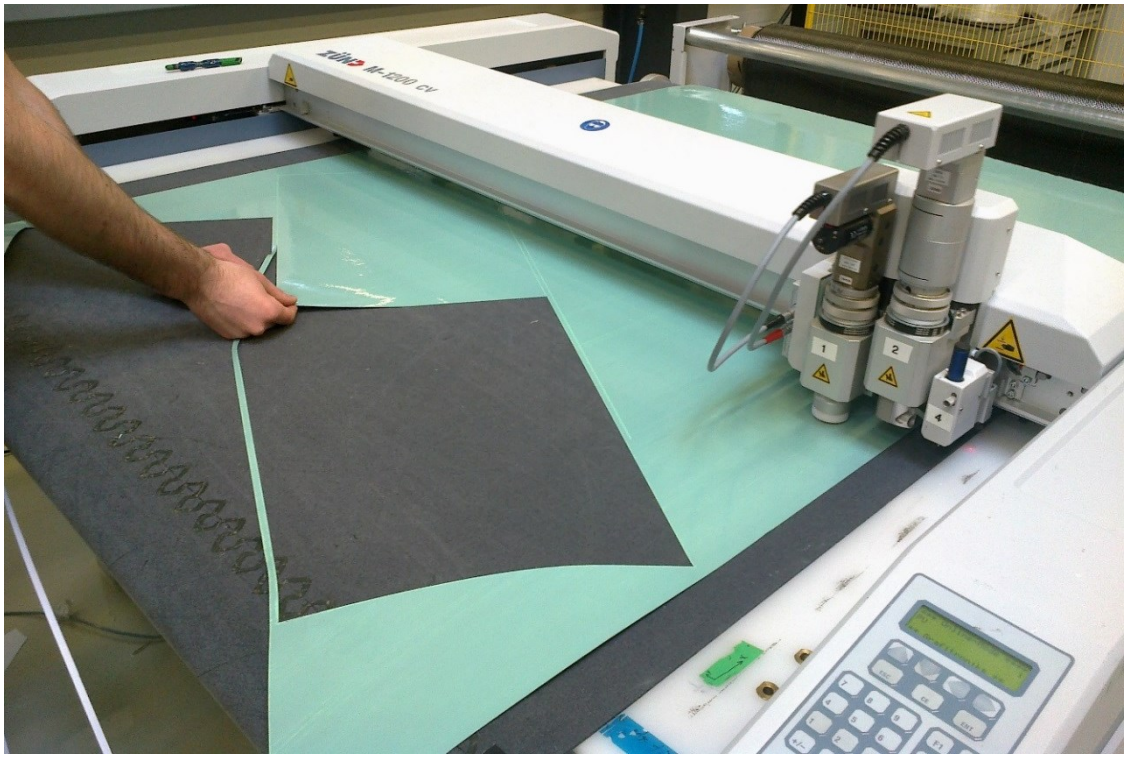

Fig. 3-35: Cutting of the individual layers using a CNC-Cutter

In the next step the individual layers have to be stacked on top of each other. This handcrafted step is also very important for the quality of the specimens. On the one hand the individual layers have to be stacked without angular misalignment and on the other hand air inclusions between the layers should be avoided. Making it difficult is that once the layers tough each other, it is impossible to separate them without grater damage. In preliminary tryouts it has been tested how the best quality could be achieved. For best results two persons were necessary to stack the layers manual. The first ply was fixed on a vacuum table, protected against sliding. Than the next ply was deposited beginning with the smaller side. One person lifted up the open end of the ply to avoid any contact with the previously dropped ply. During the deposition process, the other person slowly spread out the air between the layers from center toward the outside edges. Thus, noticeable air inclusions could be avoided and a precise alignment could be ensured. With a plate length of 560mm the misalignment error was in a range from 1mm to 2mm.

This correlates to an angular tolerance of round about 0.2°. After finishing the stacking a Teflon film was applied on both sides. It has become evident that little air bubbles between the stack and the film result in little surface damage of the finished plates. By carful stretching out the air bubbles this could be avoided.

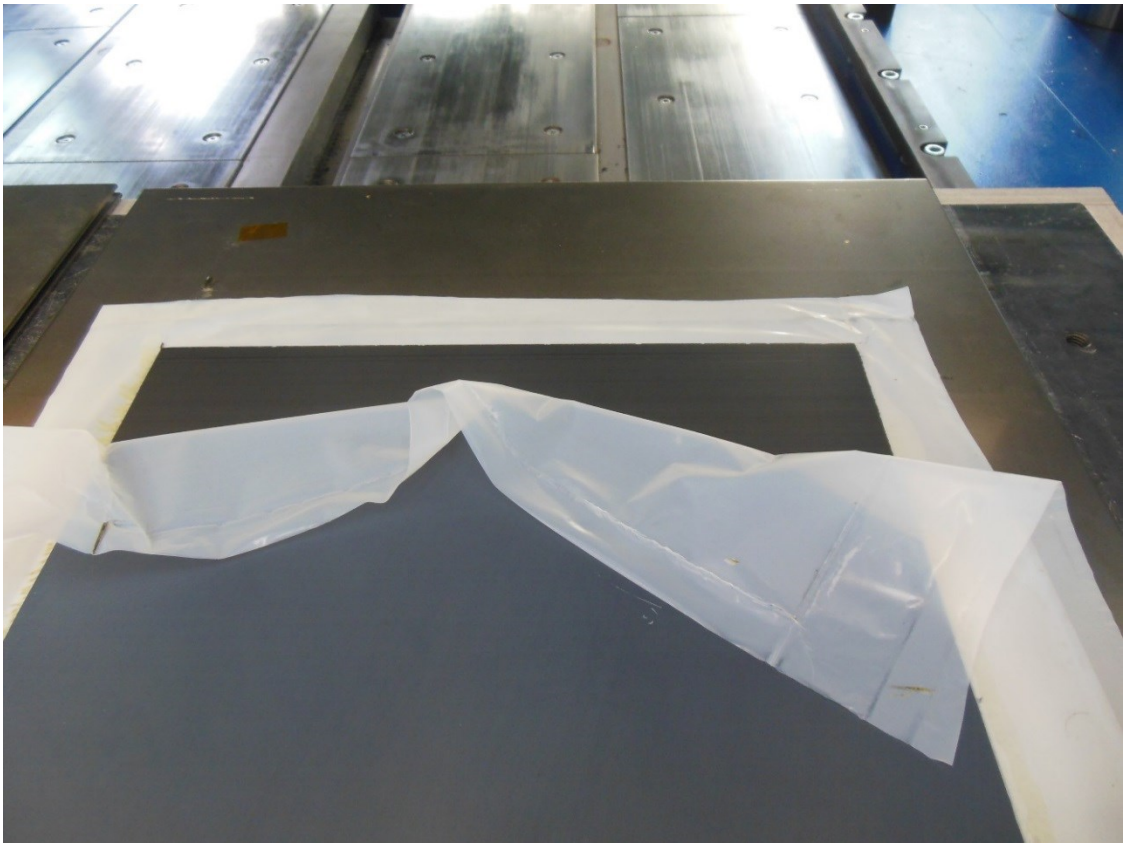

Fig. 3-36: Finished laminate plate between Teflon film

Subsequently the plates have been cured in a Rucks hot press. Therefore, the laminate stacks have been placed between 3mm thick steel plates. In order to impede a sideward leakage of resin during curing, steel spacers have been put directly on the stack. At each time two plates could be cured side by side without an influence on the quality of the finished plates. All manufactured plates exist of 16 individual layers and have a total thickness of $2 \pm 0.01\text{mm}$. Prepreg material has to be stored in a deep-frozen and should only be handled at room temperature for a certain time. To enable a homogeneous quality for all specimens, all laminated plates have been fabricated in a short period. Thus, the plates could be stored already cured until further processing.

To ensure a sparing load transmission, glass fiber-reinforced end-taps with 1mm thickness were assembled to all specimens, according to ASTM D 3039 [92]. The adhesive *UHU Endfest 300* was used to bond the taps on the partly grounded and cleaned laminate plates. In the second last step, the specimens were cut out the laminate plates using a water cooled diamond saw. Finally, the front surface of the specimens was

prepared for the strain-field measurement by digital image correlation (DIC). Therefore, a black-on-white speckle pattern was generated by air-brush.

Fig. 3-37: Curing the laminated plates in a Rucks hot press

3.6.3 Unidirectional Off-Axis Compression

In this section experimental results of unidirectional off-axis compression tests from literature [49] are presented for validation of the laminate hardening model. In this study the carbon-epoxy prepreg system Hexply IM7-8552 was used. In a SATIM hot press 32-ply plates were manufactured in accordance to the curing cycle. From these 4.0mm thick panels, off-axis compression specimens with fiber orientation angles $\theta = 15°, 30°, 45°, 60°, 75°, 90°$ were cut on a water-cooled diamond saw. All specimens had the same nominal dimensions of $20 \times 10 \times 4\text{mm}^3$ and were in accordance with the end-loading compression test standard ASTM D 695 [62]. For each off-axis angle, three specimens were tested. For the 15° specimen type, more tests were performed, since two failure modes were observed in this case. From a total of 12 specimens, 9 failed in kink-band mode at either top or bottom end-surface and only 3 failed in the expected in-plane shear dominated mode. The in-plane strain field was obtained from the digital image correlation software *ARAMIS*. For the stress-strain curves presented here, a virtual gauge area of $3 \times 3\text{mm}^2$ was chosen.

For the 15° and the 30° specimens, a stick-slip behavior at the beginning of the test was identified. This indicates that the friction between the specimen end-surfaces and the

tungsten-carbide inserts of the loading fixture was not negligible, even though a thin layer of molybdenum-disulfide (MoS2) was used to minimize the friction behavior.

To account for this effect in the numerical model, the specimen is discretized using C3D8I solid elements and the loading-plates are included as rigid-body elements. The contact between the loading-plates and the specimen end-surfaces accounts for friction. A reasonable value for the friction coefficient was found in the literature for room temperature conditions as 0.055 [93]. According to the experimental procedure, the axial strain in the numerical modal is determined as the average strain of an $3 \times 3\text{mm}^2$ area in the middle of the specimen.

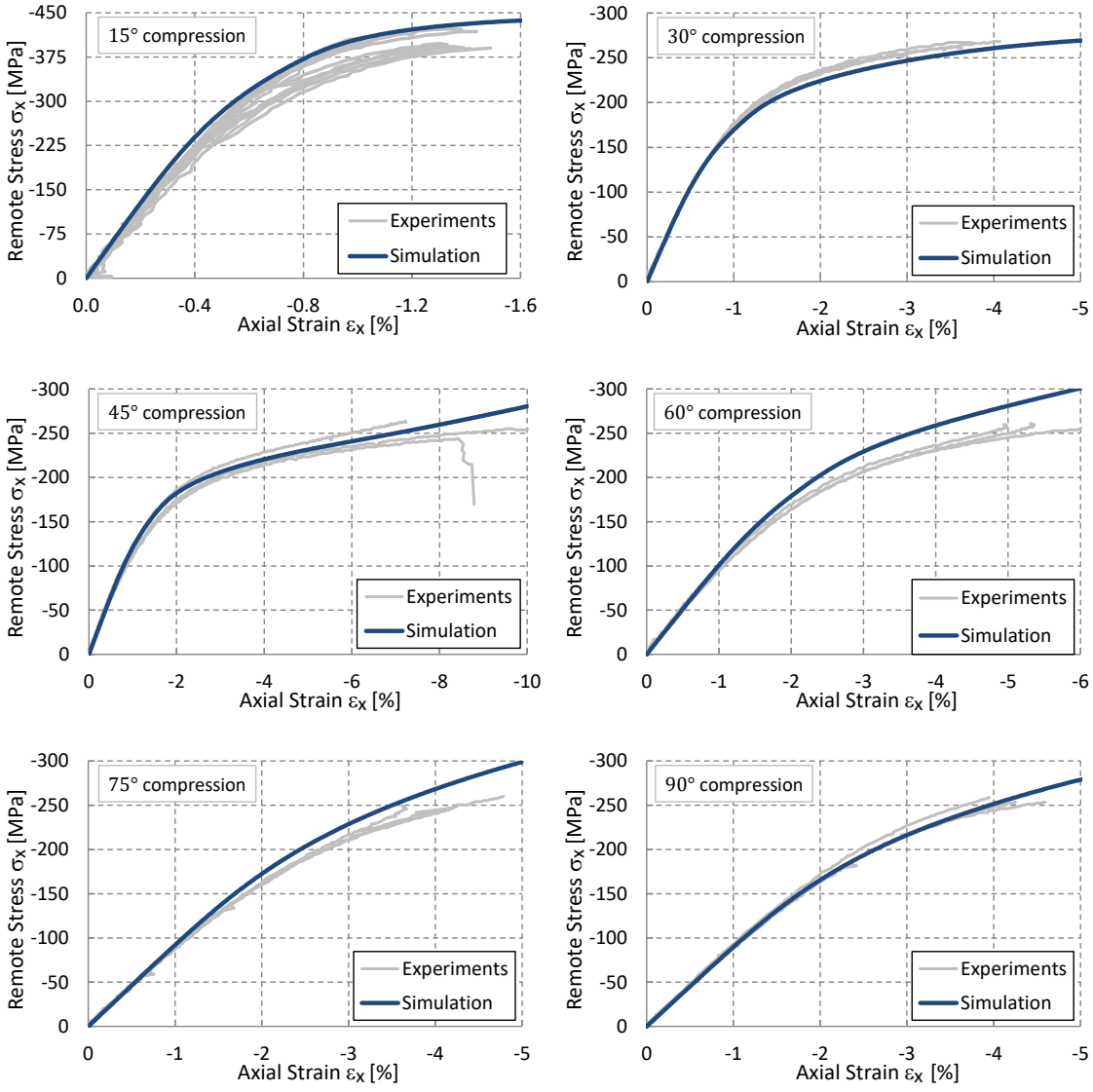

Fig. 3-38: Remote axial stress-strain response of unidirectional off-axis compression specimens for IM7-8552, experimental data from [49]

As shown in Fig. 3-38, the predicted results correlate well with the experimentally measured. The results of the 90° transverse compression test are used as model input

and therefore cannot be used as model validation. For reasons of completeness the simulated curve and the experimental results are shown nevertheless. For the simulations of the off-axis compression tests the inter-fiber damage model, described in Section 3.4 was not used, as here the nonlinear material model is focused. So the simulated response curves do not end at the point of failure. The failure behavior of the off-axis compression specimens is addressed in Section 3.4.1.

3.6.4 Angle-Ply Tension

In the previous section it has been shown that the proposed hardening model is able to simulate the response curves of unidirectional off-axis compression tests with high accuracy. However, that is not enough to ensure that the model provides accurate and useful results for arbitrary loading conditions. As shown in [49] and [52], fundamentally different plasticity approaches are able to match the same series of unidirectional off-axis compression tests. For other stress states, for example a combination of in-plane shear and transverse tension, the model predictions differ considerably from each other. To allow for an extended bases for validation, angle-ply tension tests with the off-axis angles $\theta = 15°, 30°, 40°, 45°, 50°, 60°, 75°$ have been conducted. Also two different layups have been tested for each off-axis angle in order to investigate the influence of the ply thickness. On the one hand the plies were stacked alternating. On the other hand in each case two plies of the same orientation were clustered together. A big advantage of the angle-ply tension specimens in comparison to the off-axis compression specimens is a homogeneous stress state over a large area of the specimens. In Fig. 3-39 the optically measured axial strain distribution of a $45°$ off-axis compression specimen and of a $\pm 45°$ angle-ply tension specimen is shown. While the strain varies extensively in the unidirectional specimen caused by local conditions, the strain in the angle-ply laminate is very homogeneous across the whole specimen expect for the load introduction areas outside the measuring range.

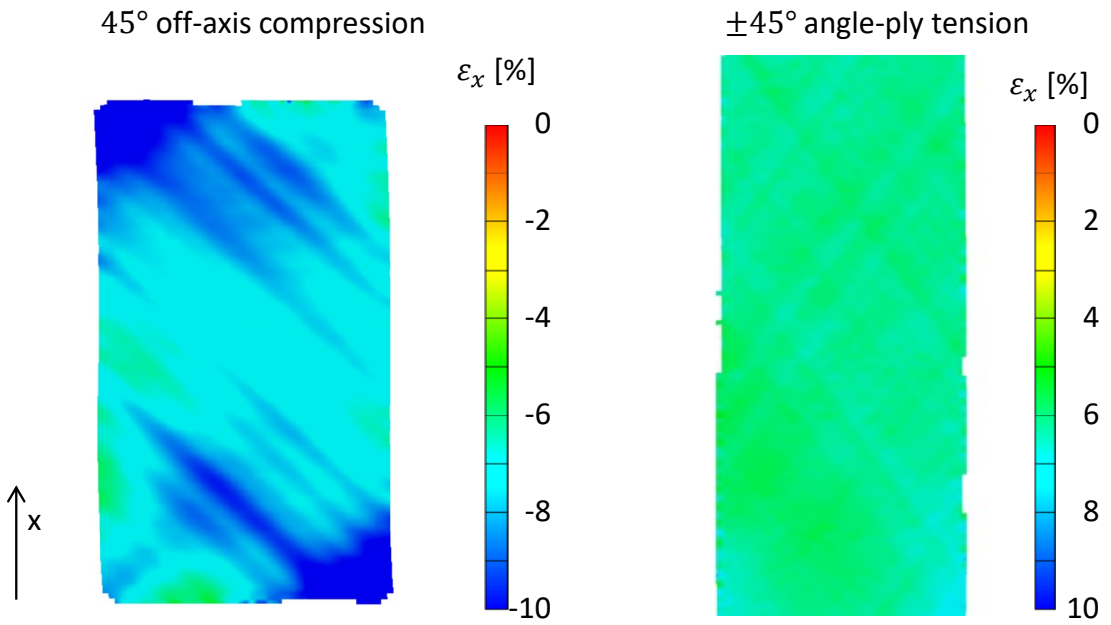

Fig. 3-39: Optical measured axial strain fields of a 45° off-axis compression and a ±45° angle-ply tension specimen

Another advantage of the angle-ply tests is the avoidance of structural instability modes. Moreover, angle-ply laminates are subjected to a highly non-proportional interaction of the local stress components that do not occur in unidirectional off-axis tests. All tested specimens consist of 16 plies. To account for the influence of the single ply thickness, two different layups have been investigated. For the layup named single ply clustered the individual plies are stacked alternating, while for the layup named double ply clustered at each case two plies with the same orientation are stacked together. When defining the exact layup several features need to be considered. In order to prevent an extension-bending coupling the layup of all laminate plates has been defined symmetric to mid-plane. In addition to impede an extension-shear coupling all layups are defined balanced (same number of $+\theta$ an $-\theta$ plies). To satisfy both requirements, it is not possible to keep a pure single-ply and double-ply clustering, respectively. As remedy the single clustered specimens have a doubled mid-ply: $((\theta/-\theta)_4)_S$ and the double clustered specimens have single outer plies: $\left((\theta/-\theta_2/\theta_2/-\theta_2/\theta)\right)_S$.

All angle-ply specimens have a length of 350mm and a width of 50 mm. The size of the specimens was selected to avoid a substantial dependence of edge delamination on the constitutive behavior. A gauge length of 250mm minimizes an influence of the clamped support. Three samples for each layup were sliced from the fabricated plates. A glass fiber/epoxy material was used for the end-tabs, see Section 3.6.2. The dimensions of the end tabs are 50x50mm² and the thickness is 1.0 mm.

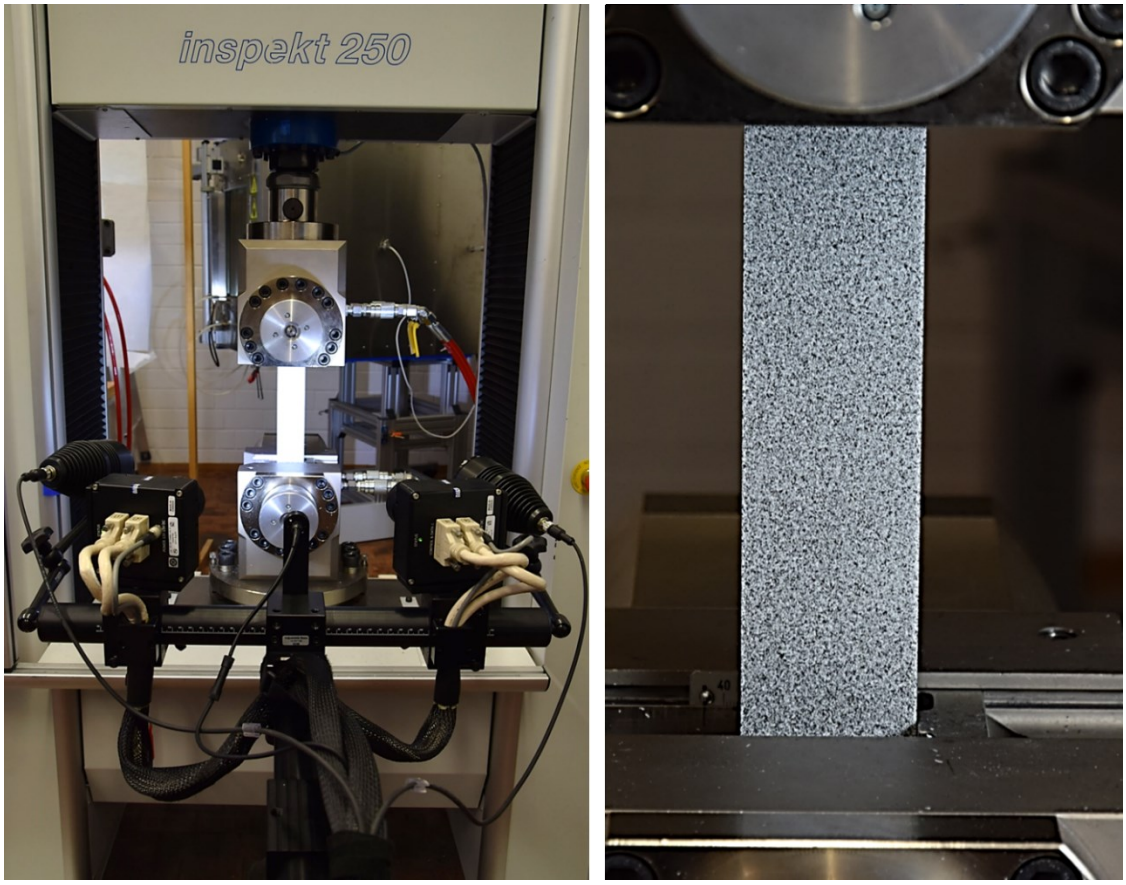

Fig. 3-40: Test setup for the angle-ply tests

The specimens were tested under tension in a load frame at a cross-head strain-rate of $0.0001s^{-1}$. All tests were conducted under displacement control. The strain was captured using a digital image correlation system *ARAMIS* ensuring a full-field strain measurement, see Fig. 3-40. This enables the determination of the global longitudinal strain ε_x and the global transverse strain ε_y at a virtual gauge area of 40x30mm².

The presented angle-ply tests for the IM7-8552 carbon/epoxy material are simulated in the explicit finite element solver of *ABAQUS*. The described material model has been embedded using a user-defined material *VUMAT*. To simulate the remote stress-strain response, the model uses a mesh of S4R shell elements. The boundary conditions are displacement controlled and the global strains are captured according to the virtual gauge area of the experimental data reduction. In the following, the axial stress-strain curves are compared for both, simulation and experiments. The prediction of the ultimate laminate strength is not part of the laminate hardening model, but is addressed in Section 4.5. Unfortunately, there is no material model available at present able to predict the ultimate failure of laminates without fibers aligned in load direction. For a better visualization of the difference between the single and double clustered specimens in the following diagrams the endpoints are marked by circles. Therefore, the mean value of the experimental measured laminate strength has been used.

±15°-Laminates

The stiffness of the ±15° angle-ply laminates is slightly increasing as load increases. The non-hookean stiffening in fiber direction is responsible for that behavior. The behavior in fiber direction has a stronger effect compared to the plastic flow due to the transverse compression and in-plane shear stresses. There is no recognizable difference between the single and double clustered specimens in the axial stress-strain diagram expecting the ultimate failure, which occurs a little bit earlier for the double clustered specimens, see Fig. 3-41.

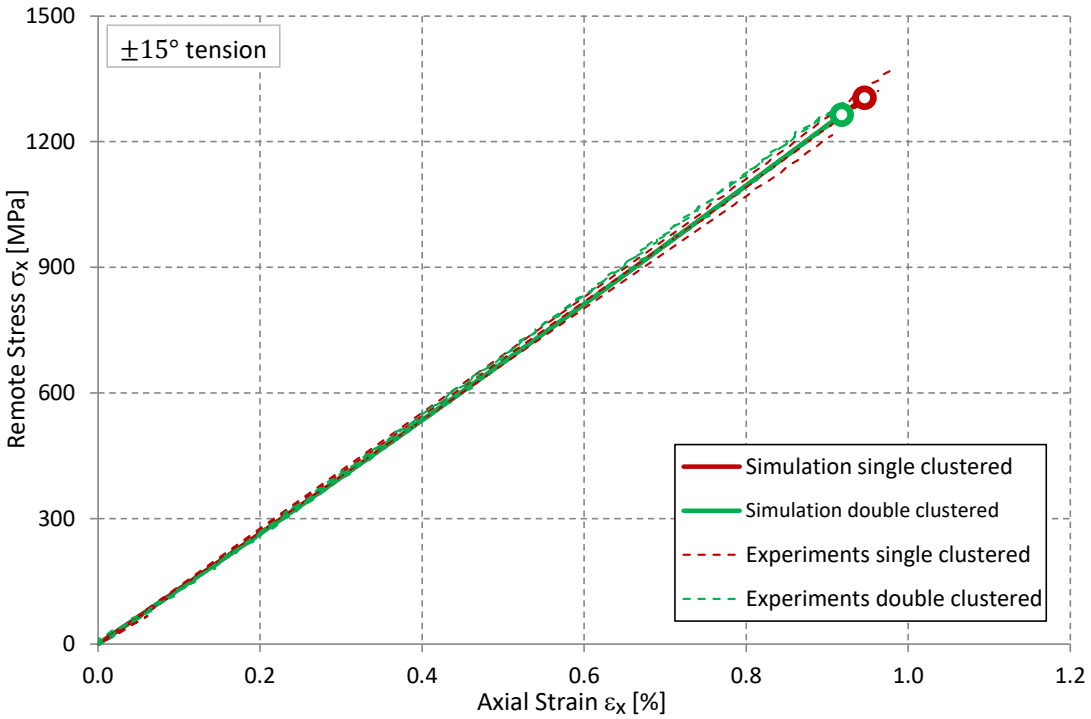

Fig. 3-41: Remote axial stress–strain response of ±15 laminate tension specimens for IM7-8552

±30°-Laminates

Referring to the axial strain, the largest deformation induced fiber angle change is achieved for the ±30° angle-ply laminates. To visualize the influence of fiber reorientation on the axial response, in Fig. 3-42 simulation results with and without considering fiber reorientation are given. The reorientation of fibers causes a distinct stiffening that countervails plastic yielding. Neglecting fiber reorientation can easily provoke a misinterpretation of the response of a ±30° tension test. Absent stiffening due to fiber rotation could mislead to a predicted influence of σ_{22} on the shear response in order to compensate for the missing stiffness. This wrongly assumed inner friction interaction would weaken the shear nonlinearity for a concurrent transverse compression.

In addition to the single and double clustered specimens also triple clustered specimens have been tested for the ±30° laminates. The exact layup for the triple clustered specimens is $(30/-30_3/30_3/-30)_S$. As the response curves of the triple clustered specimens lie between the curves of the single and the double clustered specimens, respectively, no discernable trend for the influence of the ply thickness could be observed. During the tests of the ±30° laminates little delamination formed at the outside edges. This was also indicated acoustically by a crackling noise. In contrast, inside the specimens no inter-fiber cracks could be found even for failed specimens. Nevertheless, the edge delamination is a possible factor influencing the axial stress-strain response. A clear tendency for an influence of the ply thickness on the ultimate laminate strength is given in the experimental results. The clustered specimens fail at significantly lower loading.

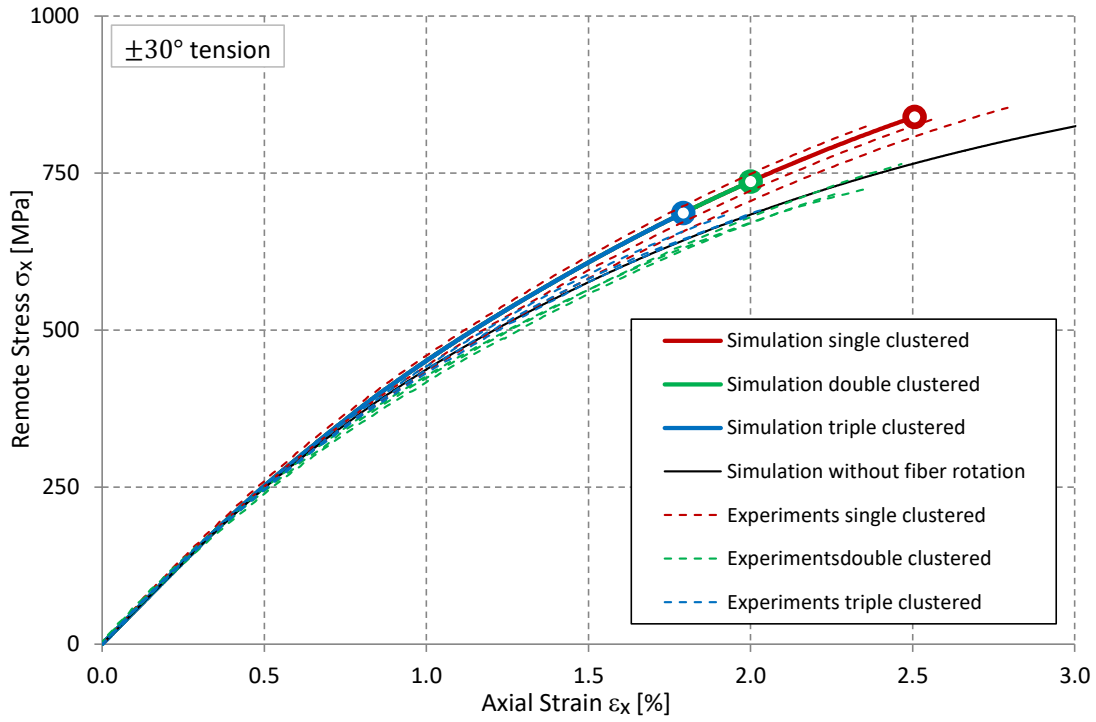

Fig. 3-42: Remote axial stress–strain response of ±30 laminate tension specimens for IM7-8552

±40°-Laminates

The largest in-plane shear strains without the influence of inter-fiber damage are achieved by the ±40° laminates. At large deformations the comparison of the simulated curves and the experimental measured curves cannot be used for validation, as the experimental results were used to define the longitudinal shear master-curve. The deviation process of the longitudinal shear master-curve is described in Section 3.3.4. Also for the ±40° laminates no difference in the stiffness profile is observable for the single and double clustered specimens. But the ultimate laminate failure occurs at a lower load level for the double clustered specimens, similar to the other off-axis angles.

This observation suggest only damage behavior to be dependent of the ply thickness (in-situ). Whereas the nonlinear constitutive behavior caused by plasticity seems not to be affected by the ply thickness.

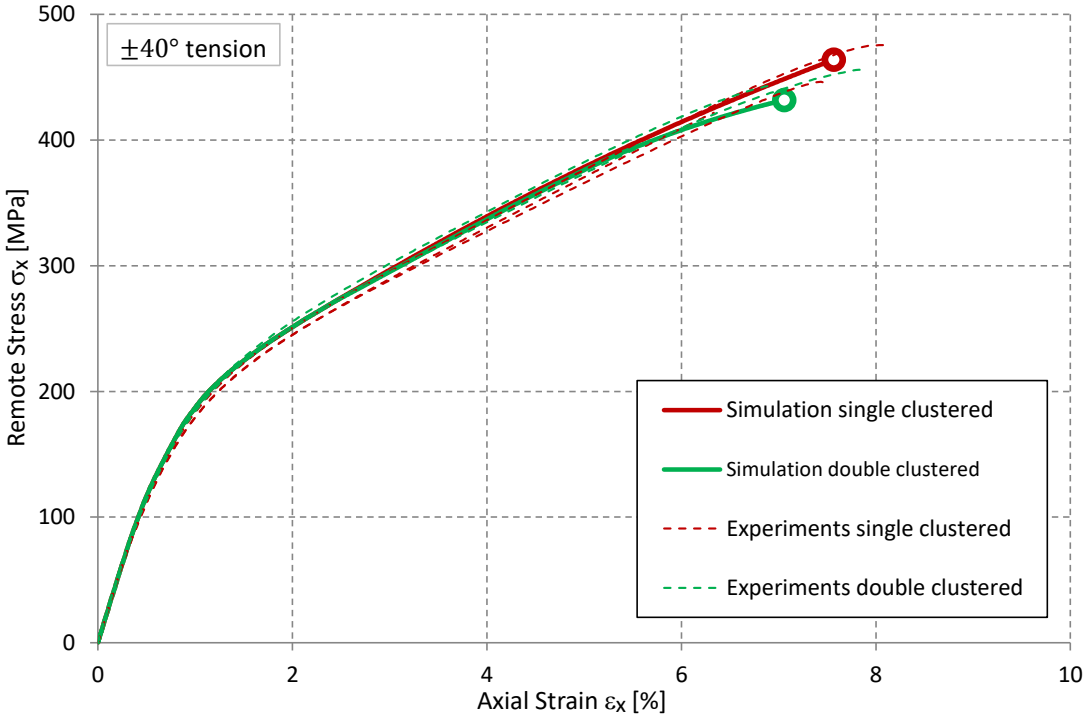

Fig. 3-43: Remote axial stress–strain response of ±40 laminate tension specimens for IM7-8552

Similar to the ±30° tension tests a noisy crackling can be heard during testing the ±40° laminates. In order to identify the cause of that sound, polished micrographs have been prepared from some of the tested specimens. Inside the specimens no cracks could be detected. But little edge delamination and edge chipping could be clearly seen, see Fig. 3-44. The influence of the edge effects should be negligible, as the damage extends only 0.2mm. Due to the wide specimen width of 50mm, only minor impact on the specimen's axial response can be assumed. Some of the ±30° and ±40° specimens have not been loaded to ultimate failure, but unloaded and reloaded after a waiting time of 500h. Based on the initial stiffness of the reloaded specimens, it could be shown that these specimens are not affected by damage [87].

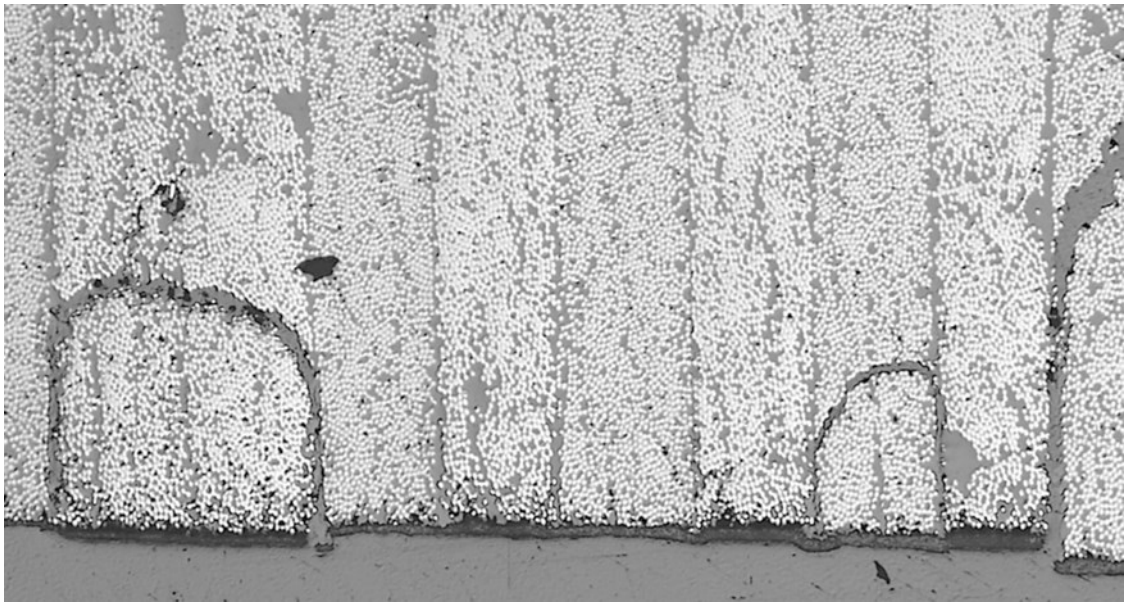

Fig. 3-44: Edge defects at a tested ±40 tension specimen

±45°-Laminates

Striking evolutions are exhibited by the $\pm 45°$ tension specimens. The inter-fiber damage initiation criterion is activated within the simulation at about 1.8% axial strain for the double clustered and at about 2.7% for the single clustered specimens. The subsequent damage progression provokes a softened axial stress–strain response. A stiffening of the laminates is induced again starting at approximately 6% axial strain. From then on, the influence of the deformation-driven fiber rotation dominates the laminate behavior. Initiation and evolution of inter-fiber damage strongly depends on the ply thickness. Compared to the alternating single clustered specimens the inter-fiber damage induced stiffness reduction of the double clustered specimens is much stronger. Also ultimate laminate failure is reached at a lower axial strain for the double clustered specimens.

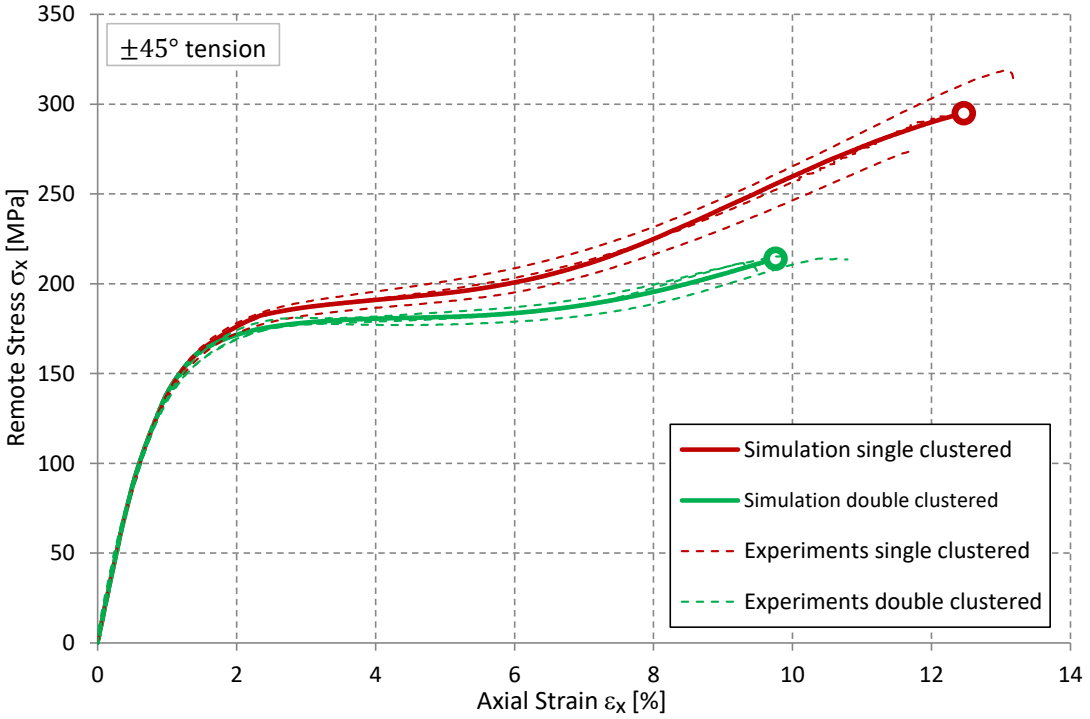

Fig. 3-45: Remote axial stress–strain response of ±45 laminate tension specimens for IM7-8552

The axial stress–strain response of the ±45° tension specimens is very important concerning the longitudinal shear nonlinearity. According to ASTM D 3518 [39], these laminates are used to predict the shear response. Fig. 3-46 compares the in-plane shear master curve used in the simulation and the curve determined by the standard approach presented in the ASTM D 3518. In contrast to the testing standard, the master curve for the numerical model is iteratively determined based on ±40° tension results, as described in Section 3.3.4. This kind of test enables large shear strains without damage influences. The ASTM specification allows for a validity of the shear stress–strain curve of up to 5% strain. The shown comparison indicates an increasing deviation from 2.5% shear strain. Therefore, damage and fiber rotation influences that are not detected in the test evaluation according to ASTM D 3518 are responsible. The testing of more narrow specimens increases the deviation from the master curve caused by free-edge delamination. To determine the longitudinal shear master curve, it is recommended to apply the ASTM method for small strains. While this is a simple approach at the beginning, for large deformations as exhibit for ±40° and ±45° laminates, it is more difficult. The calibration from ±40° tension results can therefore be advised, as it has been proven to be well suitable.

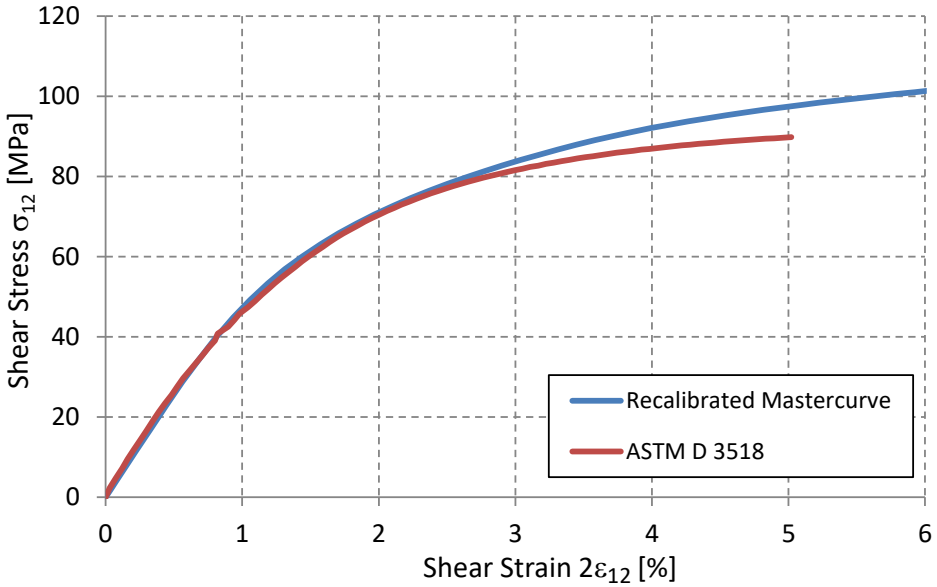

Fig. 3-46: Determined in-plane shear stress–strain curve according to ASTM D 3518 based on the single clustered ±45° tension tests and recalibration method for IM7-8552

±50°-Laminates

The constitutive behavior of $\pm 50°$ laminates is also strongly nonlinear. The proposed material model is able to simulate the laminate response very accurately. Shortly before ultimate failure, the laminate stiffness is slightly influenced by inter-fiber damage [87]. But neglecting damage would only result in a minor deviation from the test results at the end of the response curve, given in Fig. 3-47. The simulation result is notably more sensitive to the hydrostatic sensibility parameters α_{tr} and α_{sl}. In the single plies a transverse tensile stress is acting whereby a hydrostatic tensile load is acting within the laminate. This results in an increase of the plastic flow for longitudinal shear. The stiffness profile of the $\pm 50°$ laminates is only very little influenced by the thickness of the single plies in spite of little inter-fiber damage. But ultimate laminate failure is reached at a significantly lower axial strain for the double clustered specimens.

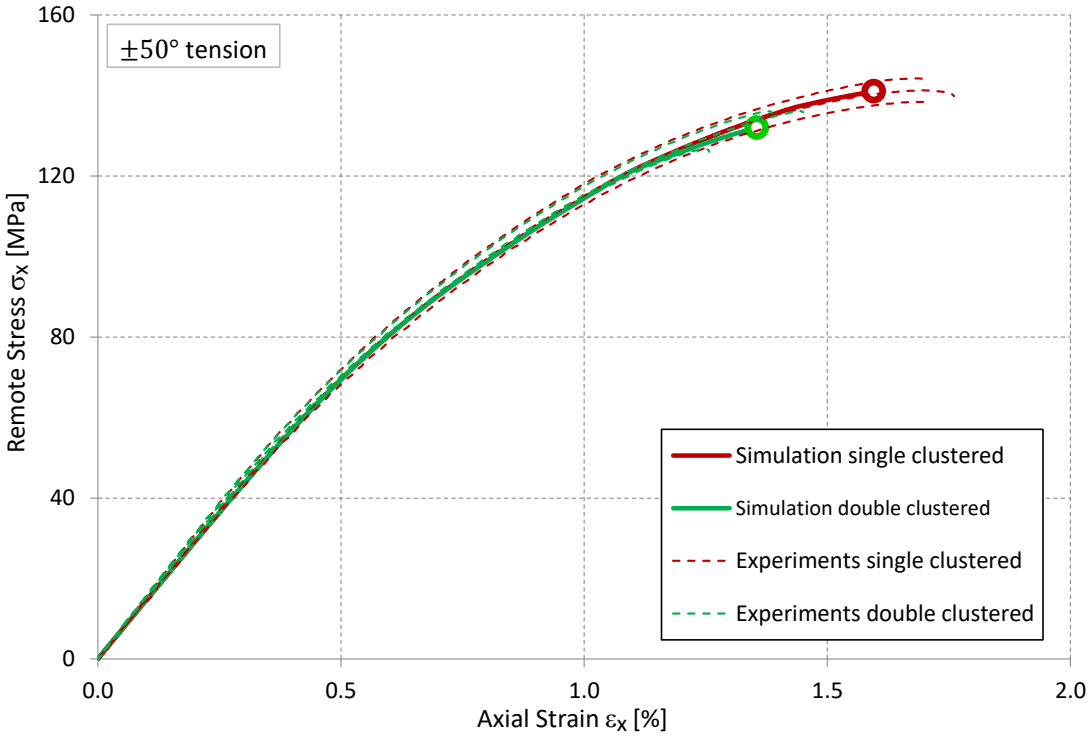

Fig. 3-47: Remote axial stress–strain response of ±50 laminate tension specimens for IM7-8552

±60°-Laminates

Because of their low elongation of break of 1.1% for single clustered and 1.0% for double clustered specimens, the constitutive behavior of the ±60° specimens is nearly linear, see Fig. 3-48. Also inter-fiber damage dose not influence the axial stress-strain response notably as inter-fiber damage initiation is immediately followed by ultimate laminate failure.

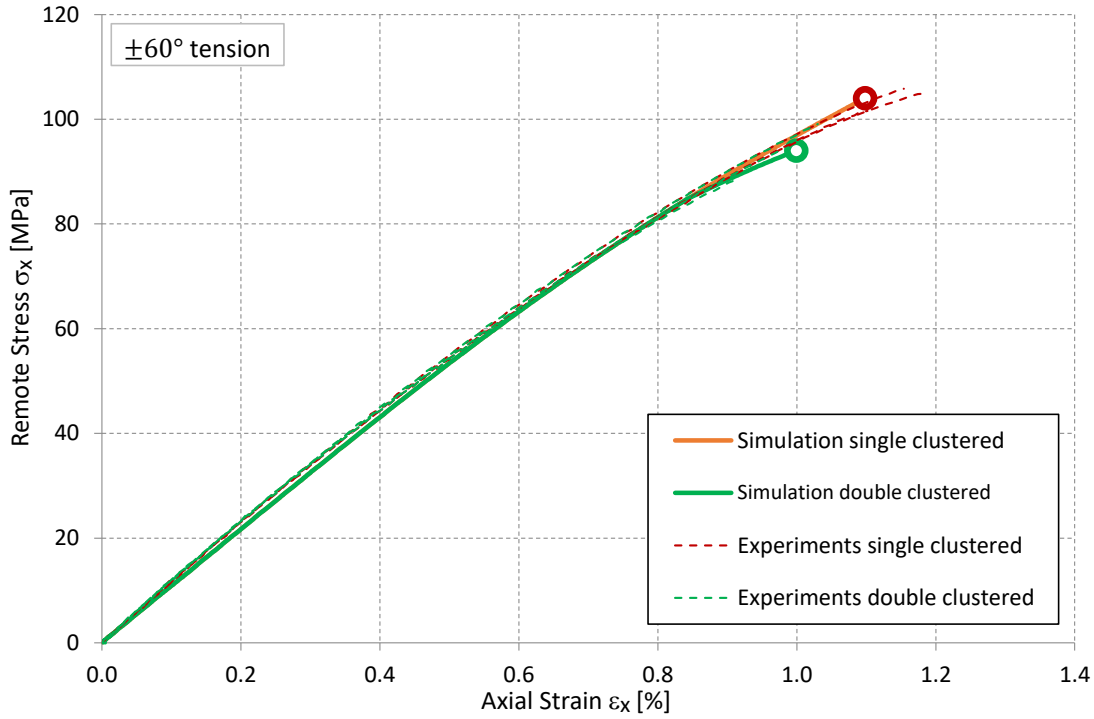

Fig. 3-48: Remote axial stress–strain response of ±60 laminate tension specimens for IM7-8552

±75°-Laminates

Also the stiffness behavior of the ±75° specimens is linear elastic up to final failure. Even for the single clustered specimens the failure strain is lower than 0.8%. As the ultimate laminate failure occurs simultaneously or even bevor inter-fiber damage initiation, no inter-fiber crack accumulation can be observed. Especially for the single clustered specimens no inter-fiber cracks are proposed by the presented material model at the point of ultimate failure, as shown in Fig. 3-30. However, the fracture pattern (see Fig. 4-22) suggests that final laminate failure occurs simultaneously with the first inter-fiber cracks. The laminate fracture plane is orientated parallel to the fibers of the outer plies, where inter-fiber cracks are expected first. Possibly the remaining laminate is not able to carry the load after the first crack in an outer ply. But also the assumed in-situ strength values are not valid for these laminates, where the difference in fiber orientation between adjacent plies is very little. The transverse tensile in-situ strength used for the simulations was determined based on 0°/90° laminates, see Section 3.4.3. As described in literature, the in-situ strength values depend on both, the corresponding ply thickness and the fiber orientation of adjacent plies [72]. At the moment there is no model available to estimate the in-situ strengths for arbitrary conditions. Also the angle-ply laminates do not provide enough information about damage initiation to develop a new approach on a sound basis. Therefore, in this thesis no extension of the model in this field has been done.

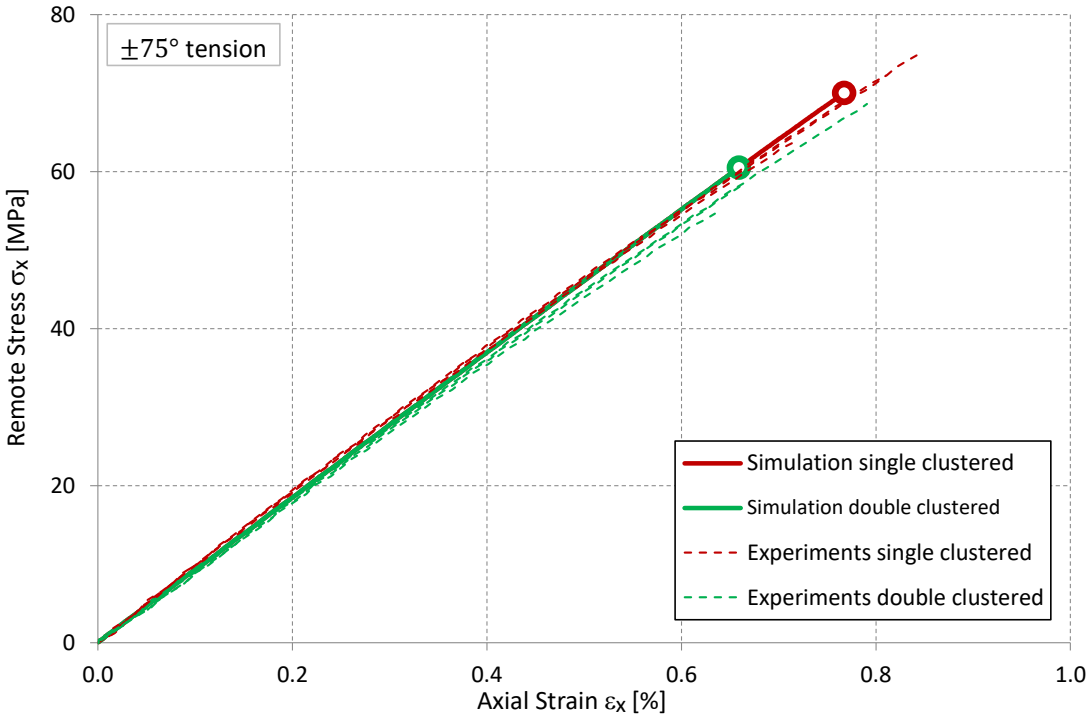

Fig. 3-49: Remote axial stress–strain response of ±75 laminate tension specimens for IM7-8552

3.7 Discussion about the Model's Applicability

The laminate hardening model has been subjected to a comprehensive validation to verify its capabilities and prediction accuracy. To this end a test series of angle-ply laminates with seven different off-axis angles has been conducted. Also two different layups have been tested for each off-axis angle in order to investigate the influence of ply thickness. On the one hand the plies were stacked alternating. On the other hand in two plies of the same orientation were clustered together before changing the fiber orientation. It was found out, that the ply thickness has only an influence on specimens where inter-fiber damage occurs. For the laminates where no inter-fiber cracks could be observed, the stress strain response of single and double clustered specimens was identical. But for all off-axis angles the double clustered specimens failed at a lower axial strain. A large width was chosen for the angle-ply specimens to minimize the influence of the free edges. A delamination driven failure mode has been avoided in this way. Thus, large axial strains could be obtained and thereon the verification of the model's applicability up to large deformations was possible. Additionally, the constitutive model was validated with off-axis compression tests from literature [49]. Using the same material system offers the determination of a single material parameter set for the simulation of both test series. The experimental basis for the model validation is very extensive in comparison to most literature. The model shows excellent correlation for all investigated specimens even at large deformations. Therefore, the

laminate hardening model provides a solid foundation for the subsequent laminate failure evaluation.

The highest potential for further improvements is certainly located in the area of inter-fiber damage. The initiation and propagation of inter-fiber cracks is strongly influenced by the surrounding laminate. In the presented model the thickness of the damaged ply is considered, but the influence of the fiber orientation of the adjacent plies is neglected. For reasonable improvements of the inter-fiber damage model, a comprehensive experimental study is mandatory. An interesting test series could be loading various laminates first in one direction to generate pre-existing damage in terms of inter-fiber cracks. For subsequent testing smaller specimens could be cut out at an angle of the already damaged laminates. Such results are very useful when designing structural parts for several load cases. To generate a more detailed understanding of inter-fiber damage processes, also the temporal progression of the crack density should be recorded.

Another important issue for damage initiation in laminates are internal thermal stresses resulting from curing and cool-down. Several analytical and numerical studies account on the determination of residual stresses in laminated composites [94–106]. In contrast experimental results are rare an always an interpretation. Three methods for the experimental measurement of residual thermal stresses can be found in literature. The first method is very critical, as here the stress at the point of inter-fiber crack initiation is compared to unidirectional strength values [94]. The second method is based on the extend of curvature of unbalanced laminates as thy cool down from their curing temperature to ambient conditions [96]. The third method is the most expensive one. Here the deformation after removing individual outer plies is measured [96]. Residual stresses in laminates seem to be very important for the prediction of inter-fiber damage initiation, but it is very difficult to estimate them correctly. A crucial issue is the long-term creep behavior of the epoxy matrix. For fiber-reinforced thermoplastics this effect is even more significant.

In current industrial applications usually laminate layups are used, where inter-fiber damage has only negligible relevance. But understanding initiation and propagation of inter-fiber cracks in laminates is very important to enable the application of less conservative layups in future applications. To this end, the investigation of inter-fiber damage can help to take the full advantage of the lightweight potential of carbon-fiber reinforced plastics.

While the inter-fiber damage model is only formulated for plane stress conditions, the plasticity model including deformation induced fiber-reorientation and non-hookean elasticity in fiber direction is formulated for three dimensional stress states. Therefore, the model is applicable for analyzing complex stress conditions at load transmission areas. The mechanism based formulation provides a sound physical basis allowing for sensible results for arbitrary loading conditions and large deformations. In order to evaluate failure, three dimensional failure criteria are available in literature. But the

consideration of layup effects and residual stresses on the failure behavior of the investigated ply is still a challenge.

The material model has been implemented as an *ABAQUS* user-defined subroutine *VUMAT* and can be used for explicit analysis. The model works robust and efficient, but requires a high quality finite element mesh because of the explicit solver. Even one small element reduces the stable time increment and therefore results in an enormous increase of the numerical effort. It can be summarized that the laminate hardening model can be used for many applications and provides very accurate results even at large deformations.

4 Laminate Softening

For the prediction of the maximum bearable load of a composite structure, damage models are necessary, since the first damage event often occurs much earlier than the ultimate failure of the laminate. Continuum damage models are particularly suitable, as in contrast to fracture mechanics approaches, like VCCT, no potential crack has to be predefined. Instead, a stress based failure criterion can be used to detect damage initiation. To enable mesh-size independent predictions, even at stress concentrations, Bažant and Oh [31] proposed the smeared crack band theory. The idea behind this approach is to relate the specific energy (area under the stress-strain curve), with the fracture energy of the material. To ensure this relation the softening modulus is defined as a function of the characteristic element length l^*. In Fig. 4-1 the representation of a crack by a continuum damage approach is shown.

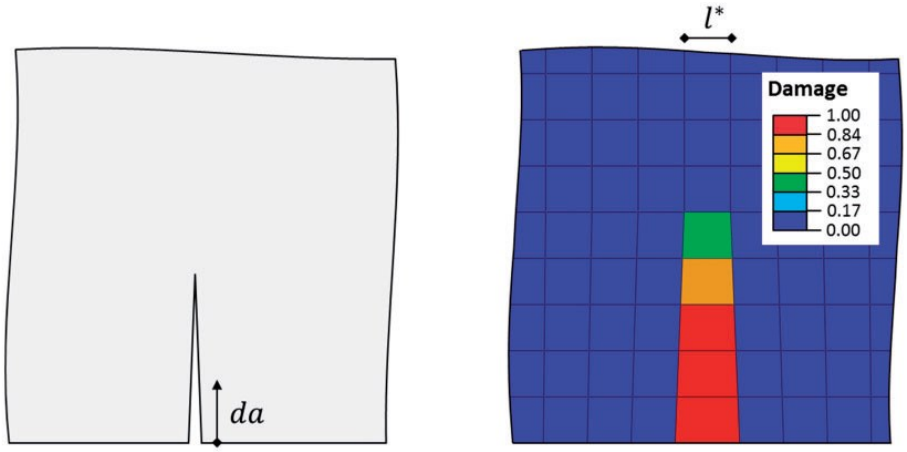

Fig. 4-1: Representation of a crack in a continuum damage approach [107]

Up to now, a couple of continuum damage models for unidirectional fiber reinforced plastics have been developed [3, 5–14, 23, 30, 57, 108–120]. These models have in common, that they are all defined on ply-level. This means, they describe the material behavior of a homogenized layer with unidirectional fiber orientation. For the prediction of the constitutive behavior of laminates, the ply-level material models require a very fine finite element model, where each ply is represented by one layer of elements. Between the plies cohesive elements are used to model delamination [121–129]. For industrial applications, usually layered shell elements are used to mesh composite structures to minimize the modeling and computational effort. Without the possibility of delamination between the plies, the ply-level models from literature provide wrong results [130].

The upcoming problems can be exemplified by an edge length study of a single element. Thereto, a layered shell element with quasi-isotropic layup $[+45/0/-45/90]_S$ is loaded with a uniaxial strain state ($\varepsilon_x^0 \neq 0, \varepsilon_y^0 = \varepsilon_{xy}^0 = \kappa_x = \kappa_y = \kappa_{xy} = 0$). In this study, the ply-level continuum damage model of Lapczyk and Hurtado [10] is used, which is implemented in the finite element solver *ABAQUS*. Up to damage initiation, detected by the Hashin criteria, the material model is linear-elastic. Once ply failure is predicted, the corresponding ply stiffness components are reduced, controlled by a linear energy-based degradation law. Therefore, the fracture toughness values for fiber tensile failure, fiber compressive failure, transverse tensile failure and transverse compressive failure have to be provided as material inherent model input. The material properties for Hexcel IM7-8552, used in this study, are given in Table 3-1, Table 4-1 and Table 4-2. The axial force-mid-plane strain response of the single element is shown in Fig. 4-2 for various element-sizes.

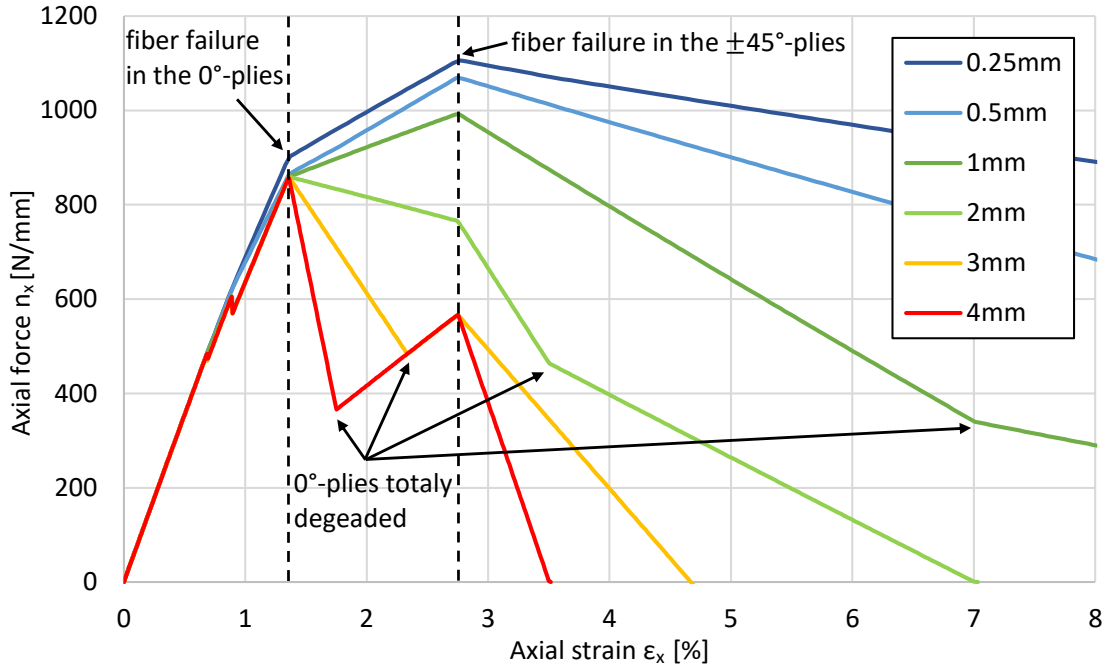

Fig. 4-2: Axial force-mid-plane strain of a layered shell element with quasi-isotropic layup for various element-sizes, using the material model of [10]

The shapes of the curves strongly depend on the element-size. For small elements the axial force can still be increased after reaching fiber failure in the 0°-plies and results in its maximum value, when reaching fiber failure in the ±45°-plies. Responsible is the definition of the energy-based softening on ply-level. The smaller the element, the slower proceeds the stiffness degradation, so that within the corresponding ply of a totally failed element, always the same amount of energy has been dissipated. For small elements the stiffness degradation in the 0°-plies occurs so slowly, that in combination with the residual stiffness of the surrounding laminate results in a further increase in

load. For larger elements, the stiffness degradation in the 0°-plies occurs faster in accordance with the axial strain. This is why the axial laminate force begins decreasing after reaching fiber failure in the 0°-plies. This drop can be so significantly severe, that the laminate load can be further increased after the stiffness in the 0°-plies is totally degraded and fiber failure in the ±45°-plies is still expected. The characteristics of the curves in the axial laminate force strain diagram is different for various element-sizes. From this, it becomes clear that the laminate's fracture toughness (area under the curves in Fig. 4-2 multiplied with the element area) is strongly influenced by the element size. As the laminate's fracture toughness is crucial for layered elements and not the energy dissipated within certain plies, this mesh-size dependency impedes reliable simulation results. For small elements, even the laminate strength gets overrated, depending on the element-size.

The shown element-size study clearly denotes, that energy-based continuum damage approaches on ply-level are not reasonably useable in combination with layered elements. If these approaches are used together with a fine modelling technique, where each ply is represented by one layer of elements and the plies are connected with cohesive elements, these material models work better [130]. Subjected to suitable material data and element properties for the cohesive zone, different test setups can be simulated. Chen [130] demonstrates a good correlation between numerical and experimental results of open-hole tension tests. All of the evaluated specimens consist of a quasi-isotropic layup with varying size-scaling and ply clustering. The experiments showed different failure mechanisms with a diverging degree of delamination, depending on the size and layup conditions, see Fig. 4-3 [131]. The simulations exhibit a distinct mesh-size dependency for the specimens failing with large delamination. For the specimens failing under the brittle mechanism, the simulation results have been proven to be widely mesh-size independent. But the failure mechanism is not correctly represented in the simulation. During simulation only the 0°-plies fail due to fiber failure and the rest of the laminate fails by large delamination and inter-fiber failure, in the experiments the whole laminate fails in one fracture plane. That means that also the fibers in the ±45°-plies break and only unessential delamination can be found.

Inter-fiber damage is represented totally wrong, when using energy-based degradation to compensate mesh-size influences. An energy-based degradation law is only suitable when damage localizes at on element row. Within a laminate inter-fiber damage does not localize, but rather covers a wide area in certain plies. Therefore, the degradation law for inter-fiber damage should not be mesh-size dependent. In the presented laminate based model inter-fiber damage is formulated on ply level, but is only based on the stress and strain conditions and not the element size. An energy-based degradation law is only used for the representation of ultimate laminate failure in the proposed model.

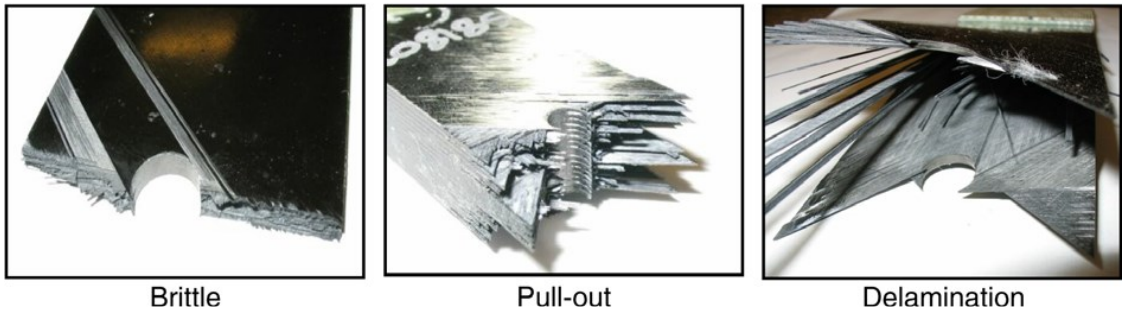

Fig. 4-3: Different failure mechanisms in open-hole tension tests [131]

Previously published continuum damage models for composites, like [7–10, 13, 30, 109] are all defined on ply-level. A crucial drawback of these material models is, they require fine meshing techniques and are not applicable in combination with layered elements. This results in enormous numerical effort, thus preventing their application in industry.

In contrast to the ply-level approaches, ultimate laminate failure and the subsequent material softening of the presented model is defined on laminate-level. This ensures the applicability of the model in combination with computationally efficient layered shell elements. Another benefit is, that on laminate-level brittle laminate failure can be described much more accurately, compared to a ply-level definition. As a consequence, inter-fiber damage allowing for a load increase, is not addressed by the laminate softening model, but is considered in the laminate hardening model, see Section 3.4. This Section refers to ultimate laminate failure, where damage evolution describes the separation process of the laminate. So the objective of the damage evolution formulation given here is to provide mesh size independent results and not to control the chronology of different failure mechanisms. A concise description of the laminate softening model is already published, see [132].

4.1 Laminate Failure Criterion

The laminate softening begins with the initiation of ultimate laminate failure. Fiber failure in at least one ply almost always results in ultimate laminate failure [28]. Usually, the residual laminate is not able to carry the load of the failed ply and the crack cannot be stopped by the adjacent plies. Using a fiber failure criterion on ply-level works well for detecting ultimate laminate failure, if the considered laminate contains fibers aligned in the principle load direction. However, if there is no ply orientated in load direction, ultimate laminate failure usually occurs at a stress state, where no fiber failure is predicted. The ultimate failure of such a laminate can have several reasons. One reason is, the laminate stress-strain response descends due to cumulative inter-fiber failure, leading to a localization of the process zone. For other laminate layups the local stress state at the free edge of the considered structure is responsible for the initiation of ultimate failure. It should be noted that in laminates stress states are acting that cannot occur uniaxial loaded unidirectional specimens. For laminates, where no fibers are

aligned in load direction, new ultimate failure criteria defined on laminate-level have to be developed. Exemplarily in Section 4.5 it is shown, that all tested angle-ply laminates fail without relevant delamination, while in no ply fiber, failure is predicted. The occurring failure mechanisms of these laminates are discussed in Section 4.5 based on the ply stress data and the fracture surfaces. In the presented study the laminate softening model is validated with quasi-isotropic open-hole tension test results. For this application a fiber failure criterion is suitable. Like in common failure criteria for unidirectional composites, the maximum stress criterion is used to detect fiber failure [26–29].

$$f_E^{1+}{}_k = \frac{\sigma_{11_k}}{XT} \tag{4-1}$$

$$f_E^{1-}{}_k = \frac{-\sigma_{11_k}}{XC} \tag{4-2}$$

4.2 Damage Evolution

For a reliable prediction of the ultimate strength of a composite structure, in addition to the strength of the laminate, its fracture toughness is necessary. Without the fracture toughness a stress concentration at a notch cannot be evaluated. In metal design, this material parameter is often combined with the notch geometry to a notch factor for strength reduction. In a finite element analysis the initiation of failure at a notch significantly depends on the mesh-size. To enable mesh-size independent predictions of the ultimate strength, the subsequent stiffness degradation has to compensate the mesh effect on damage initiation. Therefore, Bažant and Oh [31] proposed their crack band theory, in which fracture is modeled as a band of parallel densely distributed micro-cracks (smeared crack band).

During laminate softening, the laminate stiffness of the failing element is controlled by the energy dissipation of the crack evolution. Therefore, the current non-elastic components of the deformation state is frozen, when ultimate laminate failure is reached. The current non-elastic mid-plane strains and curvatures at the point of ultimate failure initiation are obtained by subtraction of the elastic deformations from the total deformations

$$\begin{Bmatrix} \boldsymbol{\varepsilon}_{pl}^0 \\ \boldsymbol{\kappa}_{pl} \end{Bmatrix} = \begin{Bmatrix} \boldsymbol{\varepsilon}^0 \\ \boldsymbol{\kappa} \end{Bmatrix} - \begin{Bmatrix} \boldsymbol{\varepsilon}_{el}^0 \\ \boldsymbol{\kappa}_{el} \end{Bmatrix}, \tag{4-3}$$

where the elastic mid-plane strains and curvatures can be calculated using the elastic laminate stiffness ABD-matrix

$$\begin{Bmatrix} \boldsymbol{\varepsilon}_{el}^{0} \\ \boldsymbol{\kappa}_{el} \end{Bmatrix} = \begin{bmatrix} \boldsymbol{A} & \boldsymbol{B} \\ \boldsymbol{B} & \boldsymbol{D} \end{bmatrix}^{-1} \begin{Bmatrix} \boldsymbol{n} \\ \boldsymbol{m} \end{Bmatrix}. \tag{4-4}$$

Following the effective stress concept, first the effective stress state is calculated. This theory was introduced for general continuum damage models by [133, 134]. The effective forces and moments can be computed by multiplication of the undamaged elastic stiffness matrix to the elastic deformation

$$\begin{Bmatrix} \boldsymbol{n}' \\ \boldsymbol{m}' \end{Bmatrix} = \begin{bmatrix} \boldsymbol{A} & \boldsymbol{B} \\ \boldsymbol{B} & \boldsymbol{D} \end{bmatrix} \begin{Bmatrix} \boldsymbol{\varepsilon}_{el}^{0} \\ \boldsymbol{\kappa}_{el} \end{Bmatrix}. \tag{4-5}$$

When fiber failure is predicted in at least one ply, the components of the forces and moments acting on the predicted fracture plane are reduced to zero. In the presented model the fracture plane is defined to be perpendicular to the fiber direction of the ply where fiber failure is predicted. This is an assumption that is only correct if the analyzed laminates contains fibers aligned in the principle load direction. For arbitrary laminates and loading conditions more extensive formulations to determine the laminate strength and fracture plane orientation are necessary. The degradation analysis is performed in such a way that the energy dissipation predicted by the numerical model equals the fracture toughness of the material.

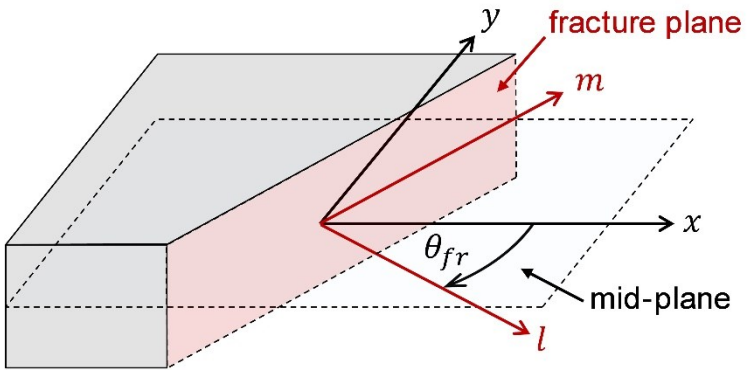

Fig. 4-4: Coordinate system aligned with the crack

Therefore, the effective forces and moments in the global coordinate system $\{\boldsymbol{n}', \boldsymbol{m}'\}_{xy}^{T}$ are rotated to the coordinate system of the fracture plane

$$\begin{Bmatrix} \boldsymbol{n}'_{lm} \\ \boldsymbol{m}'_{lm} \end{Bmatrix} = \begin{bmatrix} \boldsymbol{R}(\theta_{fr}) & \boldsymbol{0} \\ \boldsymbol{0} & \boldsymbol{R}(\theta_{fr}) \end{bmatrix} \begin{Bmatrix} \boldsymbol{n}'_{xy} \\ \boldsymbol{m}'_{xy} \end{Bmatrix}, \tag{4-6}$$

where the transformation matrix $\boldsymbol{R}(\theta)$ is given in Eq. (3-5) and the fracture angle θ_{fr} is defined as the fiber orientation of the ply, in which fiber failure is detected

$$\theta_{fr} = \theta_{k_{failure}}. \tag{4-7}$$

The direction of rotation required in Eq. (3-5) is defined normal to the laminate: $\boldsymbol{n}^{\theta} = \{0, 0, 1\}$. The coordinate system aligned with the crack is illustrated in Fig. 4-4. The effective traction $\boldsymbol{t}'$, consisting of effective forces and moments acting on the fracture plane is given as

$$\boldsymbol{t}' = \{n_l', n_{lm}', m_l', m_{lm}'\}^T. \tag{4-8}$$

To represent the crack in the simulation, the components of traction are reduced by a scalar damage variable d_{Lam} such that the nominal tractions are defined as

$$\boldsymbol{t} = \{(1 - d_{Lam})n_l', (1 - d_{Lam})n_{lm}', (1 - d_{Lam})m_l', (1 - d_{Lam})m_{lm}'\}^T. \tag{4-9}$$

The components n_m' and m_m' of the load vector are not influenced by damage, as they act perpendicular to the crack. The nominal forces and moments expressed in the fracture plane coordinate system are

$$\begin{Bmatrix} \boldsymbol{n}_{lm} \\ \boldsymbol{m}_{lm} \end{Bmatrix} = \begin{bmatrix} \boldsymbol{M} & \boldsymbol{0} \\ \boldsymbol{0} & \boldsymbol{M} \end{bmatrix} \begin{Bmatrix} \boldsymbol{n}_{lm}' \\ \boldsymbol{m}_{lm}' \end{Bmatrix}, \tag{4-10}$$

where the damage tensor $\boldsymbol{M}$ is defined as

$$\boldsymbol{M} = \begin{bmatrix} 1 - d_{Lam} & 0 & 0 \\ 0 & 1 & 0 \\ 0 & 0 & 1 - d_{Lam} \end{bmatrix}. \tag{4-11}$$

The nominal forces and moments are next rotated back to the global coordinates. The evolution of the damage variable d_{Lam} defines how much energy is dissipated during the failure process. If moisture and temperature influences are neglected, the laminate's complementary free energy density can be divided into an elastic-damage part and a plastic part

$$g = g_{ed} + g_{pl}. \tag{4-12}$$

The elastic-damage part of the complementary free energy density is

$$g_{ed} = \frac{1}{2}\{\boldsymbol{\varepsilon}_{el}^0, \boldsymbol{\kappa}_{el}\}\{\boldsymbol{n}, \boldsymbol{m}\}^T \tag{4-13}$$

and the plastic part is

$$g_{pl} = \frac{1}{2}\{\boldsymbol{\varepsilon}_{pl}^0, \boldsymbol{\kappa}_{pl}\}\{\boldsymbol{n}, \boldsymbol{m}\}^T. \tag{4-14}$$

According to the effective stress concept [133, 134], the energy dissipation rate Y_{Lam} only depends on the elastic-damage potential energy

$$Y_{Lam} = \frac{\partial g}{\partial d_{Lam}} = \frac{\partial g_{ed}}{\partial d_{Lam}}. \tag{4-15}$$

The dissipated energy per unit of laminated area g_c^{Lam} can be calculated by integrating the rate of dissipation

$$g_c^{Lam} = \int_{d=0}^{1} Y_{Lam}\, \mathrm{d}d_{Lam}. \tag{4-16}$$

On the other hand, the fracture energy g_c^{Lam} depends on the experimentally measureable fracture toughness G_c^{Lam} per unit fracture surface and the size of the corresponding finite element:

$$G_c^{Lam} A = g_c^{Lam} \frac{A\, l^*}{t_{Lam}}. \tag{4-17}$$

The fracture surface A, the characteristic element length l^* and the thickness of the laminate t_{Lam} are illustrated in Fig. 4-5. The determination of the laminate's fracture toughness G_c^{Lam} is discussed in Section 4.3.

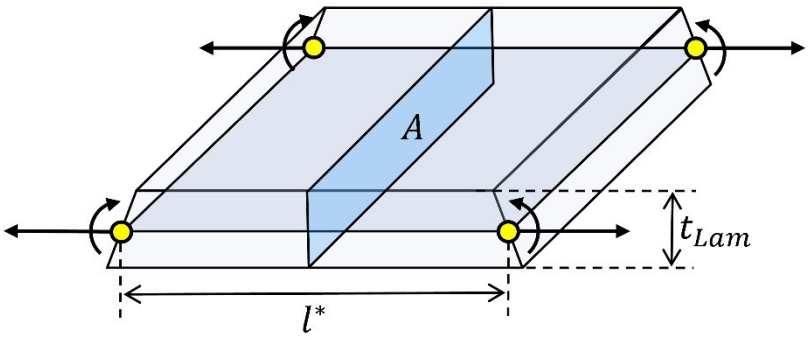

Fig. 4-5: Finite shell element, loaded normal to the fracture plane

If fiber failure in at least one ply is responsible for the laminate failure, the load acting in fiber direction of the critical ply or plies is the driver of the failure process. Therefore, a possible shear force n_{lm} and torsional moment m_{lm}, acting on the fracture plane is neglected by damage evolution law. Continuum damage models from literature [7–10, 13, 30, 109] typically ignore shear forces on the fracture plane in the damage evolution law for fiber failure.

If only load normal to the fracture plane is acting ($n_m = n_{lm} = m_m = m_{lm} = 0$), Eq. (4-16) can be simplified to

$$g_c^{Lam} = \int_{d=0}^{1} \frac{\partial\left(n_l \varepsilon_{el,l}^0 + m_l \kappa_{el,l}\right)}{2\, \partial d_{Lam}}\, \mathrm{d}d_{Lam}. \tag{4-18}$$

The dissipated energy, given by Eq. (4-18), can be determined by the area under the n_l-$\varepsilon^0_{el,l}$ curve (Fig. 4-6) aggregated with the area under the m_l-$\kappa_{el,l}$curve (Fig. 4-7).

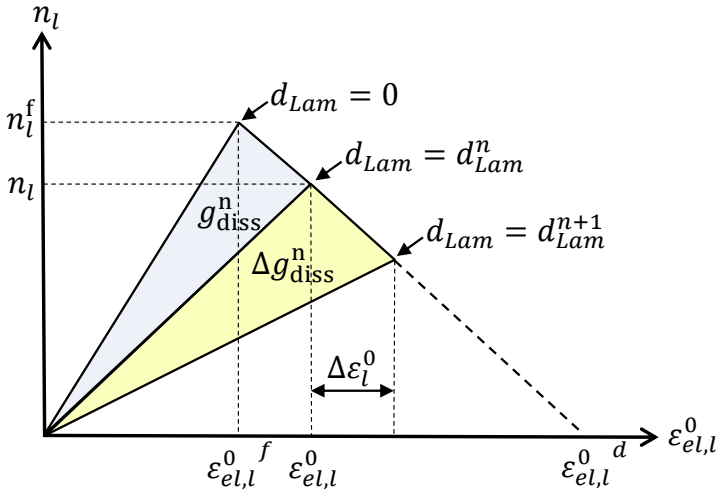

Fig. 4-6: Visualization of the dissipated energy in the axial force-strain diagram

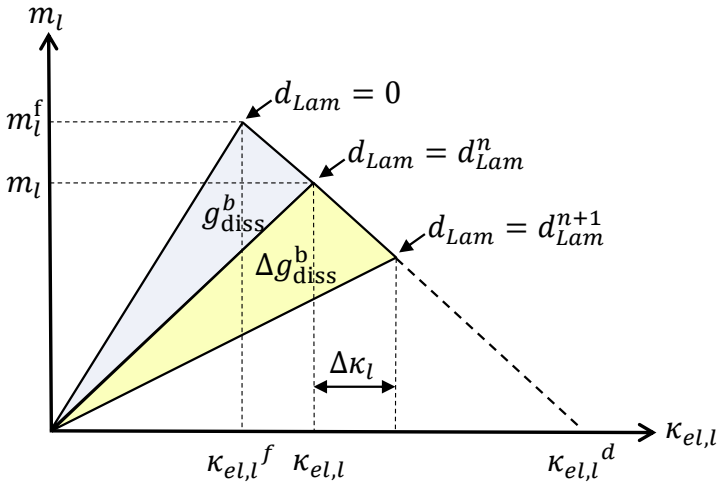

Fig. 4-7: Visualization of the dissipated energy in the axial moment-curvature diagram

During softening, at each time step, the laminate damage variable d_{Lam} is updated to represent the progression of the damage state:

$$d_{Lam}^{n+1} = \min\left(\max\left(\frac{\varepsilon_{el,l}^0\left(\varepsilon_{el,l}^0 + \Delta\varepsilon_l^0 - \varepsilon_{el,l}^{0\ d}\right)}{\left(\varepsilon_l^0 + \Delta\varepsilon_{el,l}^0\right)\left(\varepsilon_{el,l}^0 - \varepsilon_{el,l}^{0\ d}\right)}, d_{Lam}^n\right), 1\right). \tag{4-19}$$

The parameters of this equation are visualized in Fig. 4-6 and Fig. 4-7. The elastic mid-plane strain at which the material is fully damaged ($d_{Lam} = 1$), $\varepsilon_{el,l}^{0\ d}$ is defined as

dissipated energy of a fully failed material equals the laminate's fracture toughness g_c^{Lam}:

$$\frac{1}{2}\left(n_l {\varepsilon_{el,l}^0}^d + m_l {\kappa_{el,l}}^d\right) = g_c^{Lam} - g_{diss}. \tag{4-20}$$

In Eq. (4-20), $g_{diss} = g_{diss}^n + g_{diss}^b$ designates the energy which has already be dissipated. Between ${\varepsilon_{el,l}^0}^d$ and ${\kappa_{el,l}}^d$ the following correlation is derived at to ensure they are reached at the same time

$$\frac{\Delta\varepsilon_l^0}{{\varepsilon_{el,l}^0}^d - \varepsilon_{el,l}^0} = \frac{\Delta\kappa_l}{{\kappa_{el,l}}^d - \kappa_{el,l}}. \tag{4-21}$$

4.3 Determination of the laminate fracture toughness

The fracture toughness is a material property which describes the ability of a material containing a crack to resist fracture. It is defined as the energy required to grow a thin crack. For fiber reinforced composites, of course the fracture toughness depends on the failure mode. The fracture toughness for a transverse crack initiated by normal tensile load can be measured by the Double Cantilever Beam (DCB) test according to ASTM-D 5528 [135], see Fig. 4-8. In the DCB test, the delamination growth between unidirectional 0°-plies is observed. The resulting fracture toughness G_1^t is typically also used for in-plane cracks.

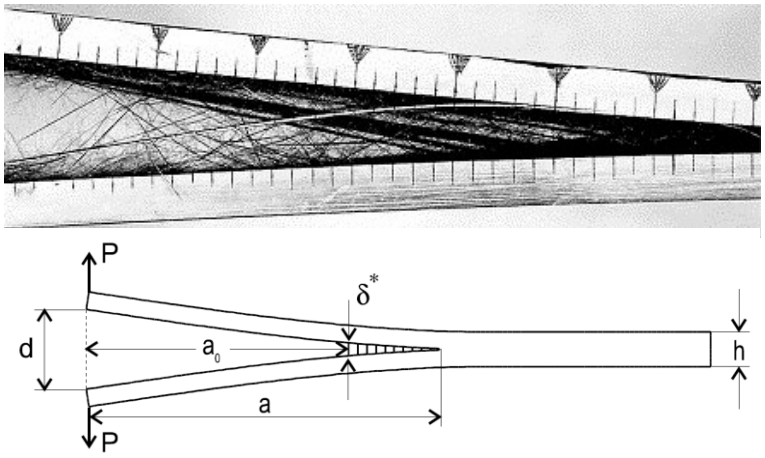

Fig. 4-8: Double cantilever beam test [136]

The shear mode component of the fracture toughness G_6 can be measured using Three- or Four-Point End Notched Flexure (ENF) test specimens, see ASTM-D7905 [137], see

Fig. 4-9. The fracture toughness for transverse compression loading G_2^c can be calculated approximately using the shear component and the fracture angle α ($\approx 53 \pm 3°$):

$$G_2^c = \frac{G_6}{\cos \alpha}. \tag{4-22}$$

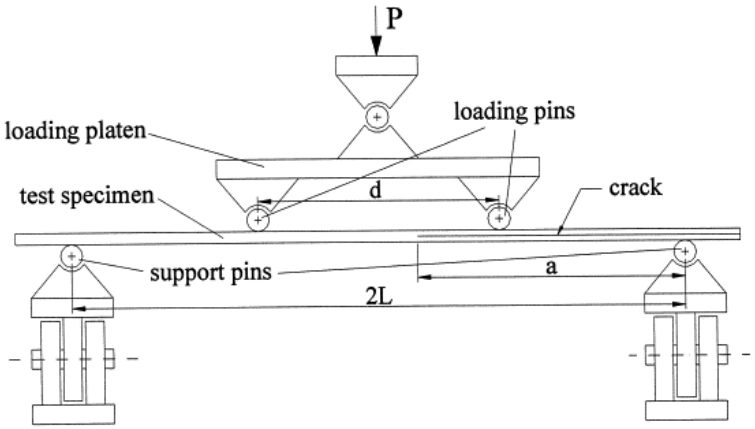

Fig. 4-9: Four-point end notched flexure test [138]

There is no standard test method to measure the fracture toughness for tensile fiber failure. Laffan [139] shows a method how to measure the value using the compact tension (CT) specimen configuration. Six method of data reduction were investigated for calculation of the fracture toughness with the aim of finding the best technique, in terms of reproducibility and simplicity. The proposed optimum method does not rely on the use of an optically measured crack length, which is hard to determine accurate enough.

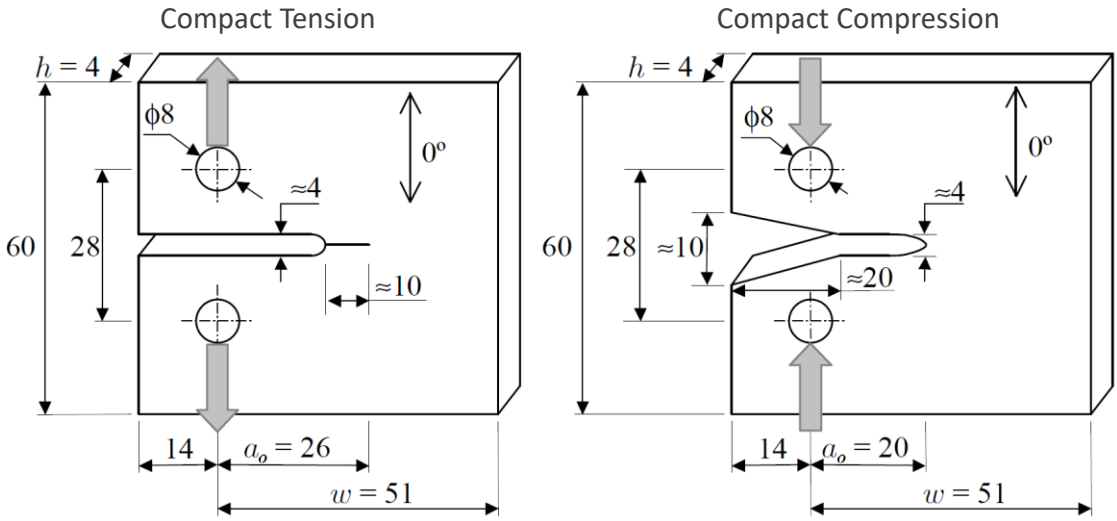

Fig. 4-10: Compact tension and compact compression test [140]

The measurement of the energy dissipation associated with compressive loading in fiber direction is far more complex. Bažant [31] proposed an approximation of the fracture toughness for fiber failure in compression based on the shear component of the fracture toughness G_6:

$$G_1^c = \frac{w}{s} G_6, \tag{4-23}$$

where w is the kink band thickness and s is the distance between two matrix cracks. This expression requires good knowledge of the kink band geometry, which is affected by the geometry and the loading of the structure. Also energy dissipation due to friction involved sliding of the crack faces is neglected. An experimental method to determine the fracture toughness of compressive fiber failure is proposed by Pinho [140]. Compact compression (CC) tests were performed to determine the fracture toughness associated with kink band failure. Another experimental procedure to measure the fiber compressive fracture toughness is described by Laffan [141]. Here, notched unidirectional four point bending tests provide the required data.

In Table 4-1, the fracture toughness values for fiber failure and inter-fiber failure for the material Hexcel IM7-8552 are given. In order of magnitude, the values for fiber failure exceed the values for inter-fiber failure by a hundredfold. It can therefore be concluded that laminate fracture toughness G_c^{Lam} is dominated by the fracture toughness of the plies failing, due to fiber failure.

Table 4-1: Fracture energies for a unidirectional reinforced ply [110]

Description	Symbol [Unit]	Hexcel IM7-8552
Fracture Energy for Longitudinal Tension	G_1^t [kJ/m²]	81.5
Fracture Energy for Longitudinal Compression	G_1^c [kJ/m²]	106.3
Fracture Energy for Transverse Tension	G_2^t [kJ/m²]	0.2774
Fracture Energy for Transverse Compression	G_2^c [kJ/m²]	1.3092
Fracture Energy for Longitudinal Shear	G_6 [kJ/m²]	0.7879

An additional important effect of the fracture toughness for fiber failure is, that it depends strongly on the thickness of the corresponding ply. Laffan [142] found out, that fracture toughness of double clustered 0°-plies within a cross-ply laminate is about twice as big as the fracture toughness of single clustered 0°-plies. Responsible for this effect is the fiber pullout-effect. In thick layers with unidirectional fiber orientation the fracture process zone is much larger and therefore, the longer pieces of fibers have to be pulled

out during the separation process. The occurring friction causes the greater magnitude of the fracture toughness. In Fig. 4-11 the fracture surfaces of $0°/90°$ cross-ply laminates are given. On the left side, the $0°$ and the $90°$ plies are alternating after each ply. In contrast on the right side, instead of single $0°$ plies always two plies are clustered. So the total thickness of the $0°$-layers on the left side is 0.125mm and on the right side 0.25mm.

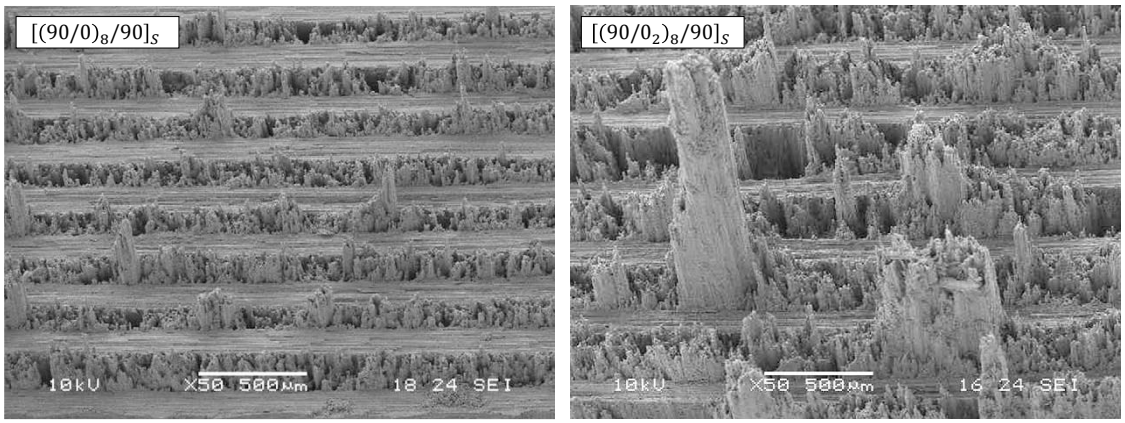

Fig. 4-11: Fracture surfaces of cross-ply laminates [142]

The influence of hydrothermal conditions on the translaminar fracture toughness has been investigated by Marín [143]. The results of double edge notched tensile tests show that the fracture toughness for hot and wet conditions is higher than for wet or dry conditions at room temperature. The fiber pull-out length and the frictional coefficient have been identified as the most significant parameters controlling the crack propagation and the fracture toughness.

The fiber-matrix interface is one of the most important properties influencing the fracture toughness. An improvement of the fiber-matrix interface results in an increase of the strength, but simultaneously in a reduction of the fracture toughness [144]. An increase of the laminate fracture toughness to improve the resistance of composites at notches enters the focus of current research in the field of carbon composites. An interesting approach is to mix different types of carbon fibers. Due to the different strength and failure strains some fibers fail earlier than the rest. Due to multiple fiber cracking and pull-out the fracture toughness can be increased significantly [20].

On basis of the results of Laffan [142], it must be considered that also the kind of load in-plane or bending influences the laminate's fracture toughness G_c^{Lam}. Moreover, it is important to mention, that experimental determination of the fiber fracture toughness is complicated and not always very clear. In the literature for the same material (IM7-8552) values for G_1^t from 81.5 kJ/m² up to 131.7 kJ/m² can be found (all values are for single $0°$-plies embedded in $90°$-plies).

For the determination of the fracture toughness of multidirectional laminates, in [145] a simple model is predicted using the fracture toughness of the $0°$-plies. To estimate the

fracture toughness of a general multidirectional laminate without fibers in load direction, reliably, new and comprehensive studies are necessary. Experimentally, the laminate's fracture toughness can be measured by open-hole tension (OHT) and open-hole compression (OHC) tests [146], here the specimen's strength is significantly influenced by the energy dissipating during laminate failure. The specific parameter for the material model is preferably determined by re-simulation of the experiments.

In summary, it can be stated that fracture toughness values for a unidirectional ply are no material intrinsic properties. They are strongly influenced by the kind of load, by the adjacent plies within a laminate and especially by the ply thickness. The most important information to estimate the fracture toughness of a laminate is the number and the thickness of the plies, which are orientated in the principle load direction. Different mechanisms are fundamentally responsible for the quantity of energy dissipated during failure. In the fracture zone chemical bounds are dissolved, plastic deformations use energy and furthermore friction effects can result in a great amount of dissipated energy. If no fibers are aligned in load direction, the laminate fracture toughness cannot be estimated by the models available in literature. Therefore, further experimental investigations are mandatory. In Section 4.5 the failure mechanisms of the tested angle-ply laminates are discussed based on their fracture surfaces.

4.4 Validation and Model Verification

The laminate softening model is only implemented for two dimensional problems. As all specimens used for validation have a mid-plane symmetric layup, this assumption is suitable for the validation cases. But for the analysis of structural parts the model has to be implemented for shell elements. In *ABAQUS* it is not possible to define the general shell stiffness within a user-defined subroutine for explicit time integration. A possibility to implement the proposed material is to define a user-defined element. This is much more extravagant and has therefore not been done for this thesis. A user-defined code for *ABAQUS* is always less efficient than a model integrated by the software developer. By this reason, a user-defined element would as well be just a solution for academic applications.

To demonstrate the model's applicability, open-hole tension tests are particularly suitable, as not only the strength of the laminate is validated, but also its fracture toughness. In [110] an experimental study of open-hole tension tests is presented. Within this investigation specimen with the same quasi-isotropic layup $[90/0/\pm 45]_{3S}$ are varied in the hole-diameter and the specimen width. The hole-diameter to width and hole-diameter to length ratios are kept constant. The experimental results show a decrease of the open-hole tension strength with an increasing hole-size, see Fig. 4-12. The presented laminate damage model achieves a very good agreement with the experiments. As material input for the model, the data given in Table 4-2 is used for the softening model. For the laminate hardening model the properties given in Table 3-1 are

used. In Section 4.3 the determination of the laminates fracture toughness is discussed. For the simulation of the open-hole tension tests the laminate fracture toughness is determined on basis of the experimental results of the 2mm hole-diameter specimens. Using the value $G_c^{Lam} = 29\text{kJ/m}^2$ as input for the simulation results in an exact accordance of the experimentally measured and the numerical determined open-hole tension strength for the specimens with 2mm hole-diameter. Alternatively, the laminate fracture toughness G_c^{Lam} could be estimated based on the fracture toughness for fiber tensile failure G_1^t, by applying the model of [145]. This method would result in a similar value for G_c^{Lam}. However, the values for the tensile fiber fracture toughness G_1^t are scattered throughout literature, so a direct determination method is chosen. For the simulation of the other specimen geometries the same value for the laminate fracture toughness has been used. Thus, the applicability of the presented material model can be demonstrated for these hole-diameters. The mesh-size of the simulation models is 0.5mm for all specimen geometries.

Table 4-2: Material parameters for the laminate softening model [110]

Description	Symbol [Unit]	Hexcel IM7-8552
Longitudinal Tensile Strength	$R_{\parallel}^t$ [MPa]	2326.2
Longitudinal Compression Strength	$R_{\parallel}^c$ [MPa]	1200.1
Laminate Fracture Toughness	G_c^{Lam} [kJ/m²]	29.0

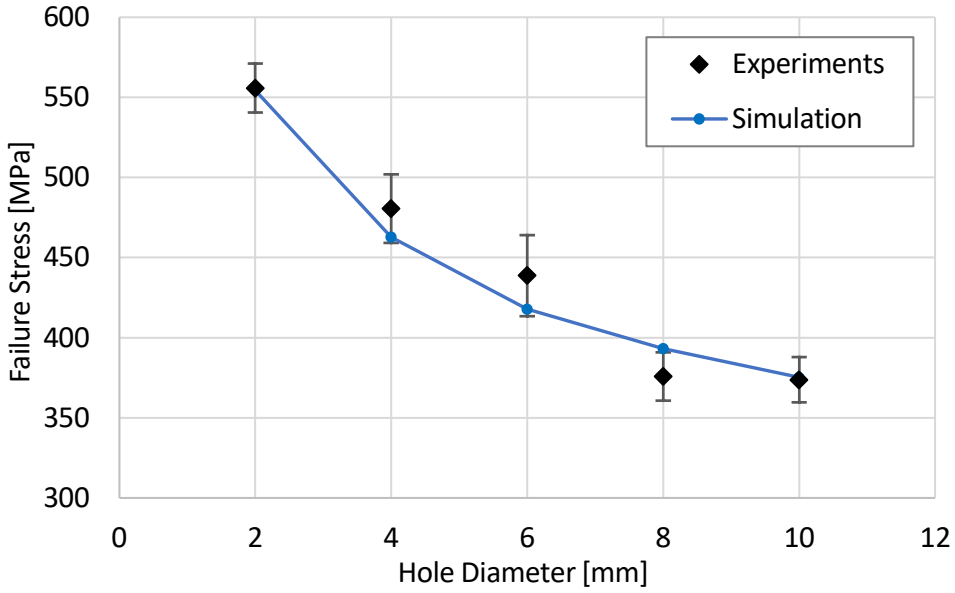

Fig. 4-12: Open-hole tension strength for different hole-diameters. Experiments from [110]

To evaluate the mesh-size independence of the model, the open-hole tension test with the 2mm hole-diameter was simulated with different mesh-refinements. The results of

this study are given in Fig. 4-13. The deviation in strength prediction of the different meshes is very slight according to the absolute value. With the exception of the course mesh with 1mm element edge length, all simulation results are inside the standard deviation of the experimental results. Applying an energy based stiffness degradation leads to a maximum allowed element size, because the internal energy of an element at the point of damage initiation must not be greater than the fracture toughness [7–10, 13, 30, 109]. The critical element size can be calculated by Eq. (4-24):

$$l^*_{max} = min\left(\frac{2\,G_c^{Lam}\,t_{Lam}}{\left(n_l^f\,{\varepsilon^0_{el,l}}^f\right)}, \frac{2\,G_c^{Lam}\,t_{Lam}}{\left(m_l^f\,{\kappa_{el,l}}^f\right)}\right). \tag{4-24}$$

As the fracture plane orientation depends on the ply, causing the ultimate failure, for each possible fracture plane angle the critical element size has to be checked. For the quasi-isotropic layup of the shown open-hole tension study, the critical element size is l^*_{max} = 5.0mm. However, already for meshes with smaller elements than the maximum allowed, the predicted open-hole tension strength increases with a coarser mesh. If the discretization is too coarse close to a stress concentration, damage initiation occurs too late and the degradation analysis is not able to compensate the gap in damage initiation. A possibility to deal with this problem is to reduce the corresponding strength value [10]. But this comes along with wrong predictions for homogeneous loaded regions of the laminate.

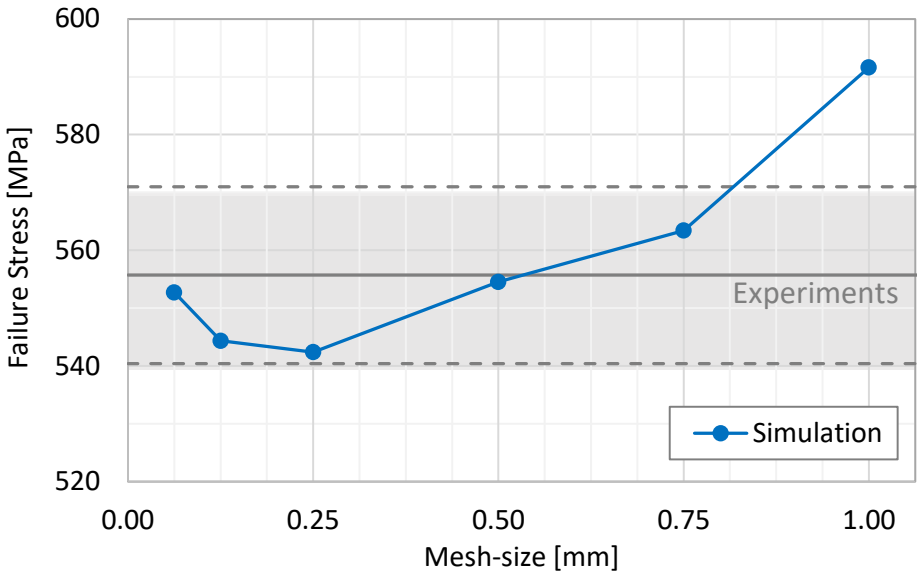

Fig. 4-13: Open-hole tension strength for different mesh-sizes. Experiments from [110]

4.5 Discussion about the Model's Applicability

The laminate hardening model has been comprehensively validated in Section 3.6. The model has shown excellent correlation with off-axis compression and angle-ply tension tests, even at large deformations. The following focuses on ultimate laminate failure prediction and laminate softening. Composite structures, consisting of layered thin unidirectional plies, with a relative wide geometry tend to a brittle ultimate failure behavior. This means, these structures fail without excessive delamination. Such a failure mechanism is in principle representable by a finite element model composed of layered shell elements. If the fibers in one layer are aligned in the principle direction of the force flux, a fiber failure criterion on ply-level is suitable to predict ultimate laminate failure. The subsequent softening analysis requires the laminate fracture toughness G_c^{Lam}. To establish this, an estimation model is already available in literature [145]. The laminate fracture toughness can also be determined experimentally, based on open-hole [146] or center cracked specimens [145].

If the presented constitutive laminate model is compared with models defined on ply-level, from literature [7–10, 13, 30, 109], the following issues must be observed according to their applicability on structural parts. Regarding the modeling and numerical effort, the laminate model offers the major advantage, that it is applicable to layered elements. Thereby the amount of degree of freedoms of the finite element model drops significantly. Using layered elements also allows an easy change of the laminate layup definition. This is an important advantage for complex composite structures.

To demonstrate the applicability of the presented laminate model in combination with layered shell elements, the single element study described in the introduction of Section 4 has been repeated, but now applying the presented laminate model. The results are given in Fig. 4-14. The curves for all different element-sizes show the same characteristic behavior. Only the degree of the descent depends on the element-size in such a way, that the dissipated energy of a fully failed element becomes independent of element-size.

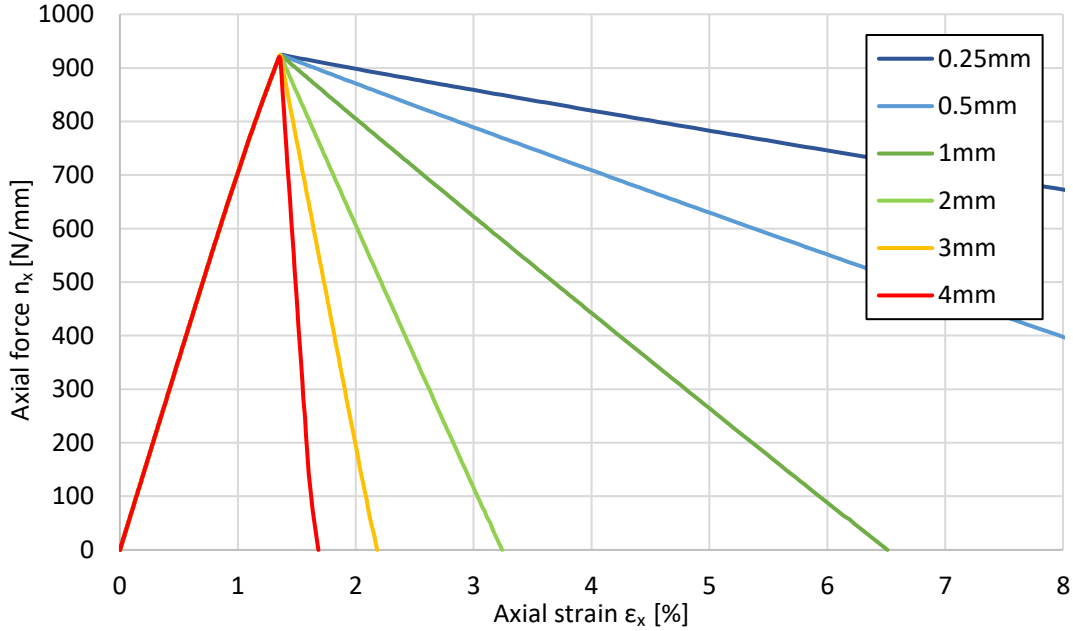

Fig. 4-14: Axial force-mid-plane strain of a layered shell element with quasi-isotropic layup for various element-sizes using the presented laminate model

In Fig. 4-15 the evolution of the laminate damage variable d_{Lam} during the simulation of an open-hole tension test with quasi-isotropic layup is shown for two different mesh sizes. The figure visualizes clearly how the mesh size regularization in terms of the energy-based degradation law works. The fine mesh represents the stress concentration close to the hole more accurate. As a consequence damage initiation begins earlier in comparison to the courser mesh. But for the fine elements the failure strain for total degradation is much larger, so during the damage progression the course mesh catches up the difference in damage initiation and the finale failure takes place almost simultaneously for both discretization methods.

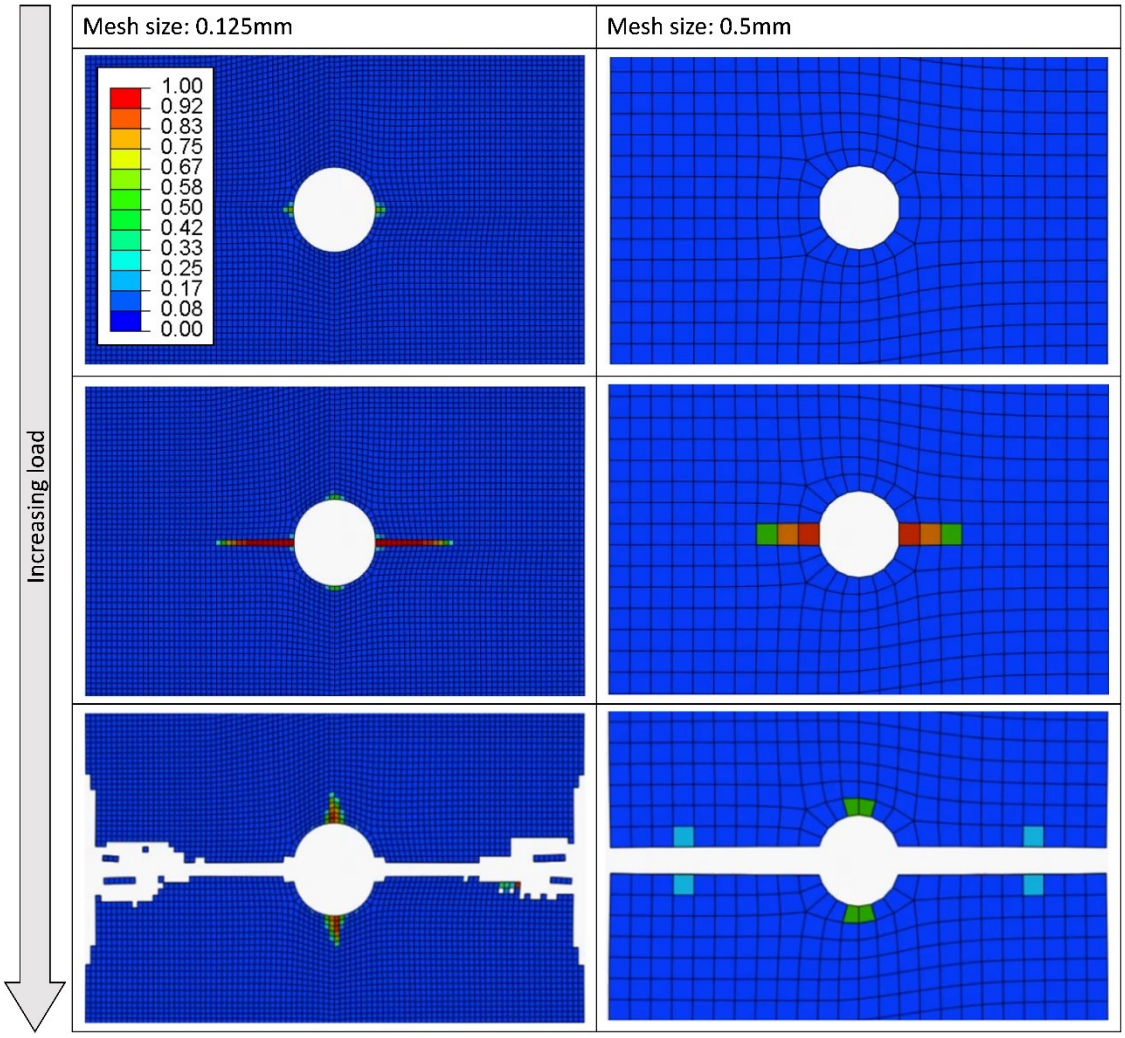

Fig. 4-15: Open-hole tension Simulation of a QI-laminate: Comparison of different mesh sizes based on the laminate damage variable d_{Lam}

If the laminate layup consists of thick unidirectional layers or the component geometry exhibits a small width, delamination can play a crucial role in the ultimate laminate failure mechanism. In this case, the presented laminate model is not suitable in combination with layered elements. Furthermore, the finite element model requires possibilities to represent delamination. An amplification of the model to deal with such problems is realizable without neglecting the consideration of the laminate in its entirety. To realize this, the finite element solver has to consider all elements, stacked in thickness direction of the laminate in one evaluation step. Another possibility is the application of complex element formulations, e.g. XFEM-approaches, which are able to represent a separation of the element itself due to delamination.

For general laminates, ultimate failure mechanisms can occur, which are not describable with ply-level material models. To investigate the failure behavior of laminates without fibers aligned in the main load direction, the failure mechanisms of the angle-ply tension tests, presented in Section 3.6.4 are discussed in this section. In Table 4-3 the strength

values of all angle-ply specimens are summarized. For all off-axis angles, the double clustered specimens failed at a lower strength value than the single clustered ones. But the difference in laminate strength varies over the off-axis angle. For a more detailed discussion, the fracture surfaces and failure mechanisms of the investigated angle-ply tensions tests are shown and discussed in the following.

Table 4-3: Laminate Strength of the angle-ply tension tests in [MPa]

	Clustering	Specimen 1	Specimen 2	Specimen 3	Mean		STDV	CV
±15°	single	1321.84	1215.68	1379.08	1305.53		67.70	5.2%
	double	1266.53	1293.00	1235.00	1264.84	-3.1%	23.71	1.9%
±30°	single	827.62	836.66	854.00	839.43		10.94	1.3%
	double	718.60	724.46	764.22	735.76	-12.3%	20.27	2.8%
	triple	682.18	682.93	692.91	686.00	-18.3%	4.89	0.7%
±40°	single	446.44	475.66	469.74	463.95		12.61	2.7%
	double	397.90	443.25	456.05	432.40	-6.8%	24.95	5.8%
±45°	single	273.85	318.83	293.23	295.30		18.42	6.2%
	double	211.67	215.41	214.29	213.79	-27.6%	1.56	0.7%
±50°	single	138.42	141.29	144.21	141.31		2.37	1.7%
	double	126.69	136.08	136.15	132.97	-5.9%	4.44	3.3%
±60°	single	101.60	105.83	104.86	104.10		1.81	1.7%
	double	88.46	94.19	99.09	93.91	-9.8%	4.35	4.6%
±75°	single	63.74	72.23	75.22	70.40		4.86	6.9%
	double	54.65	58.10	68.63	60.46	-14.1%	5.95	9.8%

±15°-Laminates

During the ultimate failure process of $\pm 15°$-laminte similar to pure unidirectional fiber tension specimens a lot of energy is dissipating. The specimen fragments into many pieces accompanied by a load bang. An interesting phenomenon is that the fracture plane is oriented perpendicular to the load direction instead of the fiber direction, see Fig. 4-16. Therefore, in all plies the fibers have to break during the separation process. This fracture behavior is different to observations made by Herakovich [147]. He has tested $\pm 10°$ and $\pm 30°$ angle-ply laminates under tension. Also brittle laminate fracture was observed, but the fracture plane was parallel to the fibers of the outer plies. Thus, only in half of the plies fiber breakage occurred. Also for the double clustered $\pm 15°$ specimens the failure mechanisms of the conducted tests and the tests from Herakovich are significantly different. While the double clustered $\pm 15°$ specimens presented here failed

similar to the single clustered at a slightly lower strength (-3.1%), a delamination driven failure mechanism was observed by Herakovich for double clustered specimens. That means that the separation of the specimens was a result of fiber-parallel inter-fiber cracks and extensive delamination. According to his studies, the local stress state at the free edges are responsible for that failure mechanism. When comparing the results of Herakovich and the results presented in this thesis it should be noted that both the material system (IM7/8552 and T300/5208) and the specimen geometry are different. To minimize the effect of edge effects a wide specimen geometry of 50mm was used for the presented angle-ply test series. In contrast, the specimens of Herakovich had only a width of 12mm and additionally consisted of only half the number of plies (8 instead of 16).

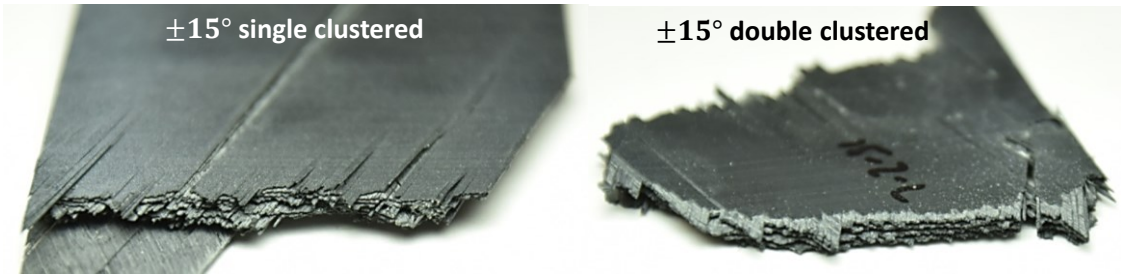

Fig. 4-16: Fracture surface of ±15° laminates

Classical failure criteria for carbon fiber reinforced composites are incapable of predicting the ultimate failure of the $\pm 15°$ specimens. At the point of failure, in the single clustered specimens a smeared stress state of $\sigma_1 = 1306\text{MPa}$, $\sigma_2 = -71\text{MPa}$ $\sigma_{12} = 50\text{MPa}$ is acting. Particularly critical is the fact, that classical failure criteria, e.g. the Puck criterion, overestimate the strength of this laminate significantly. To define new failure conditions, the observed failure mechanisms has to be analyzed more detailed. First the influence of the free edge on the laminate failure has to be quantified. Therefore, tests with tubular specimens could be conducted. Additionally the exact stress state acting in the fibers and acting in the resin could be analyzed by micromechanical models.

±30°-Laminates

In addition to the single and double clustered specimens also triple clustered specimens have been tested for the $\pm 30°$ laminates. The exact layup for the triple clustered specimens is $(30/-30_3/30_3/-30)_S$. The failure mechanism is especially for the single and double clustered specimens very similar to the failure behavior of the ± 15 laminates. Also the $\pm 30°$ specimens fail perpendicular to the load direction, in a way that the fiber break in all plies. At the point of failure (single clustered specimens) a stress of $\sigma_1 = 1056\text{MPa}$ is acting in fiber direction. Compared to the fiber tension strength $R_{\parallel}^{t} = 2550\text{MPa}$ the prevailing stress level is far away from failure initiation. In contrast to the $\pm 15°$ laminates, inter-fiber damage is initiated by the Puck criterion. But

this should be interpreted with caution, as for the ±40 laminates much higher stress exposures for inter-fiber failure are predicted, while in polished micrographs no inter-fiber cracks could be found.

There is a striking reduction of the laminate strength with increasing ply-clustering. In comparison to the single clustered specimens, the double clustered specimens fail under a reduced strength of 12.3%. The strength of the triple clustered specimens is even 18.3% lower than the strength of the single clustered ones. Locking closer at the fracture surfaces of the ±30° specimens, it is recognizable that at a small range at the edge of the specimens the fracture mechanism is not brittle. The separation is here given by a combination of inter-fiber cracks and delamination. This range becomes significantly larger with increasing ply-clustering, see Fig. 4-17. This effect suggests, that especially for the clustered specimens the local stress state at the free edges becomes important for the separation process and influences the strength of the specimens. Further investigations are necessary to differentiate between the influence of the specimen width and the free edge stresses on the specimen strength. For example experiments with various specimen width could be conducted. But also very interesting is the laminate strength not affected by the free edge effect. Therefore, additional experiments with pipe specimens would be beneficial.

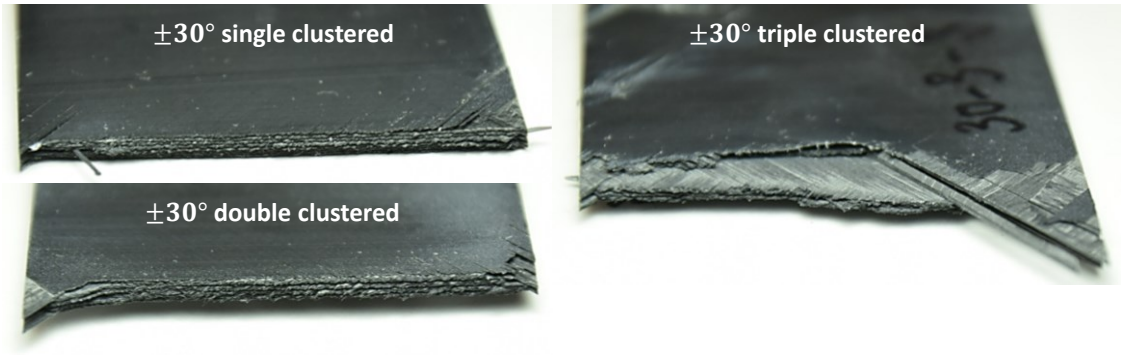

Fig. 4-17: Fracture surface of ±30° laminates

±40°-Laminates

The failure mechanism of the ±40° tension specimens is significantly different in comparison to the ±15° and ±30° laminates. For this layup the fracture plane is aligned parallel to the fibers of the outer plies, instead of normal to the load direction. As a consequence the fibers break only on half of the plies. As mentioned in Section 3.6.4 no inter-fiber cracks can be observed in the ±40° specimens even shortly before ultimate failure. In the “un-damaged” area of already failed specimens a few isolated inter-fiber cracks could be found. Unfortunately, it is not possible to find out when these cracks occurred, before ultimate failure or during the spring-back impulse after ultimate failure. The difference in strength between single clustered and double clustered specimens is relatively moderate at 6.8%. Significantly different fracture surfaces result from the single and double clustered specimens, see Fig. 4-18. At all specimens, small fiber

bundles protrude out of the fracture plane. For the single clustered specimens these fiber bundles are finer and in particular considerably shorter (5mm compared to 15mm) in comparison to the double clustered specimens (5mm to 15mm). Moreover, the length of the fiber bundles varies much more for the double clustered specimens. At all specimens little delamination can be found at all layer interfaces at the specimen edges close to the fracture zone.

Fig. 4-18: Fracture surface of ±40° laminates

±45°-Laminates

The $\pm 45°$ tension tests show the biggest difference between the strength of single and double clustered specimens (-27.6%). When comparing the single and double clustered $\pm 45°$ specimens it must be considered that the axial response of both specimen types differs from 2% axial strain, see Fig. 3-45. Ultimate failure occurs at approximately 13% for the single clustered specimens and at 10% axial strain for the double clustered specimens. The reason for the different stiffness behavior lies in inter-fiber damage processes. Both inter-fiber damage initiation and propagation is dependent on the ply thickness. As a result in the double clustered specimens a much stronger stiffness degradation due to inter-fiber cracks takes place. Polished micrographs have shown that the crack density in both specimens is similar [87]. But the crack sliding displacement is much higher in a ply with doubled thickness. As a consequence a crack in a thick ply leads to a stronger stiffness reduction than a crack in a thin ply. The ultimate failure mechanism is similar for both single and double clustered specimens, see Fig. 4-19. Similar to the $\pm 40°$ laminates, the specimens break along the fibers of the outer plies. Thus only the fibers in half of the plies need to break. The protruding fiber bundles are longer and coarser for the $\pm 45°$ laminates in comparison to the $\pm 40°$ laminates. Close to the specimen edges the fibers do not need to break as the delamination reaches the free edge. This behavior is especially observable at the double clustered specimens.

Even tough inter-fiber cracks occur at about 15-20% of the failure strain, the specimens sustain further loading for a long period of time. During loading, high transverse compressive load results from the interaction of plasticity and fiber reorientation. As a consequence the inter-fiber stress exposure decreases due to inner friction towards the end of the tests. Ultimate failure may be triggered by reaching a critical inter-fiber crack density at a local area of the specimen. At this critical crack density delamination

between neighboring cracks occur in a way that the whole load has to be carried by plies with the same fiber orientation. This would explain the high number of inter-fiber cracks in the plies where the fibers break, see Fig. 4-19.

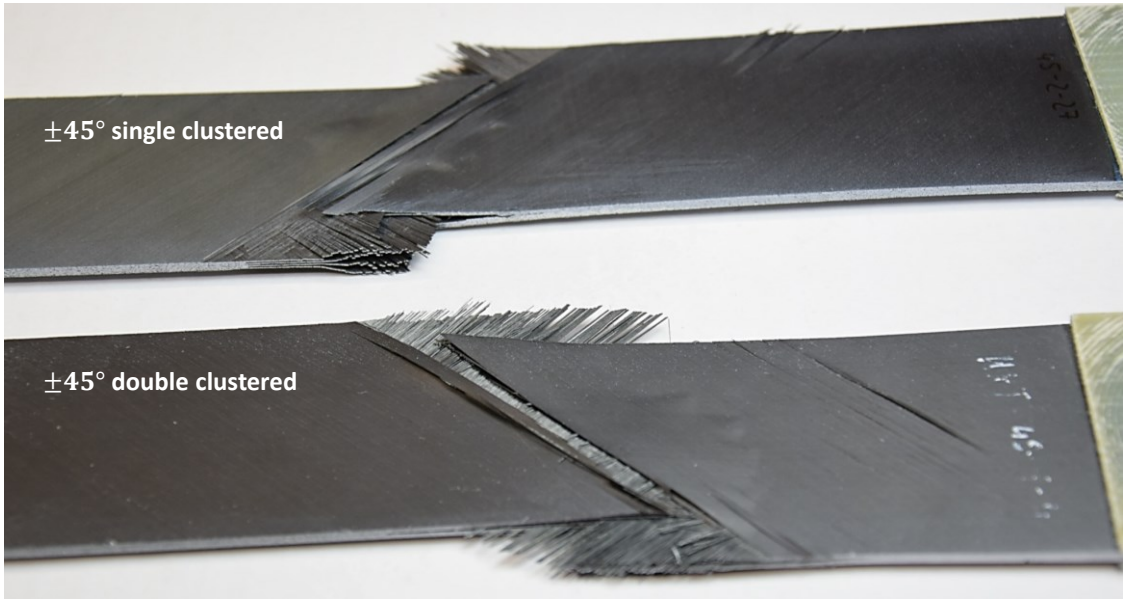

Fig. 4-19: Fracture surface of ±45° laminates

±50°-Laminates

Also for the $\pm 50°$ laminates only the fibers in half of the plies break, see Fig. 4-20. But here the fracture plane is not mandatory aligned to the fibers of the outer plies, as in the case of $\pm 40°$ and $\pm 45°$ laminates. The fracture plane of the double clustered specimen in Fig. 4-20 is oriented along the fibers of the mid-ply and not of the outer plies. This failed specimen additionally shows how the laminate failure mechanism proceeds. The $\pm 50°$ specimens already have a few inter-fiber cracks at the point of ultimate failure. At a critical point a delamination band arises through the specimens, where all interfaces between plies with different orientation fail. This delamination band arises suddenly and has a width of approximately 10mm and is orientated either +50° or -50°. For the $\pm 50°$ specimens a residual load capacity of 50% remains after ultimate laminate failure. During further loading, the specimen halves shear of along the delamination band, while the delamination at the specimen edges grows and the fibers bridging the crack fail one after another. The difference in strength between the single and double clustered specimens is low at 5.9%.

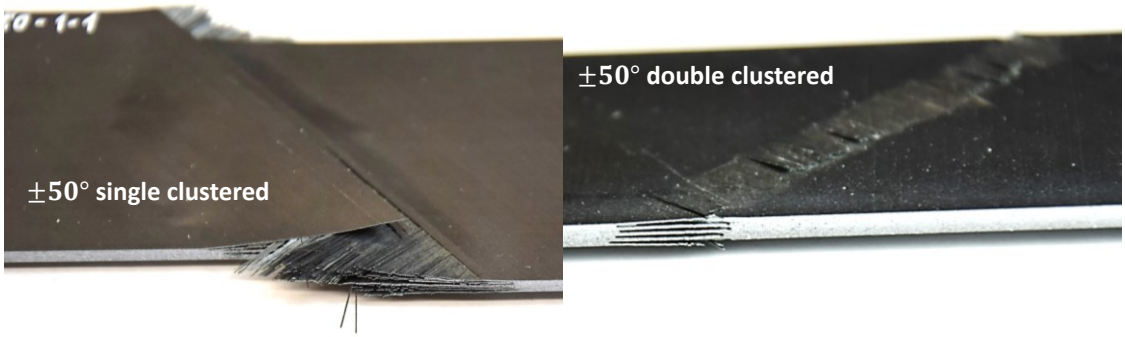

Fig. 4-20: Fracture surface of ±50° laminates

±60°-Laminates

In contrast to the ±50° laminates, the fracture plane of all ±60° specimens is orientated along the fibers of the outer plies. Thus only the fibers in half of the plies need to break. Another difference between ±50° and ±60° specimens is that there is only minor delamination observable for the ±60° specimens, see Fig. 4-21. For the double clustered specimens little delaminated triangles exist close to the specimen edge. Fiber breakage takes place in a small band close to the fracture plane, so only very short fiber bundles protrude out of the fracture surface. This is very interesting from the point of view that only approximately 40MPa are acting in fiber direction at the point of failure. The dissipated fracture energy seems to be very little even though the fibers in half of the plies break suddenly. The sound of the fracture is very slight in comparison to ±15° and ±30° specimens. The protruding fiber bundles are a bit coarser for the double clustered specimens compared to the single clustered ones. Also the profile depth of the fracture surface is bigger for the double clustered specimens. The difference in strength between the single clustered and double clustered specimens is at 9.8% for the ±60° laminates.

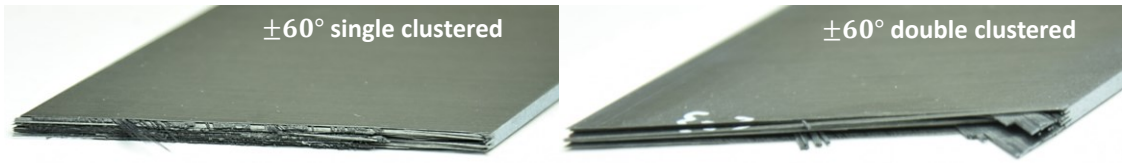

Fig. 4-21: Fracture surface of ±60° laminates

±75°-Laminates

The failure mechanism of the ±75° laminates is very similar to the failure behavior of the ±60° laminates. The only difference is that here also for the double clustered specimens no delaminated triangles at the specimen edge can be observed, see Fig. 4-21 and Fig. 4-22. The stress acting in fiber direction is approximately 7MPa at the point of failure. That is even smaller compared to the ±60° specimens. The difference in strength between single and double clustered specimens is relatively large at 14.1% in comparison to the other off-axis angles.

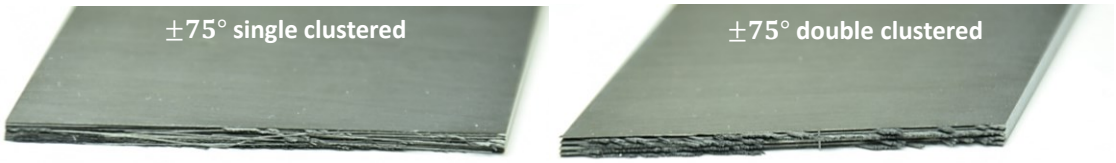

Fig. 4-22: Fracture surface of ±75° laminates

For all investigated angle-ply laminates, the fibers break, even though the fiber strength is by far not reached at any single ply. Furthermore, only very minor delamination can be detected at most of the specimens. To capture such laminate failure mechanisms in general, new ultimate laminate failure condition have to be developed. Stress states in the single plies, which are only achievable within a laminate, as well as local conditions at the free edges need to be subject of this study. Specimens without free edges (for example pipe specimens) could provide laminate strength data unaffected by the free edge effect and therefore clarify if the free edge is the driver for the specimen failure or if the laminate itself is not able to carry more load. Such investigations are most important for the $\pm 15°$ laminates as here neither inter-fiber failure nor fiber failure is predicted by classical failure criteria. The strength of such laminates is very interesting, as angle-ply layups with small off-axis angles make further weight reduction for many structural components possible [1].

As mentioned in Section 3.7, due to different thermal expansion coefficients of the fibers and the matrix material residual stresses occur during cooling down from cure temperature to ambient conditions. While the residual stresses of unidirectional reinforcement are already included in the strength values, in multi-directional laminates much higher internal stresses can exist because of the constraints between the plies of different orientation. Unfortunately, it is very difficult to estimate the correct quantity if this stresses. The problem to deal is that this stresses cannot be measured directly, but can only result from interpretation of deformations. In particular the strength of laminates where all plies are orientated with large off-axis angles is influenced by residual stresses.

Additional to new ultimate failure conditions for laminates, also new estimation approaches for the laminate fracture toughness are required to describe the failure behavior of arbitrary laminates. The fracture toughness is very important for the evaluation of stress concentrations.

Providing that some plies of the laminate are aligned in the main load direction, the model shows accurate results independent of the mesh size. Energy-based stiffness degradation laws limit the maximum element size, as the dissipated energy of cannot be smaller than the internal energy of the element at failure initiation. The laminate based formulation of the presented model allows in comparison to current ply-level approaches a larger maximum element size. For example the maximum element size for a quasi-isotropic layup is $l^*_{max} \approx 5.0$mm. But the major advantage of the proposed model is its

applicability in combination with layered shell elements. This enables the application of the presented model in combination with numerical efficient finite element models. As a result the proposed material model approach is not just suitable for academic applications like the simulation of coupon tests, but also for larger structural components.

5 Conclusion

A mechanism based nonlinear constitutive model for laminated composite structures is presented. The model accounts for often neglected mechanisms like deformation induced fiber reorientation and hydrostatic sensitivity of the epoxy matrix. As a consequence the model is able to predict the stiffness of laminates very accurate even at large deformations. In addition the number of required material parameters is kept as low as possible. As major benefit the mechanism based formulation provides a sound physical basis allowing for sensible results for arbitrary loading conditions and large deformations. The plasticity model has been formulated for three-dimensional stress states and can therefore be used to analyze complex loading conditions, as they appear at load introduction areas. The partly interactive plasticity model consist of two independent non-associative flow rules describing the yield processes due to transverse and longitudinal shear loading, respectively. For both flow mechanisms independent plastic master curves are required to describe the nonlinear response. The transverse hardening curve can be directly derived from a uniaxial transverse compression test. For the determination of the longitudinal shear hardening curve, a method for the experimental determination is presented. It has been shown that for low strains, the master curve can be obtained according to ASTM D 3518. For large deformations, a recalibration from $\pm 40°$ tension tests is proposed, as this allows an evaluation of the shear behavior without influences of additional damage effects. Beside both independent master curves only hydrostatic sensitivity parameters are required as material input. The impact of the parameters controlling hydrostatic sensitivity on the material response has been investigated by variation studies. Transverse and off-axis compression tests superimposed with various hydrostatic pressures have been used as experimental basis. Analyzes of angle-ply tension tests under atmospheric conditions showed, that considering hydrostatic sensitivity is not relevant to simulate their response. The reason therefore is the fact that neglecting hydrostatic sensitivity results in a different characterization of the material, which compensates its influence. Uniaxial tests with plane stress states are not suitable to derive the hydrostatic sensitivity parameters. Therefore, tests under high hydrostatic pressure are mandatory.

Beside fiber reorientation and plastic yielding, the constitutive behavior of laminates can be influenced by inter-fiber cracks. Initiation and progression of inter-fiber damage in a certain ply strongly depends on the ply thickness and the surrounding laminate. This is why strength values measured by unidirectional reinforced specimens are not accurate for the evaluation of embedded plies. A simple inter-fiber damage model is proposed considering the thickness of the damaged ply.

The model has been implemented as a user-defined subroutine *VUMAT* for the explicit FEA solver of *ABAQUS*. For a comprehensive validation, the model has been compared to conducted angle-ply tension and off-axis compression tests from the literature. Using the same material system offers the determination of a single material parameter set for the simulation of both test series. It became obvious, that the off-axis compression tests exclusively do not provide enough information to develop a robust nonlinear material model for fiber-reinforced composites. Two fundamentally different plasticity approaches from literature are both able to match the same series of unidirectional off-axis compression tests. For other stress states, for example a combination of in-plane shear and transverse tension, the models predict considerable different responses. To allow for an extended experimental bases for validation, angle-ply tension tests with the off-axis angles $\theta = 15°, 30°, 40°, 45°, 50°, 60°, 75°$ have been conducted. Also two different layups have been tested for each off-axis angle in order to investigate the influence of the ply thickness. On the one hand the plies were stacked alternating. On the other hand two plies of the same orientation were clustered together before chancing the fiber orientation. It was found out, that the ply thickness has only an influence on specimens where inter-fiber damage occurs. For the laminates where no inter-fiber cracks could be observed, the stress strain response of single and double clustered specimens was identical. But the double clustered specimens failed for all off-axis angles at a lower axial strain. While the strain varies extensively in the unidirectional specimen caused by local conditions, the strain in the angle-ply specimens is very homogeneous across the whole specimen expect for the load introduction areas outside the measuring range. A large width was chosen for the angle-ply specimens to minimize the influence of the free edges. A delamination driven failure mode has been avoided in this way.

Comparisons between the simulated and experimental observed material response show excellent correlation for all tested specimens even at large deformations up to 14% axial strain. The exact prediction of various different nonlinear stress–strain characteristics demonstrates the capability of the presented model. Due to the physical mechanism based formulation of the nonlinear constitutive model also for complex three-dimensional stress states reliable results can be assumed. The physical theory of the model is confirmed by very good agreement with experimental results. Therefore, the presented material model contributes to a better understanding of the material behavior of CFRPs.

The second part of the thesis deals with the numerical efficient modelling of ultimate laminate failure. A new continuum damage model approach for layered elements is presented. The main difference to current continuum damage models for CFRPs is, that separation of the laminate is defined on laminate-level and not on ply-level. In other words, after reaching the fiber strength in one ply, leading to ultimate laminate failure, not only the stiffness of the corresponding ply is reduced, but also the stiffness of the entire laminate. Thus, the model is in particular applicable in combination with layered elements, where the complete stacking is represented within one element. The

implementation of the presented approach requires access to all thickness integration points (in *ABAQUS*: section points) when analyzing the ply stresses. The model has been implemented for two-dimensional elements only, as *ABAQUS* provides no convenient interface for shell elements in combination with explicit time integration. The only possibility to implement the model approach for *ABAQUS explicit* is to program a user-defined element *VUEL*. For structural analyses usually layered shell element's discretization is used to minimize the computational effort. For validation, an experimental study of open-hole tension tests with various hole-diameters has been simulated. The laminate damage model shows excellent correlation to the experiments and provides mesh-size independent results for laminates containing fibers in main load direction. Moreover, very promising options to expand the model even further for arbitrary laminates and loading conditions are presented and discussed based on the failure behavior of the angle-ply tension tests.

6 Outlook

It takes a few steps to allow for the application of the proposed material model for composite laminates in the industrial environment. Firstly, the model needs to be implemented for layered shell elements for the application in commercial finite element solvers. Furthermore the failure behavior of composite laminates under bending has not been investigated satisfactory. But plate bending usually plays a subordinate role for shell-like laminated composite structures, as either double skin constructions or profiles be employed. For this reason, simple estimations are sufficient for the most application scenarios. At present laminates containing fibers oriented in main load direction are mostly used. For that case, the presented material model provides accurate and mesh-size independent results. Also the maximum allowed element size is coarse enough for industrial applications. To enable best possible efficiency for such laminates the laminate hardening model can be simplified or even reduced to pure linear elastic behavior. A generally valid material model is an ideal wish for sure, but not expedient for most applications, as the model becomes very expensive and complex. Also the experimental characterization of the required material properties becomes correspondingly a great deal of work. According to the scope of application the complexity of the material model should be customized for a sensible and efficient analysis.

In my opinion the most urgent demand for research is in the field of ultimate laminate failure of laminates, where no fibers are aligned in load direction. The use of angle-ply layups with a small off-axis angle, for example $\pm 10°$, makes a further weight reduction for many structural components possible [1]. The most serious problem here is that current failure criteria for fiber reinforced composites are not able to predict the strength of such laminates correctly. The laminate hardening model given in the present thesis is able to simulate the laminate stiffness very accurate and to provide the stress states in the unique plies precise. On this basis, appearing ultimate failure mechanisms can be studied numerically and experimentally. The role of the free edges is a central issue for that study. New ultimate laminate failure conditions would be the ideal outcome of such investigations. As a result the applicability of the proposed laminate model would be extended for more general laminates, where fibers in load direction are not mandatory.

A Appendix

Table A-1: Position of the Gauss integration points within one ply

	Number of Gauss Integration Points for each Ply				
	1	2	3	4	5
$z_{k,1}$	z_k	$z_k - \sqrt{\frac{1}{3}}\frac{t_k}{2}$	$z_k - \sqrt{\frac{3}{5}}\frac{t_k}{2}$	$z_k - \sqrt{\frac{3}{7}+\frac{2}{7}\sqrt{\frac{6}{5}}}\frac{t_k}{2}$	$z_k - \frac{1}{3}\sqrt{5+2\sqrt{\frac{10}{7}}}\frac{t_k}{2}$
$z_{k,2}$	-	$z_k + \sqrt{\frac{1}{3}}\frac{t_k}{2}$	z_k	$z_k - \sqrt{\frac{3}{7}-\frac{2}{7}\sqrt{\frac{6}{5}}}\frac{t_k}{2}$	$z_k - \frac{1}{3}\sqrt{5-2\sqrt{\frac{10}{7}}}\frac{t_k}{2}$
$z_{k,3}$	-	-	$z_k + \sqrt{\frac{3}{5}}\frac{t_k}{2}$	$z_k + \sqrt{\frac{3}{7}-\frac{2}{7}\sqrt{\frac{6}{5}}}\frac{t_k}{2}$	z_k
$z_{k,4}$	-	-	-	$z_k + \sqrt{\frac{3}{7}+\frac{2}{7}\sqrt{\frac{6}{5}}}\frac{t_k}{2}$	$z_k + \frac{1}{3}\sqrt{5-2\sqrt{\frac{10}{7}}}\frac{t_k}{2}$
$z_{k,5}$	-	-	-	-	$z_k + \frac{1}{3}\sqrt{5+2\sqrt{\frac{10}{7}}}\frac{t_k}{2}$

Table A-2: Related thickness for each Gauss integration point within one ply

	Number of Gauss Integration Points for each Ply				
	1	2	3	4	5
$t_{k,1}$	t_k	$\frac{1}{2}t_k$	$\frac{5}{18}t_k$	$\frac{18-\sqrt{30}}{72}t_k$	$\frac{322-13\sqrt{70}}{1800}t_k$
$t_{k,2}$	-	$\frac{1}{2}t_k$	$\frac{8}{18}t_k$	$\frac{18+\sqrt{30}}{72}t_k$	$\frac{322+13\sqrt{70}}{1800}t_k$
$t_{k,3}$	-	-	$\frac{5}{18}t_k$	$\frac{18+\sqrt{30}}{72}t_k$	$\frac{64}{225}t_k$
$t_{k,4}$	-	-	-	$\frac{18-\sqrt{30}}{72}t_k$	$\frac{322+13\sqrt{70}}{1800}t_k$
$t_{k,5}$	-	-	-	-	$\frac{322-13\sqrt{70}}{1800}t_k$

Table A-3: Experimental results of unidirectional fiber tension tests for IM7-8552

	Longitudinal Tensile Strength $R_{\parallel}^{t}$
Specimen 1	2597.56 MPa
Specimen 2	2452.61 MPa
Specimen 3	2517.28 MPa
Specimen 4	2744.69 MPa
Specimen 5	2438.58 MPa
Mean	**2550.14 MPa**
STDV	112.37 MPa
CV	4.406 %

B List of Tables

C List of Figures

D Publications

Journal Papers

[P1] U. Mandel, R. Taubert, R. Hinterhölzl, “Mechanism based nonlinear constitutive model for composite laminates subjected to large deformations”, *Composite Structures*, vol. 132, pp. 98–108, 2015.

[P2] U. Mandel, R. Taubert, R. Hinterhölzl, “Laminate damage model for composite structures”, *Composite Structures*, vol. 136, pp. 441–449, 2016.

[P3] U. Mandel, R. Taubert, R. Hinterhölzl, “Three-dimensional nonlinear constitutive model for composites”, *Composite Structures*, vol. 142, pp. 78–86, 2016.

[P4] R. Taubert, U. Mandel, R. Hinterhölzl, “Study of layup influences on the nonlinear behavior of composites by evaluation of ply stiffness reduction”, *Composites Part A: Applied Science and Manufacturing*, vol. 79, pp. 63–73, 2015.

[P5] R. Taubert, U. Mandel, R. Hinterhölzl, “Influence of nonlinear material behavior on the effect of inter-fiber cracks in composite laminates”, *Journal of Composite Materials*, accepted for publication, 2016.

[P6] A. Altmann, R. Taubert, U. Mandel, R. Hinterhölzl, and K. Drechsler, “A continuum damage model to predict the influence of ply waviness on stiffness and strength in ultra-thick unidirectional Fiber-reinforced Plastics”, *Journal of Composite Materials*, vol. 50, pp. 2739-2755, 2016.

Conference Papers

[C1] U. Mandel, R. Taubert, R. Hinterhölzl, “Laminate damage model for CFRP structures”, ICCST/10 – 10th International Conference on Composite Science and Technology, Lisbon, 2015.

[C2] U. Mandel, R. Taubert, R. Hinterhölzl, “A continuum damage approach for an efficient ultimate failure analysis with layered shell elements” 5th ECCOMAS Thematic Conference on Material Response of Composites, Bristol, 2015.

[C3] U. Mandel, R. Taubert, R. Hinterhölzl, “Mechanical behavior of angle-ply laminates” ECCM17 – 17th European Conference on Composite Materials, Munich, 2016.

[C4] R. Taubert, U. Mandel, R. Hinterhölzl, “Influence of the stacking sequence on the nonlinear behavior of composite laminates related to large deformations”, ICCST/10 – 10th International Conference on Composite Science and Technology, Lisbon, 2015.

E Supervised student theses

[S1] N. Hofheinz, „Entwicklung von laminaren Flügelnasenübergängen im Flugzeugbau“, diploma thesis in cooperation with EADS Innovation Works, Lehrstuhl für Carbon Composites, TUM, 2013.

[S2] A. Reinbold, „Untersuchung von Einflussgrößen vibrationsgefügter CFK-Thermoplast-Verbindungen“, diploma thesis in cooperation with BMW, Lehrstuhl für Carbon Composites, TUM, 2013.

[S3] M. Holzinger, „Krafteinleitung in FVK-Strukturen – Analyse von Patenten“, semester thesis in cooperation with BMW, Lehrstuhl für Carbon Composites, TUM, 2013.

[S4] J. Assenbrunner, „Integration einer CAE-Prozesskette zur Herstellung von Fahrwerkskomponenten am Beispiel eines CFK-Achsträgers“, diploma thesis in cooperation with BMW, Lehrstuhl für Carbon Composites, TUM, 2013.

[S5] F. Wilke, „Simulation von UD-Materialverhalten an Einheitszellen mit stochastischer Faserverteilung“, diploma thesis, Hochschule München, 2014.

[S6] T. Schulz, „Gestaltung lokal hochbelasteter Krafteinleitungsbereiche von endloskohlenstofffaserverstärkten Fahrzeugstrukturen“, diploma thesis in cooperation with BMW, Lehrstuhl für Carbon Composites, TUM, 2014.

[S7] M. Volk, „Konstruktion einer Ablegevorrichtung für Faserverbundlaminate“, bachelor thesis, Lehrstuhl für Carbon Composites, TUM, 2014.

[S8] J. Niemeyer, „Untersuchung von in-situ Schadensprogression in Composite Laminaten anhand von RVE Studien“, diploma thesis, Lehrstuhl für Carbon Composites, TUM, 2014.

[S9] M. Holzinger, „Entwicklung von Lasteinleitungselementen in CFK-Sandwichstrukturen“, master thesis in cooperation with BMW, Lehrstuhl für Carbon Composites, TUM, 2014.

[S10] L. Häberle, „Implementierung eines 4-kontigen Schalenelements in Abaqus“, master thesis, Lehrstuhl für Carbon Composites, TUM, 2014.

[S11] C. Dannenberg, „Untersuchung von in-situ Schadensinitiierung in Composite Laminaten anhand von RVE Studien“, semester thesis, Lehrstuhl für Carbon Composites, TUM, 2014.

[S12] L. Böck, „Bestimmung der charakteristischen Elementlänge in der Kontinuumsschädigungsmechanik“, diploma thesis, Lehrstuhl für Carbon Composites, TUM, 2015.

[S13] A. Uhl, „Erstellung mikromechanischer FE-Modelle zur Untersuchung des Materialverhaltens von Composite Laminaten“, semester thesis, Lehrstuhl für Carbon Composites, TUM, 2015.

[S14] M. Reil, „Hierarchical Evaluation of CFRP Strength and Failure Models“, master thesis in cooperation with BMW, Lehrstuhl für Carbon Composites, TUM, 2015.

[S15] N. Fischer, “Prozessoptimierung zur Herstellung von Krafteinleitungen in CFK-Strukturen”, master thesis in cooperation with BMW, Lehrstuhl für Carbon Composites, TUM, 2016.

[S16] M. Süß, “Analytische Auslegung und numerische Simulation einer Faserverbundstruktur für ein Wellenkraftwerk” ”, master thesis in cooperation with SINNPower, Lehrstuhl für Carbon Composites, TUM, 2016.

[S17] H. Weidinger, “FPP-Überlappungsmuster – Aufbau eines Simulationsframeworks und geometriebasierte Optimierung”, master thesis in cooperation with Cevotec, Lehrstuhl für Carbon Composites, TUM, 2016.

[S18] D. Schneider, “Nummerischer Vergleich verschiedener Slat Bauweisen hinsichtlich Vogelschlag Anforderungen”, master thesis in cooperation with Airbus Group Innovations, Lehrstuhl für Carbon Composites, TUM, 2016.

References

[1] S. W. Tsai and J. D. D. Melo, Composite materials design and testing: *Unlocking mystery with invariants*. Stanford: Stanford Aeronautics & Astronautics; JEC Group, 2015.

[2] Broken Cervelo C2P Fork. Available: https://www.flickr.com/photos/cjscott69/2353625026/in/photostream/.

[3] C. Schuecker and H. E. Pettermann, "A continuum damage model for fiber reinforced laminates based on ply failure mechanisms", *Composite Structures*, vol. 76, no. 1-2, pp. 162–173, 2006.

[4] A. Puck and H. Schürmann, "Failure analysis of FRP laminates by means of physically based phenomenological models", *Composites Science and Technology*, vol. 62, no. 12-13, pp. 1633–1662, 2002.

[5] A. Matzenmiller, J. Lubliner and R. L. Taylor, "A constitutive model for anisotropic damage in fiber-composites", *Mechanics of Materials*, vol. 20, no. 2, pp. 125–152, 1995.

[6] J. F. Maire and J. L. Chaboche, "A new formulation of continuum damage mechanics (CDM) for composite materials", *Aerospace Science and Technology*, vol. 1, no. 4, pp. 247–257, 1997.

[7] P. Maimí, P. P. Camanho, J. A. Mayugo and C. G. Dávila, "A continuum damage model for composite laminates: Part I – Constitutive model", *Mechanics of Materials*, vol. 39, no. 10, pp. 897–908, 2007.

[8] P. Maimí, P. P. Camanho, C. G. Dávila and J. A. Mayugo, "A continuum damage model for composite laminates: Part II – Computational implementation and validation", *Mechanics of Materials*, vol. 39, no. 10, pp. 909–919, 2007.

[9] P. Maimí, J. A. Mayugo and P. P. Camanho, "A Three-dimensional Damage Model for Transversely Isotropic Composite Laminates", *Journal of Composite Materials*, vol. 42, no. 25, pp. 2717–2745, 2008.

[10] I. Lapczyk and J. A. Hurtado, "Progressive damage modeling in fiber-reinforced materials", *Composites Part A: Applied Science and Manufacturing*, vol. 38, no. 11, pp. 2333–2341, 2007.

[11] P. Ladevèze, "A damage computational method for composite structures", *Computers & Structures*, vol. 44, no. 1-2, pp. 79–87, 1992.

[12] E. J. Barbero and L. D. E. Vivo, "A Constitutive Model for Elastic Damage in Fiber-Reinforced PMC Laminae", *International Journal of Damage Mechanics*, vol. 10, no. 1, pp. 73–93, 2001.

[13] M. V. Donadon, L. Iannucci, B. G. Falzon, J. M. Hodgkinson and S. de Almeida, “A progressive failure model for composite laminates subjected to low velocity impact damage”, *Computers & Structures*, vol. 86, no. 11-12, pp. 1232–1252, 2008.

[14] T. Flatscher, “A Constitutive Model for the Elasto-Plasto-Damage Ply behavior in Laminated FRP Composites - Its Development, Implementation and Application in FEM Simulations” Phd Thesis, Universität Wien, 2010.

[15] G. Ernst, M. Vogler, C. Hühne and R. Rolfes, “Multiscale progressive failure analysis of textile composites”, *Composites Science and Technology*, vol. 70, no. 1, pp. 61–72, 2010.

[16] J. Zangenberg and P. Brøndsted, “Quantitative study on the statistical properties of fibre architecture of genuine and numerical composite microstructures”, *Composites Part A: Applied Science and Manufacturing*, vol. 47, pp. 124–134, 2013.

[17] M. Romanowicz, “Progressive failure analysis of unidirectional fiber-reinforced polymers with inhomogeneous interphase and randomly distributed fibers under transverse tensile loading”, *Composites Part A: Applied Science and Manufacturing*, vol. 41, no. 12, pp. 1829–1838, 2010.

[18] T. J. Vaughan and C. T. McCarthy, “Micromechanical modelling of the transverse damage behaviour in fibre reinforced composites”, *Composites Science and Technology*, vol. 71, no. 3, pp. 388–396, 2011.

[19] A. Arteiro, G. Catalanotti, A. R. Melro, P. Linde and P. P. Camanho, “Micro-mechanical analysis of the effect of ply thickness on the transverse compressive strength of polymer composites”, *Composites Part A: Applied Science and Manufacturing*, vol. 79, pp. 127–137, 2015.

[20] R. P. Tavares, A. R. Melro, M. A. Bessa, A. Turon, W. K. Liu and P. P. Camanho, “Mechanics of hybrid polymer composites: analytical and computational study”, *Computational Mechanics*, vol. 57, no. 3, pp. 405–421.

[21] A. C. Hansen and M. R. Garnich, “A multicontinuum theory for structural analysis of composite material systems”, *Composites Engineering*, vol. 5, no. 9, pp. 1091–1103, 1995.

[22] J. Mayes and A. C. Hansen, “Composite laminate failure analysis using multicontinuum theory”, *Composites Science and Technology*, vol. 64, no. 3-4, pp. 379–394, 2004.

[23] B. M. Zhang and L. Zhao, “Progressive Damage and Failure Modeling in Fiber-Reinforced Laminated Composites Containing a Hole”, *International Journal of Damage Mechanics*, vol. 21, no. 6, pp. 893–911, 2012.

[24] J. Llorca, C. Gonzalez, J. M. Molina-Aldareguia, J. Segurado, R. Seltzer, F. Sket, M. Rodriguez, S. Sadaba, R. Munoz and L. P. Canal, “Multiscale modeling of composite materials: a roadmap towards virtual testing”, *Advanced materials (Deerfield Beach, Fla.)*, vol. 23, no. 44, pp. 5130–5147, 2011.

[25] S. W. Tsai and E. M. Wu, “A General Theory of Strength for Anisotropic Materials”, *Journal of Composite Materials*, vol. 5, no. 1, pp. 58–80, 1971.

[26] Z. Hashin, “Failure Criteria for Unidirectional Fiber Composites”, *Journal of Applied Mechanics*, vol. 47, no. 2, p. 329, 1980.

[27] A. Puck, “Failure Analysis of FRP Laminates by means of Physically Based Phenomenological Models”, *Composites Science and Technology*, vol. 58, no. 7, pp. 1045–1067, 1998.

[28] R. G. Cuntze and A. Freund, “The predictive capability of failure mode concept-based strength criteria for multidirectional laminates”, *Composites Science and Technology*, vol. 64, no. 3-4, pp. 343–377, 2004.

[29] C. G. Dávila, “Failure Criteria for FRP Laminates”, *Journal of Composite Materials*, vol. 39, no. 4, pp. 323–345, 2005.

[30] S. T. Pinho, R. Darvizeh, P. Robinson, C. Schuecker and P. Camanho, “Material and structural response of polymer-matrix fibre-reinforced composites”, *Journal of Composite Materials*, vol. 46, no. 19-20, pp. 2313–2341, 2012.

[31] Z. P. Bažant and B. H. Oh, “Crack band theory for fracture of concrete”, *Matériaux et Construction*, vol. 16, no. 3, pp. 155–177.

[32] U. Mandel, R. Taubert and R. Hinterhölzl, “Mechanism based nonlinear constitutive model for composite laminates subjected to large deformations”, *Composite Structures*, vol. 132, pp. 98–108, 2015.

[33] U. Mandel, R. Taubert and R. Hinterhoelzl, “Three-dimensional nonlinear constitutive model for composites”, *Composite Structures*, vol. 142, pp. 78–86, 2016.

[34] E. Kontou, “Viscoplastic deformation of an epoxy resin at elevated temperatures”, *Journal of Applied Polymer Science*, vol. 101, no. 3, pp. 2027–2033, 2006.

[35] B. R. Mauget, L. Minnetyan and C. C. Chamis, “Large deformation nonlinear response of soft composite structures via laminate analogy”, *Journal of advanced materials*, vol. 33, no. 2, pp. 21–26, 2001.

[36] C. Herakovich, “Damage evolution in [±45]s laminates with fiber rotation”, *Composites Science and Technology*, vol. 60, no. 15, pp. 2781–2789, 2000.

[37] J. D. Fuller and M. R. Wisnom, “Pseudo-ductility and damage suppression in thin ply CFRP angle-ply laminates”, *Composites Part A: Applied Science and Manufacturing*, vol. 69, pp. 64–71, 2015.

[38] C. Sun, “The effect of deformation-induced change of fiber orientation on the non-linear behavior of polymeric composite laminates”, *Composites Science and Technology*, vol. 60, no. 12-13, pp. 2337–2345, 2000.

[39] Test Method for In-Plane Shear Response of Polymer Matrix Composite Materials by Tensile Test of a 45 Laminate, ASTM D3518_D3518M.

[40] I. Djordjevic, D. Sekulic and M. Stevanovic, “Non-linear elastic behavior of carbon fibres of different structural and mechanical characteristic”, *Journal of the Serbian Chemical Society*, vol. 72, no. 5, pp. 513–521, 2007.

[41] W. van Dreumel and J. Kamp, Non Hookean behaviour in the fibre direction of carbon-fibre composites and the influence of fibre waviness on the tensile properties: Delft University of Technology.

[42] T. B. Stecenko and M. M. Stevanovi, “Variation of Elastic Moduli with Strain in Carbon/Epoxy Laminates”, *Journal of Composite Materials*, vol. 24, no. 11, pp. 1152–1158, 1990.

[43] G. J. Curtis, J. M. Milne and W. N. Reynolds, “Non-Hookean Behaviour of Strong Carbon Fibres”, *Nature*, vol. 220, no. 5171, pp. 1024–1025, 1968.

[44] M. S. Madhukar and L. T. Drzal, “Fiber-Matrix Adhesion and Its Effect on Composite Mechanical Properties: II. Longitudinal (0°) and Transverse (90°) Tensile and Flexure Behavior of Graphite/Epoxy Composites”, *Journal of Composite Materials*, vol. 25, no. 8, pp. 958–991, 1991.

[45] R. Hill, The Mathematical Theory of Plasticity: Clarendon Press, 1998.

[46] O. Y. Drucker and C. Prager, “Soil mechanics and plastic analysis of limit design”, *Quarterly Applied Math*, vol. 10, pp. 157–164.

[47] M. Xie, “A plasticity model for unidirectional composite materials and its applications in modeling composites testing”, *Composites Science and Technology*, vol. 54, no. 1, pp. 11–21, 1995.

[48] C. T. Sun and J. L. Chen, “A Simple Flow Rule for Characterizing Nonlinear Behavior of Fiber Composites”, *Journal of Composite Materials*, vol. 23, no. 10, pp. 1009–1020, 1989.

[49] H. Koerber, “Mechanical Response of Advanced Composites under High Strain Rates” Phd Thesis, Universidade do Porto, 2010.

[50] J. P. Boehler, Yielding and Failure of Transversely Isotropic Solids: Springer Vienna.

[51] A. J. M. Spencer, Constitutive Theory for Strongly Anisotropic Solids: Springer Vienna.

[52] M. Vogler, R. Rolfes and P. P. Camanho, “Modeling the inelastic deformation and fracture of polymer composites – Part I: Plasticity model”, *Mechanics of Materials*, vol. 59, pp. 50–64, 2013.

[53] R. Raghava, R. M. Caddell and G. S. Y. Yeh, “The macroscopic yield behaviour of polymers”, *Journal of Materials Science*, vol. 8, no. 2, pp. 225–232.

[54] G. M. Vyas, S. T. Pinho and P. Robinson, “Constitutive modelling of fibre-reinforced composites with unidirectional plies using a plasticity-based approach”, *Composites Science and Technology*, vol. 71, no. 8, pp. 1068–1074, 2011.

[55] E. S. Shin and K. D. Pae, “Effects of Hydrostatic Pressure on In-Plane Shear Properties of Graphite/Epoxy Composites”, *Journal of Composite Materials*, vol. 26, no. 6, pp. 828–868, 1992.

[56] S. R. Swanson, M. J. Messick and Z. Tian, “Failure of Carbon/Epoxy Lamina Under Combined Stress”, *Journal of Composite Materials*, vol. 21, no. 7, pp. 619–630, 1987.

[57] T. Flatscher and H. E. Pettermann, “A constitutive model for fiber-reinforced polymer plies accounting for plasticity and brittle damage including softening – Implementation for implicit FEM”, *Composite Structures*, vol. 93, no. 9, pp. 2241–2249, 2011.

[58] R. Olsson, “A survey of test methods for multiaxial and out-of-plane strength of composite laminates”, *Composites Science and Technology*, vol. 71, no. 6, pp. 773–783, 2011.

[59] T. Vogler and S. Kyriakides, “Inelastic behavior of an AS4/PEEK composite under combined transverse compression and shear. Part I: Experiments”, *International Journal of Plasticity*, vol. 15, no. 8, pp. 783–806, 1999.

[60] H. Koerber, J. Xavier and P. P. Camanho, “High strain rate characterization of unidirectional carbon-epoxy IM7-8552 in transverse compression and in-plane shear using digital image correlation”, *Mechanics of Materials*, vol. 42, no. 11, pp. 1004–1019, 2010.

[61] S.-C. Hung and K. M. Liechti, “Nonlinear Multiaxial Behavior and Failure of Fiber-Reinforced Composites” in *STP*, vol. 1357, *Time dependent and nonlinear effects in polymers and composites*, R. A. Schapery and C. T. Sun, Eds, W. Conshocken, Pa.: ASTM, 2000, 176-176-47.

[62] Test Method for Compressive Properties of Rigid Plastics, ASTM D0695-15, 2015.

[63] C. P. R. Hoppel, T. A. Bogetti and J. W. Gillespie, “Literature Review-Effects of Hydrostatic Pressure on the Mechanical Behavior of Composite Materials”, *Journal of Thermoplastic Composite Materials*, vol. 8, no. 4, pp. 375–409, 1995.

[64] K. D. Pae and K. Y. Rhee, “Effects of hydrostatic pressure on the compressive behavior of thick laminated 45 ° and 90 ° unidirectional graphite-fiber/epoxy-matrix composites”, *Composites Science and Technology*, vol. 53, no. 3, pp. 281–287, 1995.

[65] J. Zhang, N. Kikuchi, V. Li, A. Yee and G. Nusholtz, “Constitutive modeling of polymeric foam material subjected to dynamic crash loading”, *International Journal of Impact Engineering*, vol. 21, no. 5, pp. 369–386, 1998.

[66] I. I. Gol'denblat and V. A. Kopnov, “Strength of glass-reinforced plastics in the complex stress state”, *Polymer Mechanics*, vol. 1, no. 2, pp. 54–59.

[67] O. Mohr, “Welche Umstände bedingen die Elastizitätsgrenze und den Bruch eines Materials?”, *VDI 24, 45: 1524-1530 and 46: 1572-1577*, 1900.

[68] A. Puck, Festigkeitsanalyse von Faser-Matrix-Laminaten: *Modelle für die Praxis*. München, Wien: Hanser, 1996.

[69] R. G. Cuntze, “The predictive capability of failure mode concept-based strength criteria for multi-directional laminates—part B”, *Composites Science and Technology*, vol. 64, no. 3-4, pp. 487–516, 2004.

[70] M. Knops, Analysis of failure in fiber polymer laminates: *The theory of Alfred Puck*. Berlin, New York: Springer, 2008.

[71] K. W. Garrett and J. E. Bailey, “Multiple transverse fracture in 90° cross-ply laminates of a glass fibre-reinforced polyester”, *Journal of Materials Science*, vol. 12, no. 1, pp. 157–168.

[72] D. L. Flaggs and M. H. Kural, “Experimental Determination of the In Situ Transverse Lamina Strength in Graphite/Epoxy Laminates”, *Journal of Composite Materials*, vol. 16, no. 2, pp. 103–116, 1982.

[73] A. Wang and F. W. Crossman, “Initiation and Growth of Transverse Cracks and Edge Delamination in Composite Laminates Part 1. An Energy Method”, *Journal of Composite Materials*, vol. 14, no. 1, pp. 71–87, 1980.

[74] F. W. Crossman, W. J. Warren, A. Wang and G. E. Law, “Initiation and Growth of Transverse Cracks and Edge Delamination in Composite Laminates Part 2. Experimental Correlation”, *Journal of Composite Materials*, vol. 14, no. 1, pp. 88–108, 1980.

[75] F.-K. Chang and M.-H. Chen, “The In Situ Ply Shear Strength Distributions in Graphite/Epoxy Laminated Composites”, *Journal of Composite Materials*, vol. 21, no. 8, pp. 708–733, 1987.

[76] S. E. Groves, C. E. Harris, A. L. Highsmith, D. H. Allen and R. G. Norvell, “An experimental and analytical treatment of matrix cracking in cross-ply laminates”, *Experimental Mechanics*, vol. 27, no. 1, pp. 73–79.

[77] L. Boniface, P. A. Smith, M. G. Bader and A. H. Rezaifard, “Transverse Ply Cracking in Cross-Ply CFRP Laminates--Initiation or Propagation Controlled?”, *Journal of Composite Materials*, vol. 31, no. 11, pp. 1080–1112, 1997.

[78] T. A. Sebaey, J. Costa, P. Maimí, Y. Batista, N. Blanco and J. A. Mayugo, “Measurement of the in situ transverse tensile strength of composite plies by means of the real time monitoring of microcracking”, *Composites Part B: Engineering*, vol. 65, pp. 40–46, 2014.

[79] G. J. Dvorak and N. Laws, “Analysis of Progressive Matrix Cracking In Composite Laminates II. First Ply Failure”, *Journal of Composite Materials*, vol. 21, no. 4, pp. 309–329, 1987.

[80] P. P. Camanho, C. G. Dávila, S. T. Pinho, L. Iannucci and P. Robinson, “Prediction of in situ strengths and matrix cracking in composites under transverse tension and in-plane shear”, *Composites Part A: Applied Science and Manufacturing*, vol. 37, no. 2, pp. 165–176, 2006.

[81] G. Catalanotti, P. P. Camanho and A. T. Marques, “Three-dimensional failure criteria for fiber-reinforced laminates”, *Composite Structures*, vol. 95, pp. 63–79, 2013.

[82] R. Taubert, U. Mandel and R. Hinterhoelzl, “Influence of nonlinear material behavior on the effect of inter-fiber cracks in composite laminates”, *Journal of Composite Materials*, accepted for publication, 2016.

[83] W. K. Goertzen and M. R. Kessler, “Creep behavior of carbon fiber/epoxy matrix composites”, *Materials Science and Engineering: A*, vol. 421, no. 1-2, pp. 217–225, 2006.

[84] M. Katouzian, O. S. Bruller and A. Horoschenkoff, “On the Effect of Temperature on the Creep Behavior of Neat and Carbon Fiber Reinforced PEEK and Epoxy Resin”, *Journal of Composite Materials*, vol. 29, no. 3, pp. 372–387, 1995.

[85] G. C. Papanicolaou, S. P. Zaoutsos and E. A. Kontou, “Fiber orientation dependence of continuous carbon/epoxy composites nonlinear viscoelastic behavior”, *Composites Science and Technology*, vol. 64, no. 16, pp. 2535–2545, 2004.

[86] J. Raghavan and M. Meshii, “Creep of polymer composites”, *Composites Science and Technology*, vol. 57, no. 12, pp. 1673–1688, 1998.

[87] R. Taubert, U. Mandel and R. Hinterhölzl, “Study of layup influences on the nonlinear behavior of composites by evaluation of ply stiffness reduction”, *Composites Part A: Applied Science and Manufacturing*, vol. 79, pp. 63–73, 2015.

[88] K. B. Pettersson, J. M. Neumeister, E. Kristofer Gamstedt and H. Öberg, “Stiffness reduction, creep, and irreversible strains in fiber composites tested in repeated interlaminar shear”, *Composite Structures*, vol. 76, no. 1-2, pp. 151–161, 2006.

[89] K. Chung and H. Ryou, “Development of viscoelastic/rate-sensitive-plastic constitutive law for fiber-reinforced composites and its applications. Part I: Theory and material characterization”, *Composites Science and Technology*, vol. 69, no. 2, pp. 284–291, 2009.

[90] T. K. Obrien and R. Krueger, “Analysis of ninety degree flexure tests for characterization of composite transverse tensile strength”, 2001.

[91] A. Kaddour, M. Hinton, P. Smith and S. Li, “Mechanical properties and details of composite laminates for the test cases used in the third world-wide failure exercise”, *Journal of Composite Materials*, vol. 47, no. 20-21, pp. 2427–2442, 2013.

[92] Test Method for Tensile Properties of Polymer Matrix Composite Materials, ASTM D3039_D3039M-14, 2014.

[93] W. O. Winer, “Molybdenum disulfide as a lubricant: A review of the fundamental knowledge”, *Wear*, vol. 10, no. 6, pp. 422–452, 1967.

[94] K. D. Cowley and P. W. Beaumont, “The measurement and prediction of residual stresses in carbon-fibre/polymer composites”, *Composites Science and Technology*, vol. 57, no. 11, pp. 1445–1455, 1997.

[95] Du Chen, S. Cheng and T. D. Gerhardt, “Thermal stresses in laminated beams”, *Journal of Thermal Stresses*, vol. 5, no. 1, pp. 67–84, 2007.

[96] N. Ersoy and O. Vardar, “Measurement of Residual Stresses in Layered Composites by Compliance Method”, *Journal of Composite Materials*, vol. 34, no. 7, pp. 575–598, 2000.

[97] H. T. Hahn and N. J. Pagano, “Curing Stresses in Composite Laminates”, *Journal of Composite Materials*, vol. 9, no. 1, pp. 91–106, 1975.

[98] N. N. Huang and T. R. Tauchert, “Thermal stresses in doubly-curved cross-ply laminates”, *International Journal of Solids and Structures*, vol. 29, no. 8, pp. 991–1000, 1992.

[99] A. A. Khdeir and J. N. Reddy, “Thermal stresses and deflections of cross-ply laminated plates using refined plate therories”, *Journal of Thermal Stresses*, vol. 14, no. 4, pp. 419–438, 1991.

[100] R. Rolfes, A. K. Noor and H. Sparr, “Evaluation of transverse thermal stresses in composite plates based on first-order shear deformation theory”, *Computer Methods in Applied Mechanics and Engineering*, vol. 167, no. 3-4, pp. 355–368, 1998.

[101] M. Savoia and J. N. Reddy, “Three-dimensional thermal analysis of laminated composite plates”, *International Journal of Solids and Structures*, vol. 32, no. 5, pp. 593–608, 1995.

[102] T. R. Tauchert, “Thermal Buckling of Thick Antisymmetric Angle-Ply Laminates”, *Journal of Thermal Stresses*, vol. 10, no. 2, pp. 113–124, 1987.

[103] V. B. Tungikar and K. M. Rao, “Three dimensional exact solution of thermal stresses in rectangular composite laminate”, *Composite Structures*, vol. 27, no. 4, pp. 419–430, 1994.

[104] J. Webber and S. Morton, “An analytical solution for the thermal stresses at the free edges of laminated plates”, *Composites Science and Technology*, vol. 46, no. 2, pp. 175–185, 1993.

[105] Y. Weitsman, “Residual Thermal Stresses Due to Cool-Down of Epoxy-Resin Composites”, *Journal of Applied Mechanics*, vol. 46, no. 3, p. 563, 1979.

[106] W.-L. Yin, “Thermal Stresses and Free-Edge Effects in Laminated Beams: A Variational Approach Using Stress Functions”, *Journal of Electronic Packaging*, vol. 113, no. 1, p. 68, 1991.

[107] A. Altmann, R. Taubert, U. Mandel, R. Hinterhoelzl and K. Drechsler, “A continuum damage model to predict the influence of ply waviness on stiffness and strength in ultra-thick unidirectional Fiber-reinforced Plastics”, *Journal of Composite Materials*, 2015.

[108] D. H. Allen, S. E. Groves and C. E. Harris, “A Cumulative Damage Model for Continuous Fiber Composite Laminates with Matrix Cracking and Interply Delaminations” in *ASTM special technical publication*, vol. 972, *Composite materials: Testing and design (eighth conference)*, J. D. Whitcomb, Ed, Philadelphia, Pa. (1916 Race St, Philadelphia 19103): ASTM, 1988, 57-57-24.

[109] P. P. Camanho, M. A. Bessa, G. Catalanotti, M. Vogler and R. Rolfes, “Modeling the inelastic deformation and fracture of polymer composites – Part II: Smeared crack model”, *Mechanics of Materials*, vol. 59, pp. 36–49, 2013.

[110] P. P. Camanho, P. Maimí and C. G. Dávila, “Prediction of size effects in notched laminates using continuum damage mechanics”, *Composites Science and Technology*, vol. 67, no. 13, pp. 2715–2727, 2007.

[111] J. L. Chaboche, O. Lesné and T. Pottier, “Continuum damage mechanics of composites: Towards a unified approach” in *Studies in Applied Mechanics*, vol. 46, *Damage mechanics in engineering materials*, G. Z. Voyiadjis, J. W. Ju, and J.-L. Chaboche, Eds. 1st ed, Amsterdam, New York: Elsevier, 1998, pp. 3–26.

[112] L. Daudeville and P. Ladevèze, “A damage mechanics tool for laminate delamination”, *Composite Structures*, vol. 25, no. 1-4, pp. 547–555, 1993.

[113] P. Ladevèze, O. Allix, J.-F. Deü and D. Lévêque, “A mesomodel for localisation and damage computation in laminates”, *Computer Methods in Applied Mechanics and Engineering*, vol. 183, no. 1-2, pp. 105–122, 2000.

[114] P. F. Liu and J. Y. Zheng, “Progressive failure analysis of carbon fiber/epoxy composite laminates using continuum damage mechanics”, *Materials Science and Engineering: A*, vol. 485, no. 1-2, pp. 711–717, 2008.

[115] M. A. McCarthy, J. R. Xiao, N. Petrinic, A. Kamoulakos and V. Melito, “Modelling bird impacts on an aircraft wing – Part 1: Material modelling of the fibre metal laminate leading edge material with continuum damage mechanics”, *International Journal of Crashworthiness*, vol. 10, no. 1, pp. 41–49, 2005.

[116] R. J. Nuismer and S. C. Tan, “Constitutive Relations of a Cracked Composite Lamina”, *Journal of Composite Materials*, vol. 22, no. 4, pp. 306–321, 1988.

[117] K. Song, Y. Li and C. Rose, “Continuum Damage Mechanics Models for the Analysis of Progressive Failure in Open-Hole Tension Laminates” in *52nd AIAA/ASME/ASCE/AHS/ASC Structures, Structural Dynamics and Materials Conference*

[118] R. Talreja, “A Continuum Mechanics Characterization of Damage in Composite Materials”, *Proceedings of the Royal Society A: Mathematical, Physical and Engineering Sciences*, vol. 399, no. 1817, pp. 195–216, 1985.

[119] R. Talreja, “Damage development in composites: Mechanisms and modelling”, *The Journal of Strain Analysis for Engineering Design*, vol. 24, no. 4, pp. 215–222, 1989.

[120] F. P. van der Meer and L. J. Sluys, “Continuum Models for the Analysis of Progressive Failure in Composite Laminates”, *Journal of Composite Materials*, vol. 43, no. 20, pp. 2131–2156, 2009.

[121] Q. Yang and B. Cox, “Cohesive models for damage evolution in laminated composites”, *International Journal of Fracture*, vol. 133, no. 2, pp. 107–137.

[122] A. Turon, P. P. Camanho, J. Costa and J. Renart, “Accurate simulation of delamination growth under mixed-mode loading using cohesive elements:

Definition of interlaminar strengths and elastic stiffness", *Composite Structures*, vol. 92, no. 8, pp. 1857–1864, 2010.

[123] A. Turon, P. P. Camanho, J. Costa and C. G. Dávila, "A damage model for the simulation of delamination in advanced composites under variable-mode loading", *Mechanics of Materials*, vol. 38, no. 11, pp. 1072–1089, 2006.

[124] C. Fan, P.-Y. B. Jar and J. R. Cheng, "Cohesive zone with continuum damage properties for simulation of delamination development in fibre composites and failure of adhesive joints", *Engineering Fracture Mechanics*, vol. 75, no. 13, pp. 3866–3880, 2008.

[125] P. P. Camanho, C. G. Dávila and M. F. de Moura, "Numerical Simulation of Mixed-Mode Progressive Delamination in Composite Materials", *Journal of Composite Materials*, vol. 37, no. 16, pp. 1415–1438, 2003.

[126] C. Balzani and W. Wagner, "An interface element for the simulation of delamination in unidirectional fiber-reinforced composite laminates", *Engineering Fracture Mechanics*, vol. 75, no. 9, pp. 2597–2615, 2008.

[127] F. Aymerich, F. Dore and P. Priolo, "Simulation of multiple delaminations in impacted cross-ply laminates using a finite element model based on cohesive interface elements", *Composites Science and Technology*, vol. 69, no. 11-12, pp. 1699–1709, 2009.

[128] F. Aymerich, F. Dore and P. Priolo, "Prediction of impact-induced delamination in cross-ply composite laminates using cohesive interface elements", *Composites Science and Technology*, vol. 68, no. 12, pp. 2383–2390, 2008.

[129] R. Borg, L. Nilsson and K. Simonsson, "Modeling of delamination using a discretized cohesive zone and damage formulation", *Composites Science and Technology*, vol. 62, no. 10-11, pp. 1299–1314, 2002.

[130] B. Y. Chen, T. E. Tay, P. M. Baiz and S. T. Pinho, "Numerical analysis of size effects on open-hole tensile composite laminates", *Composites Part A*, vol. 47, pp. 52–62, 2013.

[131] S. R. Hallett, B. G. Green, W. G. Jiang and M. R. Wisnom, "An experimental and numerical investigation into the damage mechanisms in notched composites", *Composites Part A: Applied Science and Manufacturing*, vol. 40, no. 5, pp. 613–624, 2009.

[132] U. Mandel, R. Taubert and R. Hinterhölzl, "Laminate damage model for composite structures", *Composite Structures*, vol. 136, pp. 441–449, 2016.

[133] J. W. Ju, "Isotropic and Anisotropic Damage Variables in Continuum Damage Mechanics", *Journal of Engineering Mechanics*, no. 116, pp. 2764–2770, 1990.

[134] J. Lemaitre, “How to use damage mechanics”, *Nuclear Engineering and Design*, vol. 80, no. 2, pp. 233–245, 1984.

[135] Test Method for Mode I Interlaminar Fracture Toughness of Unidirectional Fiber-Reinforced Polymer Matrix Composites, ASTM D5528.

[136] V. Tamuzs, S. Tarasovs and U. Vilks, “Progressive delamination and fiber bridging modeling in double cantilever beam composite specimens”, *Engineering Fracture Mechanics*, vol. 68, no. 5, pp. 513–525, 2001.

[137] Test Method for Determination of the Mode II Interlaminar Fracture Toughness of Unidirectional Fiber-Reinforced Polymer Matrix Composites, ASTM D7905_D7905M-14, 2014.

[138] C. Schuecker and B. D. Davidson, “Evaluation of the accuracy of the four-point bend end-notched flexure test for mode II delamination toughness determination”, *Composites Science and Technology*, vol. 60, no. 11, pp. 2137–2146, 2000.

[139] M. J. Laffan, S. T. Pinho, P. Robinson and L. Iannucci, “Measurement of the in situ ply fracture toughness associated with mode I fibre tensile failure in FRP. Part I: Data reduction”, *Composites Science and Technology*, vol. 70, no. 4, pp. 606–613, 2010.

[140] S. T. Pinho, P. Robinson and L. Iannucci, “Fracture toughness of the tensile and compressive fibre failure modes in laminated composites”, *Composites Science and Technology*, vol. 66, no. 13, pp. 2069–2079, 2006.

[141] M. J. Laffan, S. T. Pinho, P. Robinson, L. Iannucci and A. J. McMillan, “Measurement of the fracture toughness associated with the longitudinal fibre compressive failure mode of laminated composites”, *Composites Part A: Applied Science and Manufacturing*, vol. 43, no. 11, pp. 1930–1938, 2012.

[142] M. J. Laffan, S. T. Pinho, P. Robinson and L. Iannucci, “Measurement of the in situ ply fracture toughness associated with mode I fibre tensile failure in FRP. Part II: Size and lay-up effects”, *Composites Science and Technology*, vol. 70, no. 4, pp. 614–621, 2010.

[143] L. Marín, E. V. González, P. Maimí, D. Trias and P. P. Camanho, “Hygrothermal effects on the translaminar fracture toughness of cross-ply carbon/epoxy laminates: Failure mechanisms”, *Composites Science and Technology*, vol. 122, pp. 130–139, 2016.

[144] J.-K. Kim and Y.-w. Mai, “High strength, high fracture toughness fibre composites with interface control—A review”, *Composites Science and Technology*, vol. 41, no. 4, pp. 333–378, 1991.

[145] P. P. Camanho and G. Catalanotti, “On the relation between the mode I fracture toughness of a composite laminate and that of a 0° ply: Analytical

model and experimental validation", *Engineering Fracture Mechanics*, vol. 78, no. 13, pp. 2535–2546, 2011.

[146] Test Method for Open-Hole Tensile Strength of Polymer Matrix Composite Laminates, ASTM D5766_D5766M-11, 2011.

[147] C. T. Herakovich, "Influence of Layer Thickness on the Strength of Angle-Ply Laminates", *Journal of Composite Materials*, vol. 16, no. 3, pp. 216–227, 1982.